Development of type II superlattice infrared detectors monolithically integrated on silicon substrates

Claudia Soledad González Burguete

Thesis presented in fulfilment of the requirements for the degree of
Masters in Philosophy (MPhil)

Department of Electronic and Electrical Engineering
University College London

August 2020

To Shubho, for his unconditional support always,

to my parents for always being with me,

to my parents-in-law for extending their love to me,

to my friends and family for always being at my side,

to all of them, thanks for helping achieved another dream.

Acknowledgement

Firstly, I would like to thank Professor Huiyun Liu for giving me the opportunity to achieve my dream of pursuing this research degree, and for his patience specially during my first months at UCL. I would also like to thank Dr Chin-Pang Liu for guiding me in my venture towards the world of IR photodetectors and for all his patience and knowledge in achieving this goal. I would also like to thank Dr Mingchu Tang, Dr Dongyoung Kim, Dr Arthur Onno, Dr Pamela Jurczak and Dr Mengya Liao for their patience while introducing me to the procedures and equipment during those first confusing months of my degree, and for always having a helpful hand and advise when I needed. I would also like to thank my colleagues Daqian Guo, Steven Chan, Fan Cui, Mahdi Alqahtani and Pouyan Martin for being my allies during my research project since the beginning. I would also like to thank my MBE team for their support and company during my time at UCL and for always having someone to share the day, thanks for all.

Secondly, I would like to thank DSTL (Defence Science and Technology Laboratory) and EPSRC (Engineering and Physical Sciences Research Council) for funding this research project and for support from their teams. I would also like to thank Dr Kenneth McEwan for overseeing this project on behalf of DSTL and for his valuable input.

Finally, I would like to thank the staff of LCN (London Centre for Nanotechnology) specially to Ms Vijayalakshmi Krishnan and Mrs Lorella Rossi for their valuable help during the fabrication process of this project and while using the LCN installations.

Abstract

The project's objective is the development of an InAs/GaSb type II superlattice (T2SL) medium wavelength infrared photodiode directly grown on Si substrate for the use of an infrared single pixel photodiode. The T2SL has been selected as the replacement for the state-of-the-art CdHgTe (CMT). The use of Si substrate will help with the integration into the Si-based technology by reducing the fabrication process and costs.

The T2SL is a photon detector with overlapping multiple quantum well structure and a type 2 bandgap alignment. The T2SL are fabricated using a combination of materials from the group III-V in order to achieve a well-controlled ultra-thin heterostructures using molecular beam epitaxy as a growth technique. The structure within the active region is designed to enhance the performance of the T2SL architecture by manipulating the thickness and doping of each layer.

The direct growth of a T2SL structure on the Si substrate has achieved similar structural and optical properties when compared to that grown on the GaAs substrate. The Si architecture has an absorption edge of 5.365µm when measured at 70K: dark current density at -1V is 4×10^1 A/cm^2; responsivity (R) peak is 1.2A/W; quantum efficiency (QE) at -0.1V is 32.5%; and specific detectivity (D*) peak is 1×10^9 cmHz$^{1/2}$/W.

The pπBn has best architecture over GaAs substrate due to the wide bandgap unipolar barrier. The pπBn has an absorption edge of 6.5 µm when measured at 77K: dark current density under -0.6V is 5×10^{-3} A/cm^2; R peak is 0.6A/W; QE at 0V and 3.25µm is 23%; and D* peak is 1×10^{11} cmHz$^{1/2}$/W.

These results demonstrate that the D* of the pπBn structure is just one order of magnitude smaller than the state-of-the-art CMT detector which is 2×10^{12} cmHz$^{1/2}$W.

Impact Statement

The aim of this project was to develop a high performance mid-infrared T2SL photodetector monolithically grown on Si substrate as a low-cost alternative to the CMT detectors.

The non-academic benefits are developed in collaboration with DSTL for potential military applications. This collaboration brings the expertise of T2SL photodetectors grown over Si subtrate which will lead to a wider deployment of IR techniques in the defence sector. These improvements will increase the performance of the infrared (IR) imaging systems for surveillance and reconnaisance missions giving DSTL significant technological advantages.

The academic benefits associated with this research are various. Firstly, the development of new growth techniques capable of direct growth over Si substrate and GaAs substrate while finding the best T2SL structure. The architecture was optimised further in order to create an IR detector capable of monolithically integrated on Si-based technology. These new growth techniques are capable of constantly developing the active region strucutres achieving results closely to the state-of-the-art CMT detectors.

Secondly, the association with DSTL can create further studentship projects with the opportunity to enhance this research in this field. This research could offer additional military applications for low-cost solution at near room temperature with acceptable performance.

And finally, the results can have further benefits in other fields of study including the hetero-integration of CMT on Si substrate, and in other photonic technologies that allow integration with the mainstream integrated circuit (IC) technology.

The significant impact of this project is attributed to being the first systematic investigation of the 6.1Å family of group III-V on IR technology associated with direct integration of readout integrated circuits (ROIC) based on the maturity of the Si-based

IC technology. The Si-based fabrication technology and large substrate size can reduce further the costs associated per unit fabrication and enhance the performance by creating larger formats.

The dissemination of this research was achieved during this research period with the publication of two articles as the first author, one research photography as competition winner, and five academic posters as the first author displayed only at UCL.

In the future, the dissemination of these results will continue as a reference in other publications, as my paper has been cited 12 times in papers published by other researchers. As means of public engagement with DSTL by designing a poster and a presentation depicting all the results obtained during this research project.

Table of Content

List of Figures and Graphs

List of Tables

List of Publications

Journal Publications

1. ***Claudia González Burguete,*** Daqian Guo, Pamela Jurczak, Fan Cui, Mingchu Tang, Wei Chen, Zhuo Deng, Yaojiang Chen, Marina Gutiérrez, Baile Chen, Huiyun Liu, Jiang Wu; *"Direct growth of InAs/GaSb type II superlattice photodiodes on silicon substrates"*; IET Optoelectronics, vol. 12, no. 1, pp. 2-4, February 2018.

2. Zhuo Deng, Daqian Guo, ***Claudia González Burguete***, Zongheng Xie, Jian Huang, Huiyun Liu, Jiang Wu, Baile Chen; *"Demonstration of Si based InAs/GaSb type-II superlattice pπn photodetector";* Infrared Physics and Technology, vol. 101, pp. 133-137, September 2019.

Picture Publication

1. ***Claudia González Burguete***, *"Molecular Beam Epitaxy Machine";* EPSRC Photographic Competition (3rd place), Press Release (2018). (https://www.telegraph.co.uk/news/2018/02/12/engineering-physical-sciences-photography-competition-2018/molecular-beam-epitaxy-machine-whichcreates-custom-wafers/).

Chapter 1: Introduction

1.1. Introduction to T2SL detector integrated on Si substrate

This project depicts the development of an InAs/GaSb type 2 superlattice (T2SL) monolithically integrated on Silicon (Si) substrate. Within the last decade, the T2SL have emerged as an alternative solution to replace the state-of-the-art CdHgTe (CMT) photodetector by improving the quality of the material, device structure design and device fabrication.

The T2SL infrared (IR) detectors are part of the third generation of photodetectors, defined by their staggered band alignment, and based on a pin structure [17]. The InAs/GaSb superlattice (SL) combination is the most commonly used for developing IR detectors as it is able to cover the entire IR spectrum from 1 to 30μm.

The T2SL is highly dependent on the structural composition profile, interfacial roughness and interfacial bonding across the layers. Therefore, the T2SL architecture is grown by molecular beam epitaxy (MBE) using ultra-thin heterostructures, where the layer thicknesses and doping are customised.

The monolithic integration of T2SL photodetectors on Si substrate faces some technical challenges such as maximizing the quantum efficiency and solving the growth issues of III-V materials over Si substrate. The use of Si substrate will help with the integration into the Si-based technology and by reducing the fabrication process and costs.

The Si-based technology is the ideal candidate for fabrication of large format focal plane arrays because the Si wafers are cheap, large, and mechanically and thermally robust for harsh environments. The mature Si-based technology takes advantages of direct integration of electrical and optical components, as well as the IR detector technology developed in order to create a compact and smart IR system.

1.2. Infrared Detectors

1.2.1. Introduction to Infrared Detectors

The electromagnetic spectrum is the range of frequencies of electromagnetic radiation with their corresponding wavelengths and photon energies. The electromagnetic radiation spectrum is divided into: gamma rays (nm, nanometres), x-rays (nm), ultraviolet (UV, nm), visible light (nm), infrared (IR, nm), microwave (mm-cm), and radio and TV (cm-km); which is depicted in Figure 1.1 [6].
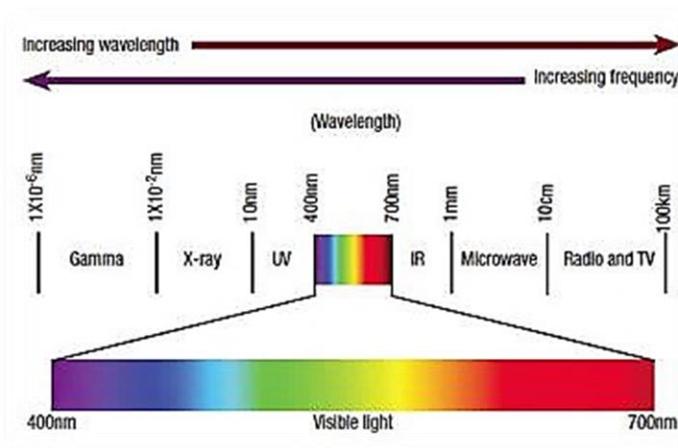
Figure 1.1: Electromagnetic Spectrum

The IR radiation has a range of wavelength between 750nm and 1mm and is divided into seven sub-divisions [20]:

a) near-infrared (NIR) between 0.78 to 1µm,

b) short wavelength IR (SWIR) between 1 and 3µm,

c) medium wavelength IR (MWIR) between 3 and 6µm,

d) long wavelength IR (LWIR) between 6 and 15µm,

e) very long wavelength IR (VLWIR) between 15 and 30µm,

f) far-infrared (FIR) between 30 and 100µm, and

g) submillimetre (SubMM) between 100 and 1,000µm (1mm).

However, the ISO 20473:2007 (which was confirmed in 2015) is the standard that specifies the division of optical radiation into spectral bands for optics and photonics into three divisions which are [49]:

a) near-infrared (NIR) between 0.78 to 3µm,

b) mid-infrared (MIR) between 3 and 50µm, and

c) far-infrared (FIR) between 50 and 1,000μm (1mm).

The first application for IR radiation since discovery was in astronomy, as its early application was associated with detection of IR radiation. The later applications were associated with forming IR images from temperature and emissive differences. Currently, most of the applications have been developed for military applications with some other applications including medical industry, earth resources, and energy conservation.

The progress of the IR detectors is directly related to the development of the semiconductor IR detectors, which are used to detect and absorb photons. A photocurrent from an IR detector is generated when photons with energy greater than the bandgap energy (E_g) of the absorbing material are absorbed, exciting electrons from the valence band to the conduction band and thus forming electron-hole pairs. The electron-hole pairs are then separated with an electric field with the electrons and holes now drifting in opposite directions. Since they are charge carriers, their movements constitute a photogenerated current or, simply, photocurrent. The fundamental optical excitation processes within the semiconductor is depicted in Figure1.2 [36].
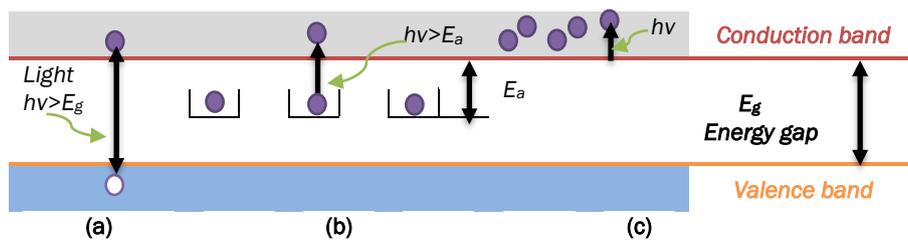
Figure 1.2: Fundamental optical excitation process a) intrinsic, b) extrinsic, and c) free carrier absorption

The pin photodiode has an intrinsic (i-region) semiconductor layer sandwiched between an n-doped and p-doped semiconductor layer, which is the most common structure as the depletion layer can be tailored in order to meet the requirements of photoresponse (electrical and optical characterisation) and bandwidth. The pin photodiodes are used in optical communications due to its ultra-fast photodetection which is better in comparison to the pn junction.

The pin photodiode design requires a balance between the response speed and quantum efficiency. This is because a thick intrinsic layer increases the photon absorption length and thus increases the quantum efficiency. However, a thick intrinsic layer also increases the times electrons and holes need to take to drift to the respective n-doped and p-doped layers. Such long transit times lead to a reduction in the bandwidth or speed of the pin photodiode.

1.2.2. History of Infrared Detectors

The history of the infrared (IR) detectors started in 1800 when a German-born British astronomer Frederick William Herschel [33] discovered the IR light while studying the spectrum of sunlight with a prism. In order to demonstrate this, he built a rudimentary monochromator using a thermometer as a detector for measuring the temperature of each colour of the spectrum. While doing this experiment, he discovered that beyond the colour 'red' the temperature was highest and with further studies he found that those rays behave like visible light and obey the same laws of reflection and refraction.

Around 1821, an Estonia-born German physicist Thomas Johann Seebeck [34] discovered the thermoelectric effect, while examining the junction behaviour of electrically conductive materials.

Around 1829, an Italian physicist Leopoldo Nobili [34] built the first thermopile in order to improve on the electrical thermometer by demonstrating the thermoelectric effect. The thermopile consisted in various thermocouples connected in series, in order to convert thermal energy into electrical energy.

Around 1833, two Italian physicist Leopoldo Nobili and Macedonio Melloni [34] modified a thermopile by using bismuth (Bi) and antimony (Sb). This thermopile consisted of a 10 in-line SbBi thermal pairs, which generated a high measurable output making this the best thermometer as it was able to detect the heat emitted from a person at a distance of 30ft. Due to its effectiveness, it became the most popular detector for IR radiation for the next 50 years.

Around 1873, an English electrical engineer Willoughby Smith [36] discovered the photoconductivity effect while experimenting with selenium (Se) as an insulator for submarines cables.

Around 1880s, an American physicist Samuel Pierpont Langley [35] developed a bolometer which was smaller, more sensitive and faster than any other measuring devices then known. The bolometer measures the power of incident electromagnetic radiation via the heating of temperature-dependent material electrical resistance. This bolometer used two platinum-foil ribbons connected as two arms of a Wheatstone bridge in order to measure the intensity of the solar radiation at various wavelengths. The developments of the bolometer allowed detecting changes of the temperature of less than 1/100,000°C.

During the early 1900s, the study of IR radiation had slowed as there was a lack of detectors sensitive and accurate enough to measure them. However, the study of light continued to develop and the interest in IR applications increased as a way of solving other problems.

Around 1915, an American physicist William Coblentz [6] developed a thermopile detector capable of seeing the IR radiation of 110 stars, making astronomy the first application of IR detectors. This invention contributed greatly towards the studies of radiometry and spectroscopy.

Around 1917, an American physicist Theodore Willard Case [17] developed the first IR photoconductor by discovering the photoconductivity properties of thallium sulphur (Tl_2S). This photoconductor was part of a military signalling system prototype used for under fog-like atmosphere conditions with limited results.

During the early 1930s, there were many developments in the fields of photon detectors, image converters and IR spectroscopy. Around 1933, a German-born American physicist Edgar Walter Kutzscher [36] discovered the photoconductivity of lead sulphide (PbS) with a response time of 3μm, which was kept secret due to World War II until 1945.

During World War II, many advances occurred in the development of high-performance IR technology leading to the birth of modern IR detectors. The photon technology was combined with the science of the semiconductor material and the developments in integrated circuits.

During 1944, an American physicist Robert Joseph Cashman [36] decided to focus his research in PbS detectors after improving the Tl_2S detector, which was produced at Northwestern University in United State of America. He discovered that other semiconductors belonging to the lead salt family could be used as IR detectors by using them as polycrystalline films of 1μm thickness. The IR applications were focused on communication, fire control and search systems.

During 1950s, the first generation of extrinsic photoconductive detectors were developed after the discovery of the transistor [18] by encouraging developments in growth and material techniques. Germanium (Ge) was the first element which benefited from the technique of control impurities, allowing this to be the basis for the first extrinsic detectors. The Ge detectors were combined with copper (Cu), mercury (Hg), zinc (Zn) and gold (Au) allowing the device to increase their wavelength range to cover LWIR and VLWIR. Additionally, the advances obtained on narrow bandgap semiconductor were made by increasing the wavelength and sensitivity of the detectors, the first material in this category was indium antimony (InSb) from the newly discovered III-V semiconductor group.

During 1960s, a number of narrow gap semiconductors alloys were introduced from different semiconductor groups: III-V (InAsSb, indium arsenic antimony), IV-VI (PbSnTe, lead tin tellurium) and II-VI (CdHgTe, cadmium mercury tellurium, CMT) [20] which could be tailored according to their spectral response. The CMT device covers up to the VLWIR (30μm) range making this semiconductor alloy the best option for wide range IR detectors.

During 1970s, the development of the group IV-VI alloy photodetectors was discontinued due to their high dielectric constant [5] and the first generation of linear arrays was developed using intrinsic photoconductive of PbS, PbSe and CdHgTe detectors. The studies of CdHgTe continued developing for high-speed applications

due to its low dielectric constant and variable bandgap providing a broad range for IR detector designs from SWIR to VLWIR.

During 1980s, the development of the second generation of IR detectors [18] was focused on the large photovoltaic CdHgTe array in the thermal imaging ranging from MWIR to LWIR. This generation was marked with LWIR first forward-looking IR (FLIR) systems operating with a single-stage cryoengine allowing the system to be compact, lighter and using less power. The research of this generation was focused on passive IR photodiodes for imaging applications due to the limitations of photoconductive detectors, as these are difficult to multiplex into focal plan arrays (FPA).

During 1990s, the development of the third generation of IR detectors [18] was focused on providing a larger number of pixels, larger frame rates, better thermal resolution, multicolour functionality, as well as on-chip functions. The multicolour FPA CdHgTe architecture consists of a LWIR photodiode behind a SWIR photodiode, where each layer absorbs radiation up to their cut-off wavelength allowing the collection in the following layers. The studies were focused on Type II superlattice (T2SL) and quantum dots IR detectors (QDIR).

The timeline of the materials investigated within in the infrared field is depicted in Table 1.1 [18].

Table 1.1: History of the development of IR detectors

Year	Materials
1940	Tl_2S
1955	Ge: Cu/Hg/Zn/Au InSb [III-V]
1960	CdHgTe [II-IV] InAsSb [III-V]
1980	CdHgTe/CCD CdHgTe SPRITE
1988	InGaAs
1985	QWIP
1995	QDIP **T2SL**
2000	MEMS FPAs Four-colour FPAs
2005	Graphene nBn detectors 2D materials
2010	Trapping detectors

1.2.3. Classification of Infrared Detectors

The IR detectors can be classified into two types: thermal and photon, which are depicted in Table 1.2 [20].

The thermal detectors work when the radiation is absorbed by resulting in changes in the material temperature and some other physical properties to generate an electrical output which are generally wavelength independent [17]. Measurements are taken for the pyroelectric detectors (which are sensitive optoelectronic component used for detecting electromagnetic radiation in a wavelength range) from the spontaneous internal polarisation, and for the bolometers from the change in electrical resistance.

The photon detectors (quantum detector) work when the radiation is absorbed within the material by the interaction between electrons and holes from the lattice [17]. These detectors depend on a specific wavelength and exhibit a good signal-to-noise performance to prevent thermal generation of charge carriers.

Table 1.2: Comparison of IR Detectors

Detector	Type	Material	Advantages	Disadvantages
Thermal	Thermopile, bolometers, pyroelectric		• Light, rugged, reliable and low cost • Room temperature operation	• Low detectivity at high frequency • Slow response (ms order)
Photon	Quantum Wells	Type 2 *(InAs/InGaSb, InAs/InAsSb, InAs/GaSb)*	• Low auger recombination rate. • Easy wavelength control. • Multicolour detectors.	• Complicated design and growth. • Sensitive to interfaces.

1.2.4. Types of Infrared Architecture

The photovoltaic effect is the most common photoeffect obtained when the electrons interact with the IR radiation. Each device is designed to exploit a particular IR detection application.

The **pn photodiode** is the basic device. The photons with energy higher than the bandgap energy create electron-hole pairs in the material. Then, the electron-hole pairs are separated by the strong electric field in the depletion region where they are accelerated towards the respective n- and p-doped regions to become majority carriers [39].

The photogenerated electrons drift towards the n-type region and the holes towards the p-type region. The direction of the photocurrent is from the n-type region (cathode) to the p-type region (anode) [38].

In a pn photodiode, the photocurrent is a result of the drift current if the electron-hole pairs are generated and separated in the depletion region. When a pn photodiode, not acting as a photodiode, is forward biased, then the current that is formed is called the diffusion current.

The dark current is the superposition of current contributions from three diode regions: bulk, depletion region and surface; which can be distinguished from thermal current, surface leakage current and space-charge-limited current [20]. The most common solution for analysing the current-voltage (I-V) curve is to numerically add all the current components to the experimental data over a range of both applied voltage and temperature.

The photodiodes are constructed so that the absorption of radiation occurs in the p-type region, ensuring that most of the photocurrent is carried by electrons which are more mobile than holes (whether by diffusion or drift) [20]. The conductivity within the doped regions is high and this does not allow any electric field to move either holes or electrons. The electrons move by diffusion then the direction of movements depends on the electron concentration gradient which also depends on the incident direction of the photons.

If the depletion region is too narrow, the electron-hole pairs generated in the n and p regions would have to diffuse back to the depletion region before they could be collected. Devices with very thin depletion region tend to show distinct slow and fast response components, where the fast component is due to carriers generated in the depletion region, and the slow component arises from diffusion carriers [38].

The **pin photodiode** consists of an i-region (undoped) sandwiched between and p+ and n+ region (doped) [6]. The i-region (depletion region) width can be tailored to achieve the requirements of photoresponse (electrical and optical characterisation)

and bandwidth. The photodiode design requires the balance between the response speed and the quantum efficiency. Therefore, in order to obtain high quantum efficiency, the depletion region should be thicker. The pin photodiode structure is depicted in Figure 1.3 [20].
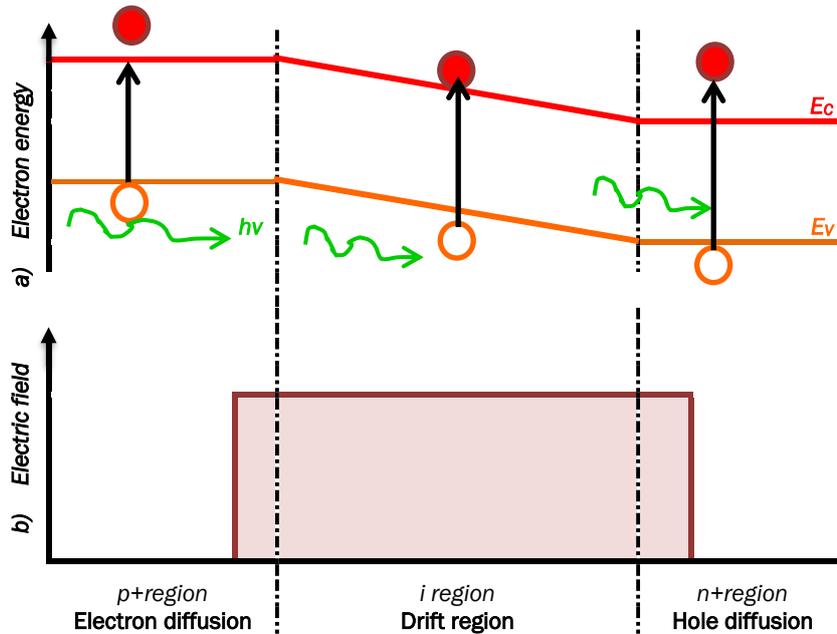
Figure 1.3: pin photodiode a) energy band diagram and b) electric field profile

The front-illuminated pin photodiode has an etched opening in the top contact and the active area is reduced to the size of the incident light beam. The sidewalls of the mesa are covered using a passivation material (like polyimide) in order to reduce the surface leakage of the mesa. In addition, the main source of noise is the generation-recombination noise, while the dark current in a reverse-biased junction is very low.

The response speed of a pin photodiode is limited either by the transit time or by circuit parameters [20]. The transit time of carriers across the i-region depends on its width and the carrier velocity, and even for moderate reverse biases that carriers drift across the i-region with saturation velocity. The transit time can be reduced by reducing the i-region thickness.

The **nonequilibrium photodiodes** consist of a near-intrinsic (narrow gap) sandwiched between two wider gap layers (or one wider gap layer and one very heavily doped layer) [37]. These devices can be written as PπN, PπN+ and PvN+; where the

uppercase is the wider gap, + (plus) is the high doping in excess of 10^7 cm^{-3}, π is the near intrinsic p-doped, and ν is the near intrinsic n-doped. This device provides good detectivity resulting in reduced leakage.

The **nBn detector** consists of an n-type narrow bandgap (thin contact layer), a wide-bandgap layer with a barrier for electrons (no barrier for holes), and a thick n-type narrow bandgap (absorbing layer) [20]. The minority carrier photoconductor consists of a high barrier layer between two contacts where the majority carrier current is blocked by the large energy offset while allowing the photogenerated minority carrier. This device is very versatile and works with materials like InAs, InAsSb and InAs/GaSb. The band diagram of the nBn structure is depicted in Figure 1.4 [20].
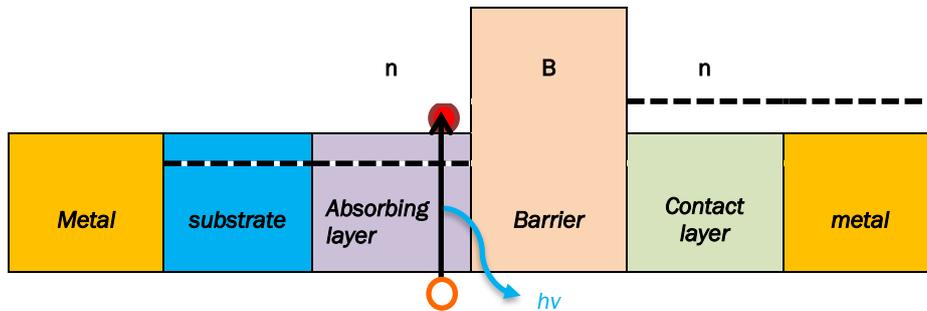
Figure 1.4. Flatband diagram of an nBn structure

1.2.5. Types of Infrared Detectors

The infrared photodetector (IRPD) is the technology with many applications for this modern world, where each is designed to exploit a particular IR application.

The **bulk detector,** like HgCdTe (CMT) and InSb photodetectors, is the most common IRPD technology because of the maturity of its technology and this was the first developed. The active portion of these detectors is a photodiode, which can be constructed in various structures and techniques [58]. The bulk detectors have the highest detectivity.

The **quantum well infrared photodetector** (QWIP) is the simple construction of this type. The QWIP consists of periodic repetition of layers of two material with different

bandgaps, where the material with lower bandgap is referred as the well layer and the one with the higher bandgap is referred as the barrier layer [20].

The **strained-layer superlattices photodetectors** (SLS) has a similar structure to QWIP but the physical principles are very different. The SLS active layers have a thickness of the same order of magnitude. The main difference between the QWIP and the SLS is the thickness of its layers, as the SLS has thinnest layers in order for the signal to overlap creating minibands [58]. The SLS has the closets merits to the bulk detector.

The **quantum dots infrared photodetectors** (QDIP) is based on a QWIP with an additional layer of dots. The dots have a narrower bandgap compare to the barrier material in order to create a local quantum well. The QDIP has improved merits like low dark current and high detectivity, as it is less sensitivity to defects compared with conventional bulk materials [56].

The **quantum dots-in-a-well photodetectors** (DWELL-IP) is the combination between the QWIP and the QDIP, where the weakness of both structures has been addressed. DWELL-IP begins with the growth of a wide-bandgap material referred as the barrier material, followed by the growth of a narrower bandgap material referred as the well material. [58].

The comparison between HgCdTe [59], QWIP [63], SLS [62], QDIP [61] and DWELL [60] all on GaAs substrate, which are depicted on Table 1.3.

Table 1.3: Comparison table between HgCdTe, QWIP, SLS, QDIP and DWELL at LWIR and 77K

Parameter	HgCdTe	QWIP	SLS	QDIP	DWELL
Detectivity [cmHz$^{1/2}$W^{-1}]	2×10^{13}	2×10^{11}	1×10^{12}	1×10^{11}	3×10^{10}
Responsivity [A/W]	1	1.4	3.2	5.3	3.58
Dark current density [A/cm^2]	2.5×10^{-4}	1×10^{-9}	1×10^{-3}	3×10^{-8}	5×10^{5}

1.2.6. Next generation of Detectors

The next generation of photodetectors are focused on regulating the flow of light at a range beyond the optical wavelength and ignoring the limits regarding the two-

dimensional (2D) and the three-dimensional (3D) nanosculptures in order to develop new detectors from unconventional materials and geometries [50].

The **3D nanostructures** have a range from the ultraviolet (UV) to the near-infrared (NIR) region, and they can be tailored as these materials possess optoelectronic tunability. The next generation are made of solution-processed semiconductors like organic metals, metal-halide perovskites (MHP) and quantum dots [51]. These new detectors can compete with the standard inorganic semiconductor like Si or Ge in terms of detectivity, and with InGaAs or HgCdTe in terms of high-temperature epitaxial semiconductor.

These generation of detectors faces new challenges associated with the new process required to grow these new architectures in order to develop new functions. The 3D nanostructures are colloidal quantum-dot (CQD) and MHP photodetectors.

1. The ***CQD photodetectors*** has a range from the visible to the IR region. The way to reach the IR is by adjusting the size of the nanocrystals during synthesis. The CQD bandgap engineering can help designed a graded energy and electric field in order to concentrate the photogenerated carries; yielding a megahertz - 3dB bandwidths at zero bias and high detectivity in the NIR [64].

2. The ***MHP photodetectors*** is the combination of the advantages offered from the use of organic and inorganic semiconductor resulting in a simple diode architecture, which can be photogenerated and collect without a loss [65].

The **2D nanostructures** has controlled over light matter interaction of nanoscales and has aided the discovery of new phenomena, which has developed new strategies for integrated circuits (IC) and high expectation for future discoveries. The 2D materials have developed photodetectors as they have a wide range from the visible to the terahertz passing through the IR region. These materials can produce a heterostructure by assembly monolayers [51].

The construction of 2D nanostructures required 2D materials. Some of these 2D materials which have been successfully isolated are: graphene, hexagonal boron

nitride (hBN), transition metal dichalcogenides (TMDC), black phosphorous (BP), covalent organic frameworks, nitrogen-rick holey conjugate polymer, and lead-free halide perovskite materials [66]. The 2D nanostructures are graphene-based photodetectors, TMDC-based photodetectors and BP-based device.

1. The ***graphene-based photodetectors*** have a zero band with an interband transitions, which allow the absorption of photons over a wide range from mid-infrared (MIR) to UV region. Graphene-based photodetectors have a low responsivity, which contributes to a small absorption coefficient. Graphene is a hexagonal monolayer sp2 bonded carbon structure visualized as a 2D version of a 3D crystalline graphite. Graphene has emerged as the best example of fabrication post-silicon nanostructures device [67].

2. The ***TMDC-based photodetectors*** behave like a semiconductor with a good bandgap suited for NIR region. The TMDC bulk construction has an indirect bandgap, while the monolayer construction has a direct bandgap and can be tuned using the electric field for optoelectronic applications. The TMDC comprises of a combination of metals and chalcogens (MX_2; M for metal, X for chalcogen) [51].

3. The ***BP-based photodetectors*** have a tuneability properties, which works over a wide range from the visible to the IR region making this detector extensively used in photonic devices. This detector has become a promising candidate for IR applications as an innovative new device. BP is a layered puckered orthorhombic structure with a narrow bandgap, which is characterized as multilayer flakes by recording their IR relative polarization-resolved extinction spectra [68].

1.3.   Monolithically Integration on Si substrate Detectors

1.3.1. Introduction to Monolithically integration

In the evolution of photodetectors, the next step is the silicon integrated circuit (IC) photodetectors in order to support single-chip photonics systems. Therefore, the expectation in developing new photodetectors is compatibility with IC and advance functionality.

Silicon is the most important material with the most applications due to its abundance, which helps with large-scale production at low cost. Silicon has good carrier mobility for electrons at $1350cm^2$ V^{-1} s^{-1} and for holes at $480cm^2$ V^{-1} s^{-1}. The maturity of the chip technology like complementary metal-oxide semiconductor (CMOS) has been achieved by controlled doping and epitaxial growth, which generates silicon integrated circuits (Si-IC) [69].
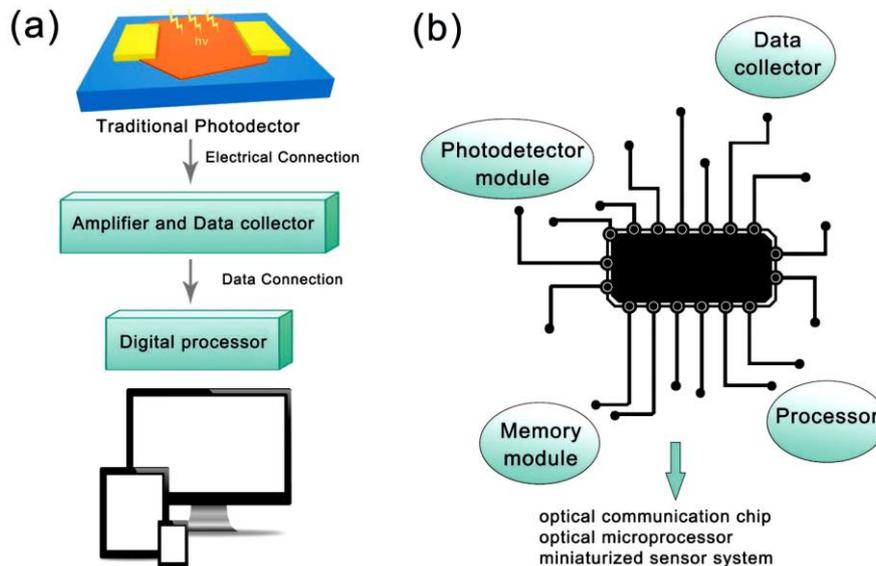
Figure 1.5 Schematic diagrams a) traditional photodetectors and b) monolithic

The construction of traditional photodetectors requires additional electronic components in order to become integrated with Si-IC and the challenges associated with miniaturizing the system to suit the smart equipment. Si-compatible photodetectors require the monolithically integration on Si of electronic and optical components in order to create single-chip photonics systems. Both systems are depicted in Figure 1.5 [52].

Currently, not all the photodetectors are compatible with the current chip fabrication. the dominant chip in the market is the CMOS, therefore, all Si-IC devices need to be constructed on bulk Si wafer in order to benefit from the Si chip in industry [69].

Although silicon is a very important material for developing chip, it is a terrible photosensitive material due to its indirect bandgap making it a poor photoconductive material. Its bandgap of 1.1eV decreases the absorption beyond 800nm with a cutoff at 1,100nm. The Si techniques developed for bulk Si materials are the foundation of today's integrated circuit, which is the key of the current electronic platforms [52].

The monolithically integration has taken two paths. The first one aims to be directly compatible with the current IC technology in order to achieve better properties. The proposal to fulfil this approach is an all-silicon photodetector, which is called Si-compatible photodetectors. The second aims to develop a methodology using epitaxial growth on Si substrate in order to realize applications using III-V semiconductors [54].

1.3.2. Silicon compatible Detectors

The silicon-compatible (Si) photodetectors are based on Si homojunctions with excellent lattice match in order to show excellent stability and highly uniform build-in electric field. The Si-based heterojunction structures have allowed the expansion of the spectral response from ultraviolet (UV) to long-wavelength infrared (LWIR) region using various materials with different bandgaps like: n-ZnO, TiO2, Se, InGaAs, CuO, SnTe, reduced graphene oxide, and graphene [70].

Traditional Si-based heterojunction structures have achieved advances in the field of enhanced optical detection at multiple wavelengths with omnidirectional photodetection. However, many suffer Auger combinations due to the lattice mismatch of the composite materials and needing attention into the interface structures in order to satisfy the requirements of ultrafast photodetectors [64].

The fast development of graphene has promoted the raise of 2D crystal applications, as they are chemical inert to Si for direct growth to obtain heterostructures with Si

substrates [52]. Some of these Si-compatible photoconductive devices are: metal-semiconductor-metal (MSM) device, photo-FET (field effect transistor) and hybrid photo-FET.

1. The **Si MSM device** is where the photosensitive material forms a channel between two electrodes, and the photoconductivity is detected by the current variation under bias [71].

2. The **photo-FET device** decreases the dark current of the MSM devices and at the same time inherit the photoconductive gain. The facile dielectric epitaxy of the Si makes it an excellent substrate for photo-FET [72].

3. The **hybrid photo-FET device** improves the photoelectric performance and spectral response of the photo-FET, as well as solving the problems between responsivity and sensitivity from the traditional structure. These devices can be fabricated on a Si/SiO_2 substrate. They are also able to maintain their enhanced responsivity from the photoconductive gain and obtain low leakage current from the fully depleted channel, while achieving remarkable high level of sensitivity and responsivity [72].

Some of the all-silicon photodetector devices are proposed based on different physical properties and are: mid-bandgap absorption-based (MBA) devices, surface-state absorption-based (SSA) devices, internal photoemission absorption-based (IPA) devices, and two-photon absorption-based (TPA) devices [53].

1. The **MBA-based devices** are used to develop integrated optical detectors completely compatible with the standard silicon technology and the sensitive optical band wavelengths.
2. The **SSA based** ring resonator photodetectors.
3. The **TPA based** photonic crystal nanocavity photodetectors.
4. The **IPA based** photodetectors associated to plasmonic waveguiding structures.

1.3.3. Silicon non-compatible Detectors

The silicon (Si) non-compatible detectors is another solution for monolithically integrated infrared (IR) photodetectors on a Si platform. Si is a good substrate for large-format focal plane array (FPA), the lattice mismatch between the Si and the III-V materials is ~4%, making this a good alternative for monolithically integrated FPA on Si substrates [56].

The growth of III-V semiconductors on the Si substrate have problems due to the large lattice constants, the thermal expansion coefficients between layers, and the growth of polar compounds on a non-polar substrate. Therefore, heteroepitaxial growth requires a clear understanding of the growth mechanism and a detailed control of the growth process, which is decided at the early growth stage [55].

The initial stage for developing the growth on GaSb substrate applications was the use of an AlSb buffer layers, which is called the nucleation layer. This nucleation layer was later used during the growth over Si substrate. The nucleation layer creates the interface between the Si substrate and the GaSb buffer layer, which allows flat and well-ordered atomic formations [73].

Currently, there have been examples of direct growth on Si substrate on quantum-dots infrared photodetectors (QDIP), and nanowire devices (NW).

The **nanowire device** (NW) presents small epitaxial interface allowing the growth of high-quality single crystalline material despite a high degree of lattice mismatch [57].

Table 1.4: Comparison table between QWIP and NW at LWIR

Parameter	QWIP [74]	NW [57]
Responsivity [A/W]	0.33	0.68
Dark current [A]	0.8nA @-1V	1.7nA @-2V
Dark current density [A/cm²]	8×10^{-5} @-1V	

1.4. Current Challenges

In the field of IR (infrared) photodetectors, CdHgTe (CMT, cadmium mercury telluride) is considered the state-of-the-art benchmark, as it is currently dominating the market.

This is because CMT IR photodetectors properties are closely matching the ideal optical properties associated with IR sensing by using well-established techniques.

While, the CMT has helped revolutionize the IR detectors due to its variable bandgap allowing the creation of wide range of applications, the reasons for researching an alternative structure is because mercury is highly toxic, when inhaled or ingested. The comparison of CMT (state-of-the-art) with two types of superlattice demonstrates the advances of the superlattice structures, which is depicted in Table 1.5 [41].

Table 1.5: Comparison table between CdHgTe (CMT) and T2SL photodiodes at 77K

Parameter	CdHgTe	InAs/GaSb SL	InAs/InAsSb SL
Background doping	$5 \times 10^{13} cm^{-3}$	$< 10^{15} cm^{-3}$	$> 10^{15} cm^{-3}$
Quantum efficiency	80%	~50-60%	~40%
Thermal GR carrier lifetime	≈10µs	~0.1 µs	~1 µs
R_0A product (λ_c=10µm)	1000 Ωcm^2	500 Ωcm^2	~100 Ωcm^2
Detectivity (λ_c=10µm, FOV=0)	$3 \times 10^{12} cmHz^{1/2}W^{-1}$	$1 \times 10^{12} cmHz^{1/2}W^{-1}$	$4 \times 10^{11} cmHz^{1/2}W^{-1}$

*FOV (field of view)

Currently, the challenges associated with using CMT detectors are: the very expensive cost, the difficulty obtaining uniformity during growth for long wavelengths, and the limitations in size associated with the use of the cadmium zinc telluride (CdZnTe) substrates.

Therefore, Type II superlattice (T2SL) IR detectors have been proposed as an alternative approach to CMT detectors. The most common substrates used in T2SL are GaSb and GaAs; however, these are expensive and have a limited size. Therefore, it is important to find a more sustainable substrate like silicon (Si), as this will benefit greatly from the Si-based integrated circuit (IC) technology that is quite mature and will help reduce the fabrication costs.

The greatest challenge is to develop a growth technique capable of creating multiple structures over Si substrate, therefore, the migration of the architectures grown on

GaAs substrates towards Si substrates is something that some research groups are aiming to achieve.

These research groups are working towards solving their own version of this problem. These growth techniques are been developed for metal-organic chemical vapor deposition (MOCVD) and molecular beam epitaxial (MBE).

The research groups depicted in Table 1.6 are currently working in these growth techniques.

Table 1.6: Research groups

Group	Country	Materials (substrate/growth)	Growth technique
Anadolu University	Turkey	GaSb (substrate) InAs/InAsSb	MBE [10]
Arizona State University	USA	GaSb (substrate) InAs/InAsSb	MBE [15]
Northwestern University	USA	GaSb (substrate) InAs/InAsSb	MOCVD [29]
Shanghai Tech University	China	GaSb (substrate) InAs/GaSb	MBE [44]
Lancaster University	UK	Si (substrate) InAs/InAsSb	MBE [30]

The organisation of the thesis is as follows:
a) Chapter 2 will describe a comprehensive analysis of the type 2 superlattice (T2SL) IR detectors,
b) Chapter 3 will provide detailed description of every piece of equipment, technique and process required to build and test every architecture is this project,
c) Chapter 4 will compare the performance of the basic nip structure grown on Si substrate and on GaAs substrate,
d) Chapter 5 will compare the performance of the nip, pπn and pπBn structures grown on GaAs substrates,
e) Chapter 6 will describe the conclusion of Chapter 4 and 5; and the future work.

Chapter 2:   Type 2 Superlattice Infrared Detectors

2.1. Introduction

This chapter depicts a comprehensive analysis of the type 2 superlattice infrared detectors (T2SL), as this project focuses on the development of an InAs/GaSb T2SL infrared (IR) detectors. The analysis includes the III-V group semiconductor as InAs/GaSb belong to this group, the quantum theory behind the T2SL structure, and the development of new architectures for the active region.

The semiconductor is a material with an electrical conductivity which becomes a weak insulator at low temperature. The InAs/GaSb belongs to the group III-V of semiconductor materials; as In and Ga belong to group III, and As and Sb belong to group V.

The superlattice (SL) structure is a type of multiple quantum well (MQW). The overlapping of wavefunction occurs when introducing more wells (or thinner wells) leading to the creation of a continuous band of states. The multiple QW wavefunction reaches zero between the well while the superlattice overlaps, making this the main difference between these two structures.

The T2SL energy band alignment is when the bandgap of material A is outside the bandgap of material B. Many new superlattice combinations have been created based on matching crystal structures and lattice constant.

The IR photodetectors are devices that detect photons by using a reverse biased semiconductor architecture such as the pin structure. The photodetectors can only detect materials with right size of energy gap (smaller than the photon energy). The new architectures are developed using the basic pin structure as a starting point with the developments taking place at the active region.

2.2. Semiconductors

2.2.1. Introduction to Semiconductors

The semiconductor is a material with an electrical conductivity between a conductor and an insulator. The semiconductor has a smaller bandgap compared to an insulator and at low temperatures the semiconductor becomes a weak insulator, as only few electrons have sufficient energy to jump from the valence band to the conduction band [14].

The energy diagram of the semiconductor has three regions: conduction band (E_c), bandgap (E_g) and valence band (E_v). This is depicted in Figure 2.1 [20].
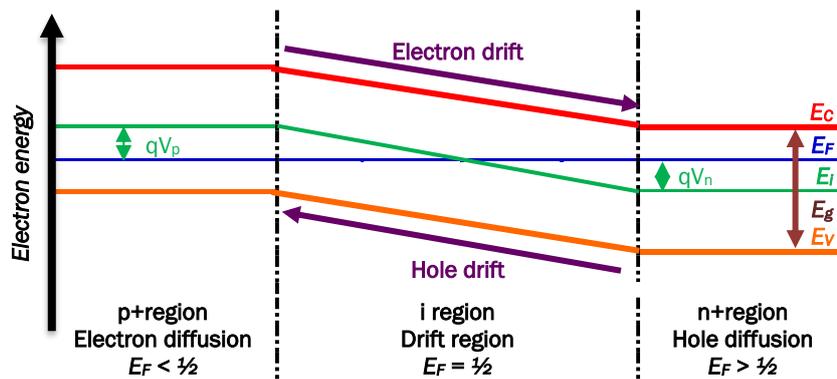
Figure 2.1: pin photodiode in thermal equilibrium

The semiconductors can be classified as intrinsic (undoped or pure) or extrinsic (doped) [25]. The intrinsic semiconductor is in its pure form, which means that has the same number of electrons and holes.

The extrinsic semiconductor is formed when impurities are introduced to the material by creating extra mobile holes or electrons, this process is called doping. When the material has excess number of electrons it is called n-type (negative charge or donor), or with an excess number of holes it is called p-type (positive charge or acceptor). This makes doping an essential element of designing electronic devices.

The energy diagram for a pin structure requires the alignment of each energy level using a fermi level (E_F), which is a reference line that helps depict the concentration of holes and electrons depending on the doping conditions.

In case of the intrinsic semiconductor (E_i), the fermi level is in the middle of the energy band. In case of the extrinsic semiconductor, the fermi level moves closer to the edge of the band depending on the doping concentration, for p-region closer to E_v and for n-region closer to E_c. The energy diagram for a pin structure in thermal equilibrium is depicted in Figure 2.1.

The fermi level is the energy level at which the probability of occupation by an electron is 50%, which is described by the fermi-dirac function as the probability of an energy level being occupied by an electron. The function is applied to obtain the density of electrons in the conduction band or the density of holes in the valence band. These equations are depicted in equation E2.1 [25].

$$n = n_i \exp\left(\frac{E_F - E_i}{kT}\right); p = n_i \exp\left(\frac{E_i - E_F}{kT}\right) \qquad \text{[E2.1]}$$

where *n* is the electron carrier concentration per unit volume, *p* is the hole carrier concentration per unit volume, n_i is the intrinsic carrier concentration, *k* is the Boltzmann's constant (1.38x10^{-23} J/K), and *T* is the temperature (K).

2.2.2. Introduction to III-V Semiconductors

The semiconductor materials are classified into five groups in the periodic table, this is depicted in Table 2.1 [7]. The combination of more than one semiconductor forms an alloy (binary, ternary, etc), which is the basis of bandgap engineering.

The most common binary alloys for use in semiconductor belong to the group III-V, as they have a stronger chemical bond due to their mixture of covalent and ionic bonding; and have a direct bandgap. The semiconductors of group II-VI are more of an ionic bonding and the group IV is a purely covalent bonding.

Table 2.1: Semiconductor Materials

II A	III A	IV A	V A	VI A
Be *Beryllium*	B *Boron*	C *Carbon*	N *Nitrogen*	O *Oxygen*
Mg *Magnesium*	Al *Aluminium*	Si *Silicon*	P *Phosphorus*	S *Sulphur*
Zn *Zinc*	Ga *Gallium*	Ge *Germanium*	As *Arsenic*	Se *Selenium*
Cd *Cadmium*	In *Indium*	Sn *Tin*	Sb *Antimony*	Te *Tellurium*
Hg *Mercury*	Tl *Thallium*	Pb *Lead*	Bi *Bismuth*	

The most common binary alloys of group III-V are: gallium arsenide (GaAs), aluminium arsenide (AlAs), indium arsenide (InAs), indium antimony (InSb), gallium antimonide (GaSb), gallium phosphide (GaP), gallium nitride (GaN), aluminium antimonide (AlSb), and indium phosphide (InP).
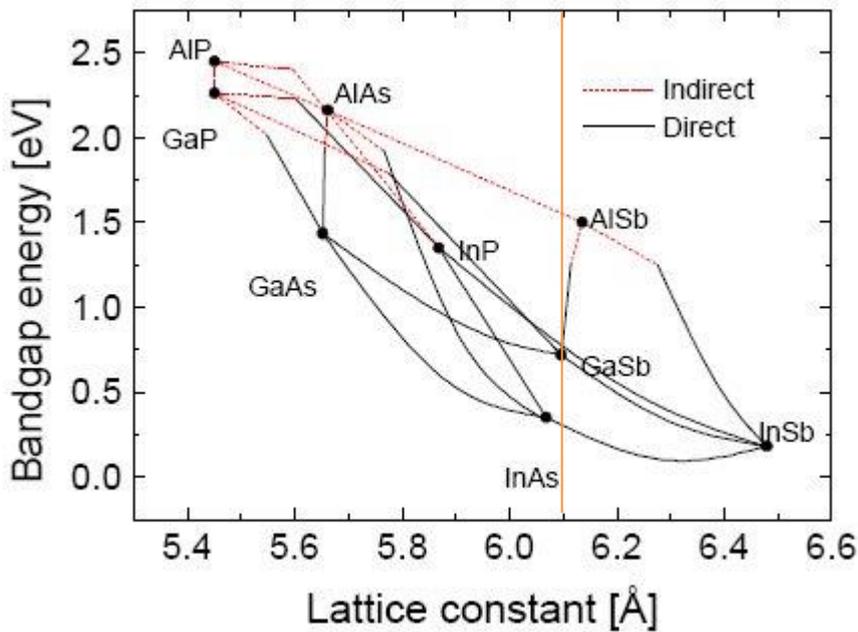
Figure 2.2: Bandgap energy vs lattice constant for some III-V semiconductors at room temperature values.

The semiconductors are characterised in terms of their crystal structure and lattice constant. The most common structures are diamond (like Si and Ge) and zincblende (like GaAs, AlSb, AlAs, InAs, and GaSb to mention few). The lattice constant is the physical dimension of the unit cell in a crystal. The lattice constants in different group III-V alloys are depicted in Figure 2.2 [32].

2.2.3. Introduction to Infrared Photodetectors

The infrared (IR) photodetectors, as described before, are devices that detect photons by using reverse biasing semiconductor in a pin architecture.

The electrons are excited to the conduction band by illuminating the semiconductor with electromagnetic radiation (photons). The photons will create electron-hole pairs if the photon energy (E) is equal or greater than the semiconductor bandgap (E_g), and these photons are absorbed by the material. The photons with energy lower than bandgap are not absorbed. The photon energy is determined by the wavelength of the light, which is depicted in equation E2.2 [8].

$$E = h v = \frac{hc}{\lambda} = \frac{1.241 \; x 10^{-6}}{\lambda} \qquad \text{[E2.2]}$$

where E is the photon energy (eV or J, depending on the Planck's constant units), h is the Planck's constant (4.136x10^{-15} eV s), v is the frequency of the light (1/s or Hz), c is the speed of light (3x10^8 m/s), and λ is the wavelength (m).

In order to find out the absorption edge wavelength (λ_c), which is the limit beyond which no more photons are absorbed, we used equation E2.2 using the values of the bandgap of the materials. The absorption coefficient determines the rate at which photons are absorbed and is depicted in equation E2.3 [20].

$$I = I_0 \exp(-\alpha x) \qquad \text{[E2.3]}$$

where I is the photon intensity as a function of the distance x, I_0 is the incident photon intensity (watts per unit area) at x=0, and α is the absorption coefficient (per unit distance).

The combination of the electron free space (relationship between energy and momentum) and quantum mechanical momentum results in electron-momentum (E-k) diagram, which links the energy of an electron to its momentum.

The E-k curve is a parabolic and all values of energy (and momentum) are allowed, with a minimum at k=0. The mass of a particle is inversely proportional to the curvature of the E-k curve.

The recombination of electrons with holes occurs at the energy gap involving a change in both energy and momentum, which can be either direct or indirect band gaps and is depicted in Figure 2.3 [31].
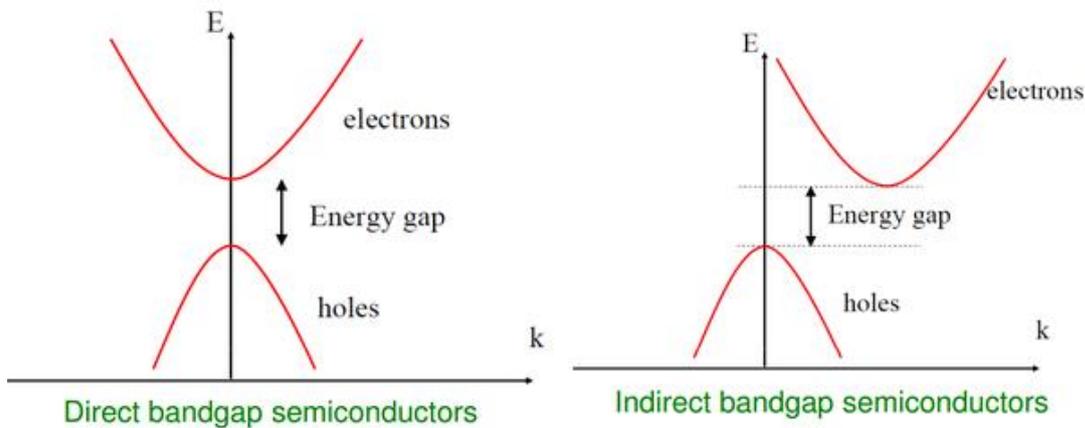
Figure 2.3: Energy-momentum diagrams for a semiconductors a) direct and b) indirect.

Figure 2.3a depicts the direct bandgap, which does not require any changes in the momentum to create an electron-hole pair and is depicted at k=0.

Figure 2.3b depicts the indirect bandgap, which needs a phonon in order to change the momentum of the electron to create an electron-hole pair and is depicted with a displacement in k.

The E-k parabola is used to obtain the effective mass, which is related to the mass of the electron. The interaction between the electron and the extended derived lattice of a real solid have a different curvature for different materials.

The electrons move through the crystal as if they had an effective mass (m^*), which is depicted in equation E2.4 [42].

$$m^* = \hbar^2 \frac{dk^2}{d^2E} = \hbar^2 \frac{k^2}{2E} \qquad \text{[E2.4]}$$

The IR photodetectors is based on the pin junction. The recombination of electrons with holes occurs at the intrinsic region (depletion region), where an absorbed photon will excite an electron from the valence band to the conduction band therefore creating an electron-hole pair. The recombination process is enhanced by defects and impurities in the crystal lattice acting as recombination centre, however, the recombination is bad for the photodetectors because it leads to a reduction in the photogenerated current.

The depletion region is the more effective part of the photodiode for detection and the aim is to increase its width, in order to absorb as many of the incoming photons as possible [31]. The quantum efficiency and frequency response are optimised by calculating the optimum depletion region width in the pin photodiode, making this the reason as to why the pin junction is better than the pn junction.

2.2.4. Introduction to Quantum Theory

The superlattice (SL) structure is a type of multiple quantum well (MQW). The single quantum well (SQW) is the most basic heterostructure, developed as the results of new growth techniques (MBE) allowing control over the growth atomic layer by atomic layer in order to develop well-controlled ultra-thin semiconductor heterostructures. The use of quantum mechanics can predict the probability distribution and then design the semiconductors material control and the material behaviour.

The single quantum well (QW) is analysed using the particle-in-a-box concept. The particle-in-a-box concept applies to the behaviour of an infinite QW, however the equation for a finite QW with boundary conditions is obtained by solving the Schrödinger's equation.

The particle-in-a-box is the one-dimensional potential well containing one particle, where the walls of the well are infinitely high and cannot be penetrated, which is the definition of the infinite QW depicted in Figure 2.4a [40].
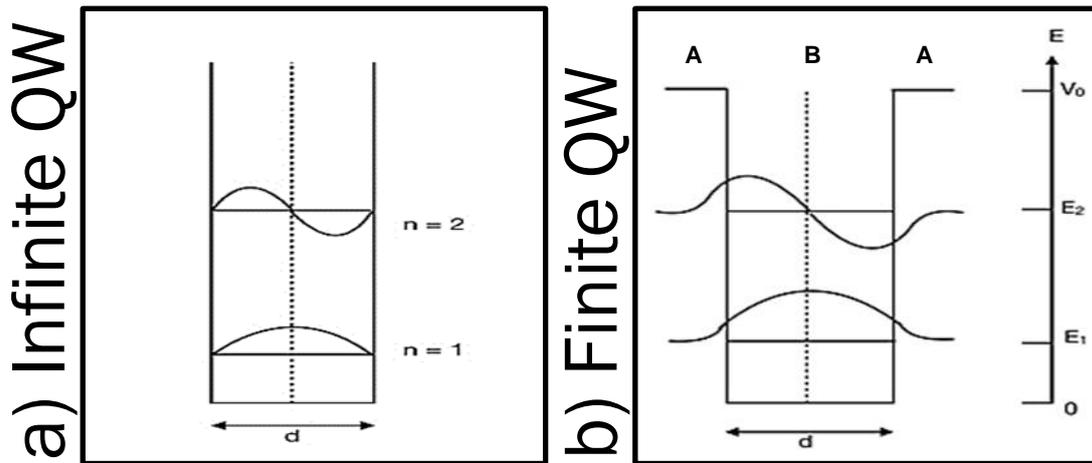
Figure 2.4: Quantum Well Structure a) Infinite and b) Finite

The finite QW has a symmetry around the centre of the well making the solution to the wavefunction, which is depicted in Figure 2.4b.

In order to set the boundaries of the well it is important to consider solving the particle-in-a-box equation by assuming that the potential energy (V) inside the walls is zero, and the resulting equation have the same form as simple harmonic oscillator, which is depicted in equation E2.5 [24].

$$\psi(x) = A\sin\left(\sqrt{\frac{2m_A^* E}{\hbar^2}} * x\right) + B\cos\left(\sqrt{\frac{2m_B^* E}{\hbar^2}} * x\right) \qquad \text{[E2.5]}$$

where $m^*_{(A,B)}$ is the electron effective mass of material A or B, E is the energy, $\hbar$ is the reduced Planck's constant (6.5821×10^{-16} eV s), ψ (psi) is the position-dependent wavefunction, and x is the growth direction.

The first boundary is defined when ψ and x are zero, solving only the sine equation. When the sine equation is zero then x is an integer multiple of π. The second boundary is defined when ψ is zero and x is equal to d (width of the potential well), and this is solved using both equations.

The finite height of the potential barrier allows the possibility of barrier penetration by finding the particle beyond the barrier, which is achieved by normalizing the wavefunction of the particle-in-a-box allowing substitution of A as A = (2/d)^½. Therefore,

changing the height of the well walls from infinite to finite. This allows the energy-levels (eigenfunctions) by rearranging the particle-in-a-box equation, which is depicted in equation E2.6 [40].

$$E_n = \frac{\hbar^2 k^2}{2m_A^*} - V_0; \; E_n = -\frac{\hbar^2 k^2}{2m_B^*}(-V_0 < E < 0) \tag{E2.6}$$

where $m^*_{(A,B)}$ is the electron effective mass of material A or B, E_n is the confinement energy of the carriers, k is the wavevector (k = nπ/d), n is the particle's principal quantum number (integer), and d is the width of the potential well.

2.3. Type 2 Superlattice

2.3.1. Introduction to Superlattice

The superlattice (SL) structure is a type of multiple quantum well (MQW) and occurs when introducing more wells leading to the creation of a continuous band of states. The superlattice DOS (density of state) has a better performance than the 2D (dimensional) DOS. The superlattice DOS has lost their steepness allowing a behaviour closer to 3D DOS, as the 3D is the behaviour of the bulk material.

The superlattice effect introduces a profound change in the 2D density of state (DOS), where the dispersion of the N state destroys the steepness of the square density of state from the energy represented of the MQW. The transition from single QW to multiple QW is defines by N wells giving rise to bands with 2N states. The DOS is the number of available states per unit volume. The DOS of a quantum state E_n is independent of E and the layer thickness.

The superlattice has a finite value at the first level whilst 3D first value is zero. Figure 2.5 [8] compares the difference between a 3D system, a 2D QW system and a superlattice.
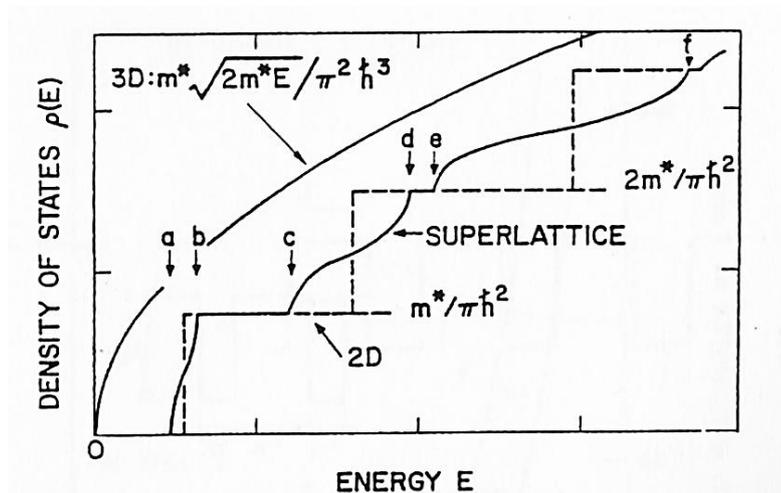
Figure 2.5 Comparison of DOS systems with superlattice

In an ideal superlattice the same barrier is repeated periodically with a period d. The transmission and reflection coefficients of a QW display resonances every time the

condition *kd=nπ* is fulfilled. Therefore, the particle spends a longer time in the QW region.

The decreasing well thickness, creates a new resonant continuum state which pops out of the well whenever a bound state reaches the well top for *kd=nπ* [40]. The resonant continuum states should be of greatest importance in the carrier capture of QW, as the reflection coefficient is near unity for such states.

The movement restrictions of the electrons by the potential well into a finite height modifies the electron wave function by penetrating into the barrier where the amplitude drops exponentially instead of vanishing at the boundary. This effect is the basis of the formation of superlattice, which allows a large number of coupled wells to behave as a quasi-continuous energy band

The way of discovering exactly how thick the quantum wells are before the finite structures resemble an infinite is by looking at the ground state energy as a function of the number of periods. The wavefunction associated with the superlattice is defined by the overlapping due to the adjacent well. However, the wavefunction associated with multiple QW reaches zero between the wells, making this the essential difference between MQW and superlattice, which is depicted in Figure 2.6 [40].
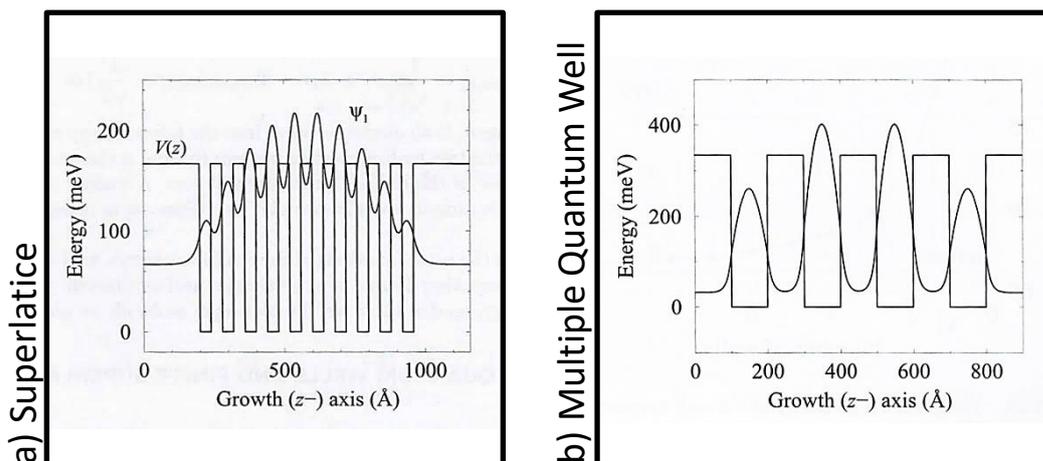
Figure 2.6: The ground state wave function a) Superlattice and b) Multiple Quantum Well

The developments of superlattice are improving the quality of the material, the design of the device structure and the device fabrication in order to create a better photodetector. The superlattice has been chosen as an alternative solution for IR

detectors as a replacement for CdHgTe (Cadmium Mercury Tellurium, CMT), which is the state-of-the-art IR detectors.

2.3.2. Superlattice Photodetectors

The superlattice is a new structure designed to enhance many types of structures at the active region. The way to grow this structure is by engineering the bandgap and designing a well-controlled ultra-thin heterostructures (different structures) using new growth techniques such as molecular beam epitaxy (MBE).

MBE has allowed the creation of more precise structures as more control has been achieved. The superlattice is a structure that consists of two or more ultra-thin layers of semiconductor creating multiple heterostructures built from multiple heterojunctions.

The best superlattice structures are obtained by using materials with a very close lattice match, however, this structure allows for almost any material combination with or without doping to be grown at a rate of one monolayer (ML) per second. If materials have different lattice constants the layers are strained during the growth [25].

This method allows to vary the band structure in the growth direction while tailoring the specification to meet the design requirements regarding electrical and optical specification.

The construction of heterostructures creates interfaces between the materials which have a roughness of around 1ML, when the lattice does not match a dislocation is created. The dislocations propagate into the growing crystal and this reduces its quality, while strains are developed in the crystal around the interfaces [27].

The structure of the photodetector is divided into four parts which includes: substrates, buffer, active region and top contact. This is depicted in Figure 2.7 [6].

    a) The substrate is the base of the photodetector and is made of different material with different crystal structure, such as Si (diamond) and GaAs (zincblende), which are made using other techniques.

b) The buffer removes any defect that the substrate has in the case of GaAs substrate. However, in case of the Si substrate the buffer is used to reduce the dislocation that occurs due to crystal lattice mismatch.

c) The active region is where different architectures are designed depending on the requirements of the photodetector.

d) Sometimes, the passivation is required and is placed between the contact layer and the ohmic contact in order to reduce the surface leakage by creating a chemical bond at the surface.

e) And finally, the top contact layer is designed to create an ohmic contact by using a metal alloy. The contact layer is heavily doped and thin in order to create a good ohmic contacts.
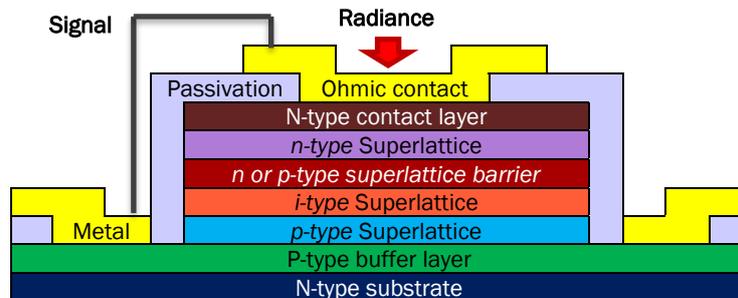
Figure 2.7: The schematic cross section of a single photodetector

2.3.3. Type 2 Superlattice Materials

The type 2 superlattice (T2SL) is classified as a type 2 bandgap alignment. Many new superlattice structure are created based on matching crystal structures and lattice constant.

The semiconductors have their own bandgap and the alignment depends on other semiconductors within the structure. The bandgap alignment is divided into three groups which are type 1 (straddling gap), type 2 (staggered gap and misaligned gap) and type 3 (bulk). The bandgap alignment and the electron-hole movement are depicted in Figure 2.8 [6].
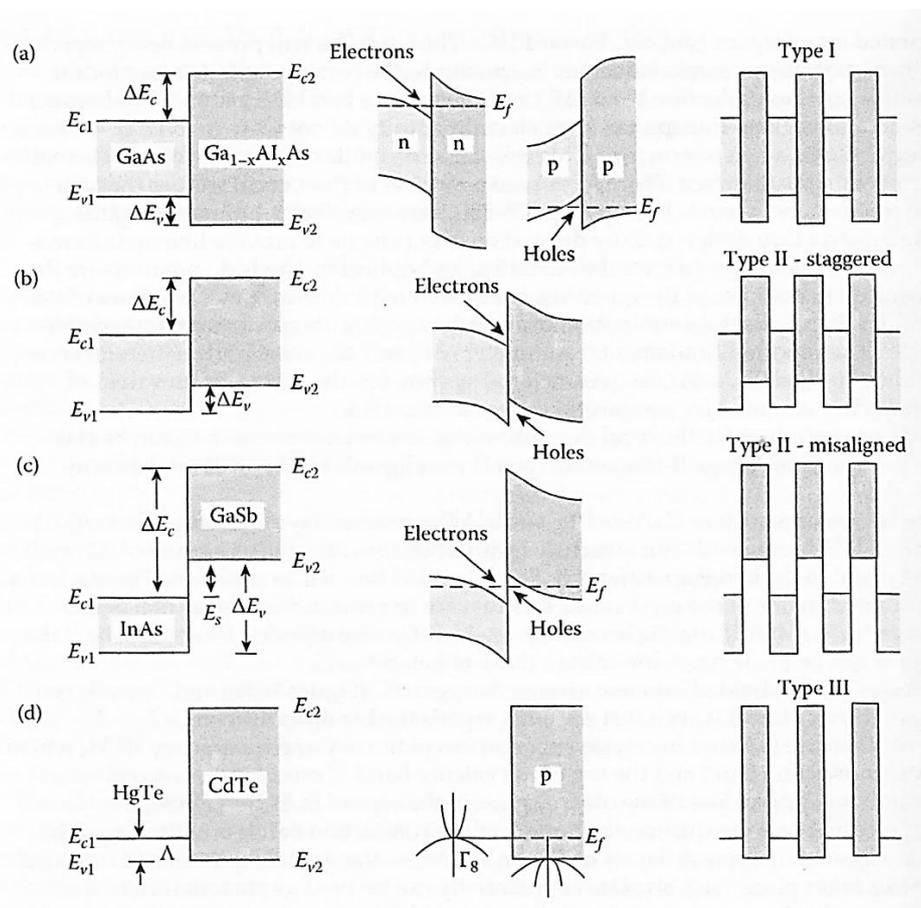
Figure 2.8: Types of bandgap alingment a) Type 1, b) Type 2 (staggered), c) Type 2 (misaligned), and d) Type 3

The type 1 alignment is when the bandgap of material A (left side) is within the bandgap of material B (right side), as depicted in Figure 2.8a. The type 2 alignment is when the bands of material A are lower than the bands of material B. If the conduction band of material A is within the bandgap alignment of material B the type is staggered, as depicted in Figure 2.8b. However, if the bandgap of material A is outside the bandgap of material B the type is misaligned, as depicted in Figure 2.8c. The type 3 alignment is the bulk growth with no visible alignment, as depicted in Figure 2.8d.

New semiconductor combinations are constantly been developed, some of these combinations are listed in Table 2.2 [23]. The most common crystal structures used in the zincblende which has two atoms per unit cell. The semiconductor combination that best fulfil the requirement to develop superlattice structures belong to the 6.1Å family (lattice constant), which are InAs (6.058Å), GaSb (6.096Å) and AlSb (6.136Å).

Table 2.2: Table of most common materials for superlattice

Materials	Bandgap (eV) [i–indirect/d–direct}	Lattice constant (Å)	Electron Effective mass	Crystal structure
Si	1.124 (i)	5.43107	0.26	Diamond
GaAs	1.426 (d)	5.65325	0.067	Zinc blende
InAs	*0.354 (d)*	*6.0583*	*0.024*	*Zinc blende*
GaSb	*0.730 (d)*	*6.0959*	*0.042*	*Zinc blende*
AlSb	*1.615 (i)*	*6.1355*	*0.14*	*Zinc blende*
InSb	0.175 (d)	6.4793	0.014	Zinc blende

The bandgap alignment of these elements with their reference values is depicted in Figure 2.9 [22]. This demonstrates visually which are the best combinations for superlattice: for Type 1 (GaSb/AlSb) and for Type 2 (InAs/GaSb, InAs/AlSb).
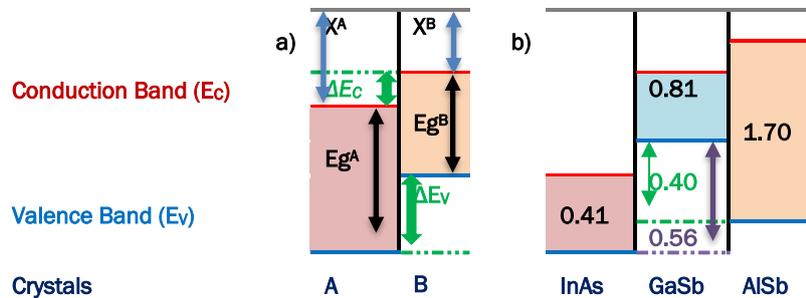
Figure 2.9: Bandgap Alignment a) schematic and b) 6.1Å family

The band alignment of InAs/GaSb T2SL is drastically different from the more widely studied AlGaAs/GaAs system. The energy bandgap of the superlattice is adjusted to form either a semimetal (for wide InAs and GaSb layers) or a narrow bandgap (for narrow layers) semiconductor. The bandgap is determined by the energy difference between the electron miniband (E_1) and the first heavy hole state (HH_1) at the Brillouin zone centre. InAs/GaSb T2SL bandgap varies within a range from 0 to about 400 meV depending on the layer thicknesses and interface compositions [21].

Due to considerably lower electron effective mass ($m^* e$) than the hole effective mass ($m^* h$), the E_1 band is more sensitive to layer thickness than the HH_1. The thickness of the GaSb layers has a negligible effect on the T2SL bandgap due to the large value of the GaSb HH mass (~0.41mo). However, the thickness of the GaSb has a significant impact on the conduction band (CB) dispersion due to penetration of the InAs electron wave functions into the GaSb barriers. Since InAs is not lattice-matched to GaSb the bandgap of T2SL depends on strain effects [41].

The InAs/GaSb T2SL is characterised by a broken-gap alignment. The optical transition between highest hole (heavy-hole, HH_1) and the lowest conduction minibands is employed for the detection of incoming IR radiation. The InAs/GaSb T2SL alignment is depicted in Figure 2.10 [11].
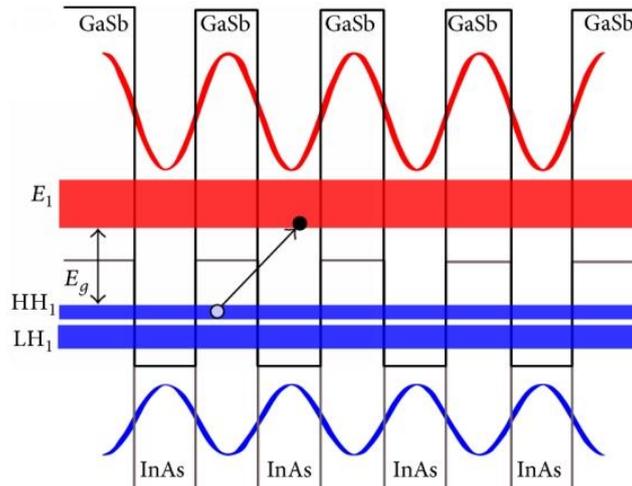
Figure 2.10: T2SL band alignment of InAs/GaSb

2.3.4. Type 2 Superlattice Infrared Architectures

The new architectures are developed using the pin structure as a starting point with the developments taking place at the active region.

The **basic structure** for the active region is the *pin*, which is read from bottom to top. With this in mind the next basic structure is *nip*, which is built as described. In either case, the quantum efficiency is dependent directly on the thickness of the depletion region.

The **unipolar barrier** blocks one type of carriers (electron or hole) and allows the other type to pass through. The barrier structure has a significant reduction of dark current and a higher operating temperature [21].

The barrier needs to be a close lattice match to the rest of the structure, therefore, the best barrier for the growth of InAs/GaSb is InAs/AlSb, as this is also of the type 2 alignment. This barrier can be either *pBp* or *nBn* depending on the specification

requirements of the designed, which are depending on the applications and is depicted in Figure 2.11 [23].
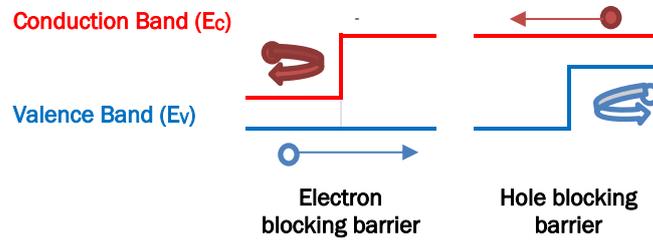
Figure 2.11: Illustrations of electron and hole-blocking unipolar barriers

The **M-structure** reduces the dark current significantly while demonstrating low effect on the optical properties, which is depicted in Figure 2.12a [46]. While, the **N-structure** increases the electron-hole pairs under bias therefore increasing the absorption while decreasing the dark current, which is depicted in Figure 2.12b [16].

The M and N structures are named after the shape of the bandgap alignment of the layers created within the structure from using InAs, GaSb and AlSb alloys.
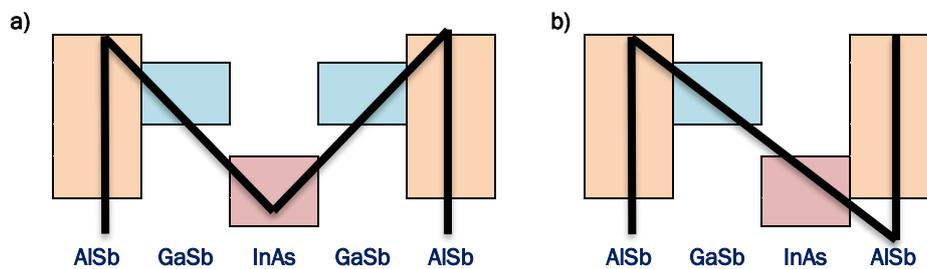
Figure 2.12: Schematic bandgap diagram a) M and b) N structure

The main difference between both structures is the position of the AlSb layer. In case of the M-structure, the AlSb layer is situated at the border of the structure creating a symmetrical formation. While in the case of the N-structure, the AlSb layer is situated at just one border of structure creating an asymmetrical structure.

With every new architecture, the design gets more complex and with this their results get closer to the state-of-the-art CdHgTe photodetector. The comparison of the architecture depicted in this chapter demonstrates the improvement that every new architecture has to the overall performance of the photodetector.

The scope of comparison is focused on InAs/GaSb T2SL IR detectors grown on GaAs substrates for medium wavelength (mid-wave) IR (MWIR) applications. The comparison between an M-structure, a unipolar barrier and a pin, which are depicted in Table 2.3.

Table 2.3: Structures and designs for M-barrier, unipolar barrier and pin

Structure and Design Parameters	M-Barrier [12]	Unipolar-Barrier [3]	pin [28]
Growth technique	MBE	MBE	MBE
Buffer (size & material) [μm]	0.5	0.35/ GaSb	2.5/ GaSb
Bottom contact (size & material) [μm]		0.52/ SL [10ML InAs/10ML GaSb]	1/ p-GaSb
Structure architecture	M Barrier (pπMN/piMn)	Barrier (nBn/niBn)	pin
Construction of superlattice [InAs/GaSb]	6.5ML/ 12ML	10ML/ 10ML	8ML/ 8.3ML
Other structure	10 InAs/ 1 GaSb/5 AlSb/ 1 GaSb (slightly doped @790°C)	[0.1μm AlGaSb]	
Top contact (size & material) [nm]	500		6/ n+ InAs

All structures were grown using MBE over GaAs substrates, allowing a close comparison. The GaAs substrate allows direct growth due to their matching crystal structure and close lattice match. The main differences between these detectors are the structure, which covers from the basic *pin* structure to the most complex *M-barrier*.

Chapter 3: Methodology

3.1. Introduction

This chapter provides detailed description of every piece of equipment, technique and process required to build and test all the architectures developed for this project.

The type II superlattice (T2SL) detectors is grown using a combination of elements from group III-V (3&5). The development of the T2SL takes advantage of modern growth technologies such as molecular beam epitaxy (MBE), as this helps grow large format focal plane arrays (FPA) with great uniformity [19]. T2SL IR detectors are defined by their staggered band alignment and are based on a pin structure, which has an intrinsic region between two heavily doped layers of the device (n-region and p-region) [1].

The InAs/GaSb (indium arsenic/ gallium antimony) superlattice (SL) is the most common combination used in T2SL structure for developing IR detectors, as it is able to cover the entire IR spectrum from 1 to 30μm. All the layers of the growth are based on InAs/GaSb composition and the only way to establish their specific characteristics is by manipulating the thickness and the doping of each layer. The entire process is depicted in Figure 3.1.

Moleculara Beam Epitaxy

Material Characterisation
- X-ray diffraction
- Atomic force microscope
- Photoluminescence

Device Fabrication
- 1st photolithography
- Mesa etching
- 2nd photolithography
- Passivation etching
- Metallization

Electrical and Optical Testing
- Dark current
- Quantum efficiency
- Responsivity
- Specific detectivity
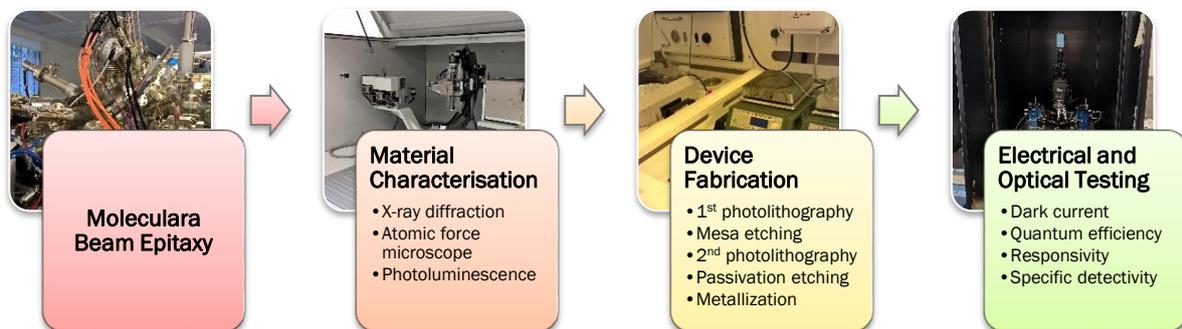
Figure 3.1: T2SL process layout

3.2. Molecular Beam Epitaxy

Molecular beam epitaxy (MBE) is an epitaxy method for thin-film deposition of single crystals, which uses an ultra-high vacuum (UHV) based technique for producing high purity epitaxy structures. The deposited film creates epitaxial layers, which can be made from the same material (homoepitaxy) or from different materials (heteroepitaxy). The layers are grown from materials that have a similar lattice constant to themselves and to the substrate, and if not, some dislocations may occur.

The MBE machine consists of a vacuum chamber, a pressurised chamber for the substrate holder (UHV), a substrate heater, several effusion cells with shutters (containing ultra-pure elements), an in-situ cleaning, and an in-situ reflection high-energy electron diffraction (RHEED) analyser (consisting of a gun and a fluorescent screen). This is depicted in Figure 3.2 [26].
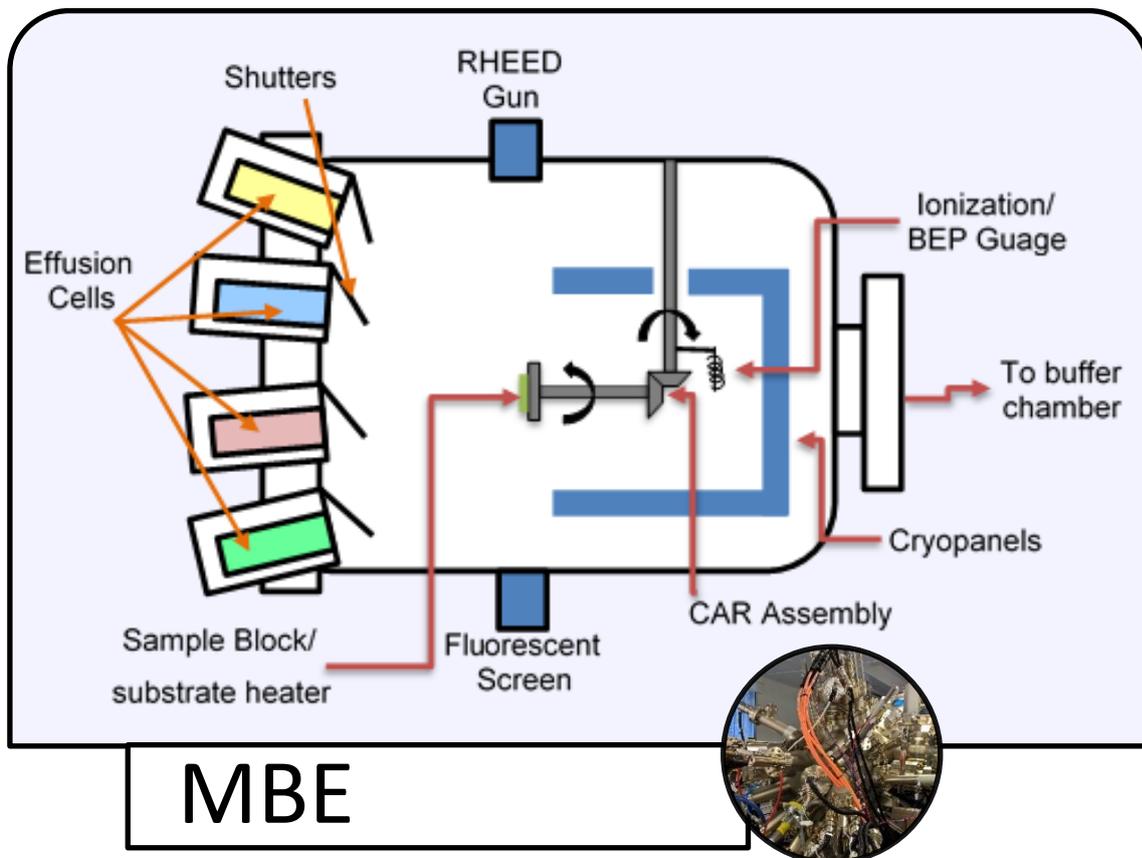
Figure 3.2: MBE system chamber

The UHV environment of the MBE is achieved through various cryogenic pumps and a cryopanel created using liquid nitrogen. The cryopanel removes the heat from the system and traps the impurities surrounding the substrate preventing these from interfering with the growth process. The effectiveness of the UHV is enhanced by the vacuum chamber, which helps avoid the oxidation of the source materials.

The MBE is a well-controlled machine thanks to the use of UHV technology. The low growth rate (one monolayer per second) and low temperature (due to the liquid nitrogen within the chamber) are important for precise thickness control, sharp interfaces (monoatomic), and negligible dopant distribution.

The growth rate can be kinetically controlled. The substrate is uniformly heated to an appropriate temperature allowing surface diffusion of molecular species in order to find appropriate lattice sites [26]. The heating is achieved by radiation and the constant rotation helps to smooth the non-uniformities due to the off-axis source.

The effusion cells produce a beam, which is defined by evaporated atoms that are isolated from each other until they meet on the substrate. The effusion cells contain ultra-pure elements like gallium ingot (Ga 8N, 99.99% purity) and arsenic ingot (As 7N5, 99.99% purity), which are vaporised and then condensed onto the substrate where they react with each other. The substrate is placed on the substrate holder inside the UHV where the substrate is heated and the evaporated atoms move around it until they find a site to chemically bond to.

The effusion cells' shutters allow a precise control of the thickness of each layer, up to a single atom by turning the beam flux on and off. The flux of atoms is controlled by the temperature of the effusion cells.

The MBE has an in-situ cleaning process that uses low-energy sputtering with an ion beam of an inert gas. It also has an in-situ analyser employing RHEED containing phosphorous compounds, which are difficult to manipulate and are highly volatile.

The RHEED monitors the growth of the crystal layers, which is a high-energy beam directed at the sample's surface at an angle. Then the electrons are diffracted by the

crystal structure of the sample and then attached onto a phosphorus screen mounted opposite to the electron gun. The expectation is a series of streaks where a sharp pattern indicates a flat surface, if not the pattern is more diffused.

The T2SL fabrication starts with the design of the architecture, which is then grown using the MBE. The superlattice consists of monolayers (ML) grown by MBE. The MBE structure is grown depending on which type of IR detector is being designed for. Once the MBE structure is grown, the next step is the material characterisation and after this the architecture is ready for device fabrication.

The MBE is associated with low-dimensional structures [26] due to its ability to deposit ultra-thin layers up to a single ML. Therefore, the superlattice idea comes from creating a large number of alternating ultra-thin layers in which the electrons could tunnel through the wider gap in order to interact with the periodic potential of uniformity due to their crystal lattice.

3.3. Material Characterisation

After the growth, the next step is called the material characterisation. These comprise a set of measurements carried out on the grown wafer in order to analyse the structure in a non-invasive way. These measurements include: x-ray diffraction, atomic force microscope, and photoluminescence.

3.3.1. X-Ray Diffraction

The x-ray diffraction (XRD) is a technique that determines the composition of the materials used within the structure. The XRD measures the diffraction pattern of each component when an x-ray interacts with an atomic array in the crystal that can be diffracted, as the wavelength of the x-ray is comparable with the interatomic distance in the crystals.

The XRD machine is divided into three parts: an x-ray beam, a sample holder, and an x-ray detector. This is depicted in Figure 3.3.
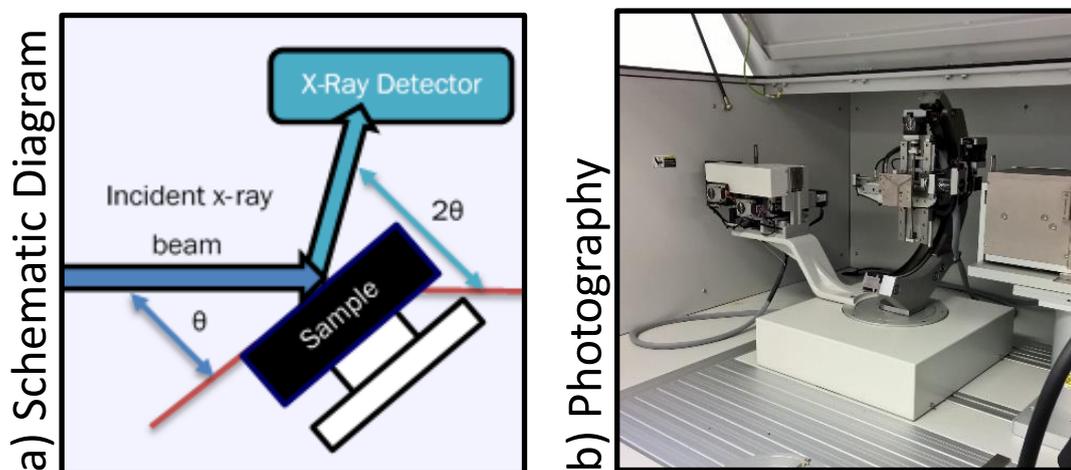
Figure 3.3: X-Ray Diffraction Machine

The XRD works by generating a monochromatic x-ray into an incident beam, which interact with the materials of the sample by scattering the x-rays from the atoms within the sample, and then are gathered at the detector.

The x-ray incident beam strikes parallel planes of atoms which are scattered by the atoms inside. This means that at certain incident angle θ (theta), the light-path difference of scattered waves can satisfy Bragg's law, allowing the interference of the scattering light to create a peak intensity. This is also called diffraction. Bragg's law is depicted in equation E3.1 [9].

$$n\lambda = 2d\,sin(\theta)$$
[E3.1]

where *n* is the order, λ (lambda) is the wavelength of the x-ray, *d* is the lattice spacing, and θ is the diffraction angle. This measurement principle is depicted in Figure 3.4 [9].
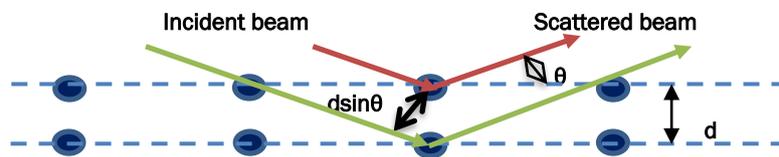
Figure 3.4: XRD measurement mechanism

In practice, the wavelength of the x-ray has a fixed value allowing the creation of multiple planes with an interplanar spacing producing a diffraction peak at a specific angle. The space between the diffracting planes determines the peak position, as the spacing is determined by the material composition.

In case of the superlattice structure, the XRD measures the multilayer structure and this is depicted by additional peaks around the main diffraction peaks, which are called fringes. The number of fringes gives the total number of layers within the superlattice. The main peaks within the superlattice are given by the period thickness. The slope is given by the interface roughness for each layer within the superlattice.

The resulting diffracting pattern has a lot of information, which defines the parameters of the layers such as: the composition, lattice mismatch, defects, thickness, strain, interface quality, and uniformity. This allows to verify the composition and the lattice mismatch between the layers.

3.3.2. Atomic Force Microscopy

The atomic force microscope (AFM) is a scanning probe microscope, which measures the surface quality by creating a 2D model of the structure to verify the heights and widths.

The AFM machine is divided into four parts: a laser, a cantilever with a tip, the sample holder, and a photodiode. This is depicted in Figure 3.5.
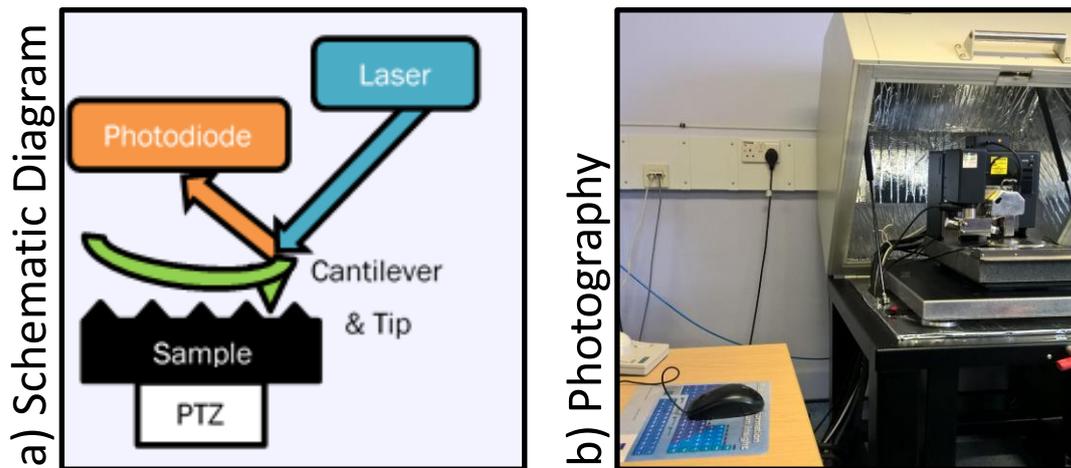
Figure 3.5: Atomic Force Microscopy Machine

The AFM measures the force created between the tip placed at the end of the cantilever and the sample, which is created by lateral and vertical deflections using an optical lever, this motion is called tapping. This is operated by reflecting a laser beam off the cantilever, for this the laser and the tip should be in perfect alignment.

The resulting image has two components: the magnification (1 to 10µm) and the number of pixels (30x30). The AFM is the main technique used to analyse the morphology of the top epitaxial layers.

3.3.3. Photoluminescence

The photoluminescence (PL) is an optical technique, which measures the bandgap energy of material from the wavelength of the emitted light following the absorption of photons both temperature and power-dependent PL measurements can be performed.

It also allows a detailed analysis of the band structure, and their imperfections (defects and impurities) within the sample.

The PL installation consists of a light source (532nm laser), an optical chopper (interrupts the laser beam), a focusing lens, a sample holder (inside a cryostat with a helium (He) compressor cooling system), a set of focusing lenses, a monochromator (with a bandwidth of 1 to 5µm), and a photodetector (connected to lock-in amplifier and then a computer). The lock-in amplifier is designed to use its internal oscillator to measure the amplitude of the input signal. This setting is depicted in Figure 3.6.
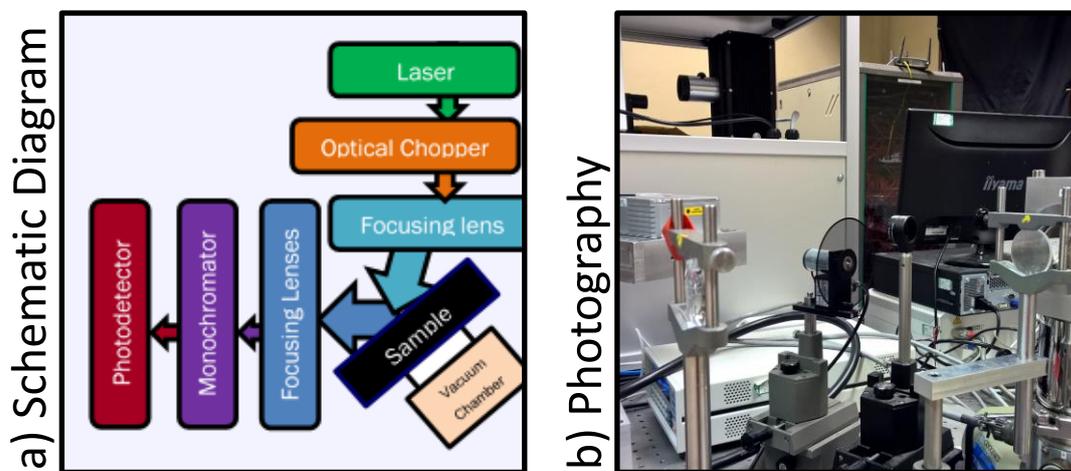
Figure 3.6: Photoluminescence setting

Before starting the measurements, the sample is placed inside the chamber and once inside, the vacuum pump is turned on. Once the vacuum is obtained, the laser is set to a photon energy level higher than the bandgap of the material to be measured.

The PL measures the energy of emitted photons, therefore, the energy levels of the impurities within the sample can be obtained. These photons help the electron to jump into the conduction band in order to generate electron-hole pairs. After this, the electron relaxes back into the valence band and during this process they emit radiation that is detected by the optical receiver. The typical measurements taken are either power-dependent or temperature-dependent.

The temperature dependent measurements are taken from room temperature (as band to band recombination dominates the emission) to low temperatures (up to 10K), as the peak width is decreased due to the fact that the thermal recombination is supressed

and carrier interactions are limited. These measurements help describe the carrier confinement barriers. Increasing the temperature of the sample allows some electrons to thermally escape and this emission can be measured.

The power-dependent measurements help check the crystal quality of the material. The high value (higher than 400mW) means that the radiative recombination dominates, as the defects usually contributes towards the non-radiative recombination. These measurements are taken at different values allowing to extrapolate the band structure and their effects such as quantum confinement by inducing energy levels splitting.

3.4. Device Fabrication

After the material characterisation, the next step is the device fabrication. The equipment required is depicted in Figure 3.7 and is found inside a standard cleanroom.
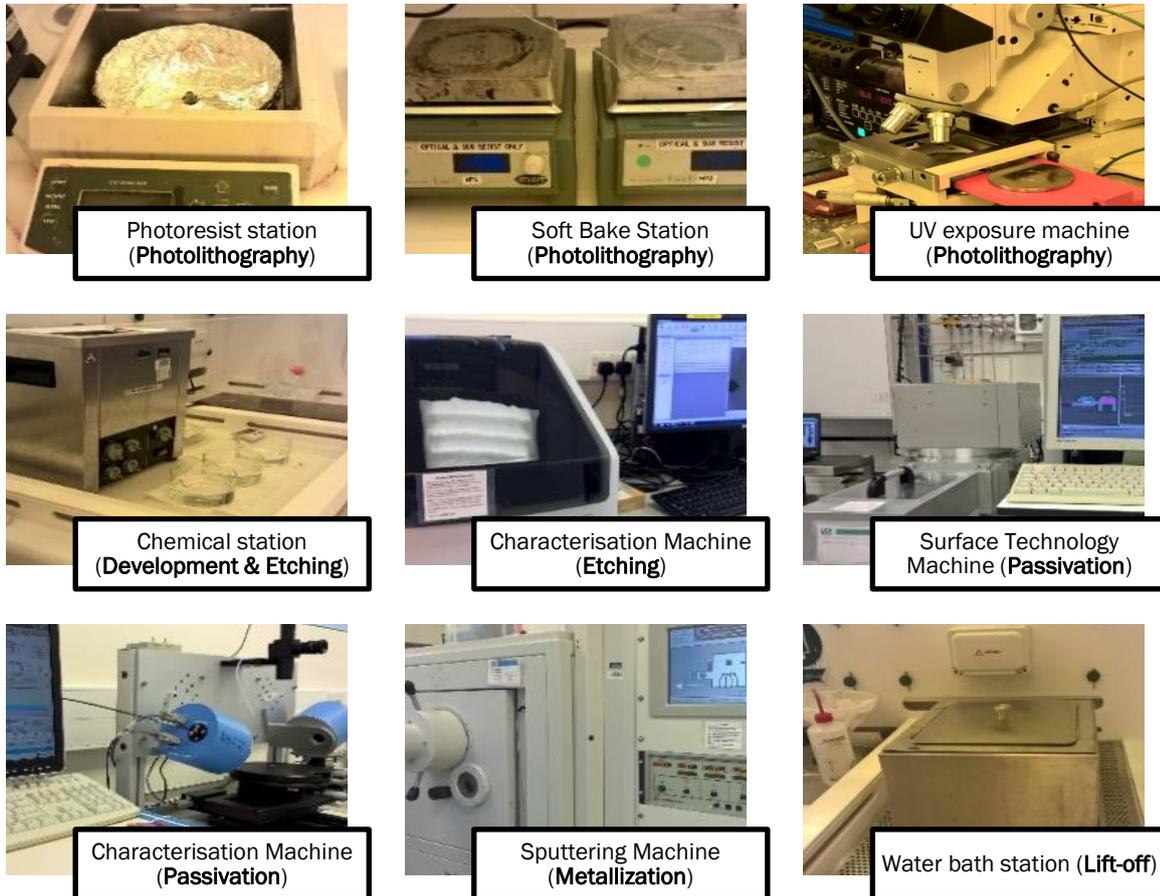
Figure 3.7: Device fabrication process equipment

During the device fabrication process, the structure is chosen depending on the designed application from simple mesas to more complicated devices.
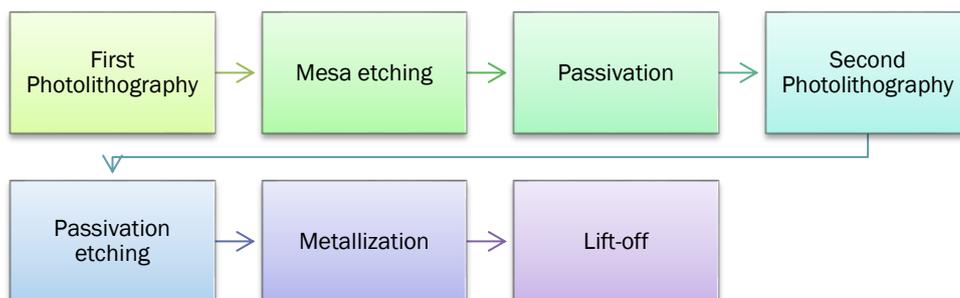
Figure 3.8: Device fabrication process step-by-step

However, regardless of the structure selected, and their many variations within each step depending on the requirements and the materials, each step remains the same making this process a standard procedure for all device fabrication. The process is depicted step-by-step in Figure 3.8.

Once this device fabrication is completed, the cross-section of a single photodetector is depicted in Figure 3.9.
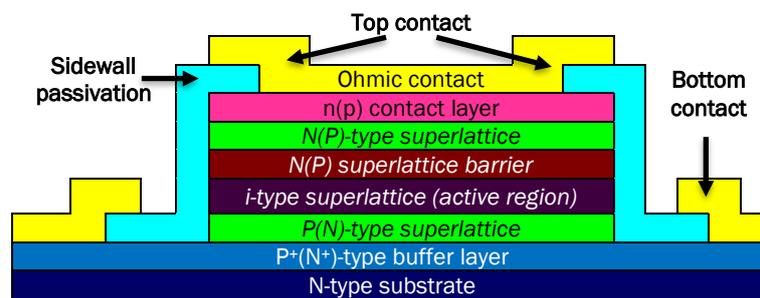
Figure 3.9: The schematic cross section of a single photodetector

3.4.1. Photolithography

The photolithography is a chemical process that creates patterns (photomask) using a light source. The advantages of the photolithography lie in the fact that the leveraging patterns (created structures) can be very small, well defined and easy to replicate. The disadvantages are that the process is slow, and there is a possibility of contamination, low density and defect formation.

The most important piece of equipment for the pattern creation is the photomask. The design's complexity is defined by the application it is being used for. Most of the photomasks include all the patterns required to create the photodetector. This means that there is a pattern for creating the mesa and for various connections of metal options, all depending on the overall design.

The photolithography consists of three steps: application of photoresist, the exposure to UV lights, and the development. The equipment needed to accomplish these steps is depicted in Figure 3.7.

The first step is the application of the photoresist. There are two types of photoresists: negative and positive. This defines which part of the photomask is removed. If the photoresist is positive, the part that has been exposed with the UV light is the one that is removed. If the photoresist is negative, the part that has been exposed is the one that remains.

For the application of the photoresist, the sample is placed in the middle of the spinner machine. The photoresist is a chemical that is applied over the sample using a plastic pipette, making sure that the photoresist covers the complete sample. The spinner allows the photoresist to thin down with the thickness of the photoresist depending on the speed of the spinner. Once the photoresist has been applied it needs, to be soft baked.

The second step is the exposure of the photomask to the UV light. The difficult part of this is to align the sample with the photomask. It is important to remember to place the side of the photomask where the drawing is just on top of the sample. The photomask needs to be held in place with vacuum in order to avoid the sample to move in the middle of the process. Once the photomask is in the correct position, the last step is to turn on the UV light and expose the sample. Special goggles should be worn to protect the eyes from the dangers of UV radiation.

The final step is the development, which is a chemical reaction that allows the photoresist to produce a visible image, as everything so far has been done under UV light. The development is a two-step process: apply the developer and then stop the chemical reaction.

The above steps constitute the standard steps for using during every photolithography. The major difference is the mask alignment, as the first application does not have any restriction. However, during the second photolithography, both masks have to be completely aligned with the alignment marks laid down in the first photolithography step. Therefore, it is important to design various alignment marks around the structure in order to achieve a accurate alignment.

As described before, the first photolithography will set the shape and size of the mesas, which can be either square or circular in shape with a size between 25 to 500µm. The second photolithography will create the windows for the ground contacts, as the basis of the metallization process.

3.4.2. Etching

The etching is a chemical reaction used to define the patterns created by the photolithography. There are two parts to achieve a successful etching: the first one is to choose the chemical reaction (either wet or dry) and the other is to achieve the desired depth.

As mentioned before, the etching can be achieved by two types: dry or wet. The wet etching is achieved by dipping the sample into a chemical mixture, which is depicted in Figure 3.7. The chemical mixture is customised for each material. Each chemical mixture has an etching rate which allows us to calculate the time the sample needs to be submerged in the chemical mixture in order to achieve the desired depth. After the calculated time, the depth needs to be measured accurately making sure that the correct depth has been achieved. The measurement is done using a profiler (Dektak XT), which is depicted in Figure 3.7.

The dry etching is a more controlled process, as it uses a plasma machine. The dry etching is done inside a pressure chamber where the gases are introduced in a set order depending on the material that needs to be etched. It is important to be exact about the etching rate as once the sample is inside no further changes can be made if the rate is not accurate, the etching could go beyond the desired depth.

3.4.3. Passivation

The passivation process consists of applying a microcoating around the structure in order to avoid a corrosive chemical reaction with the base material and reduce the surface recombination. The ideal passivation is electrically neutral and has a very low density on surface states. Therefore, the ideal passivation is a widegap insulator grown with no fixed charge at the interface [20]. The surface of actual devices is passivated

in order to stabilise the surface against chemical and heat-induced changes as well as to control surface recombination, leakage, and related noise.

The passivation has been classified into four types depending on the material:

a) dielectric passivation deposition (silicon nitride (Si_3N_4), silicon dioxide (SiO_2)),

b) SU8 deposition,

c) chalcogenide passivation deposition (ammonium sulphide (($NH_4)_2S$) or zinc sulphide (ZnS)),

d) and electromechanical passivation (sulphur (S)) [13].

The SU8 deposition is the fastest passivation to apply as its application has the same steps as when applying any photoresist (coat, soft bake, expose, and develop). However, SU8 is a permanent epoxy making this the main difference between the SU8 and a photoresist. Therefore, it requires a different remover PG (N-methyl-2-pyrrolidinone and surfactant) for etching.

The most commonly used passivation for T2SL is the dielectric passivation SiO_2. The objective of this passivation is to render the surface inert, in order to avoid any chemical reaction with air or other materials that make contact with the surface, so that the properties of the semiconductor are not changed.

The dielectric passivation is carried out using a plasma-enhanced chemical vapour deposition (PECVD), which is depicted in Figure 3.7. The PECVD machine consists of: a chamber containing six gases (nitrogen, oxygen, silane, ammonia, nitrous oxide, and hydrogen). The combination of silane and nitrous oxide is required to create SiO_2.

It is important to measure the thickness of the passivation in order to verify if the desired design thickness was achieved. The problem with the passivation is the layer covers the entire sample making it impossible to measure using the sample. Therefore, the way to measure the thickness of the passivation is to add a test sample with the only purpose of measuring the thickness. The thickness is measured by a characterisation machine (MM15 Control Unit), which is depicted in Figure 3.7.

3.4.4. Metallization

The metallization process consists of creating a layer of metal deposition in order to create ohmic contact for use on integrated circuits and as detectors. The metallization involves applying a thin film layer of metal in order to create a combination of metals by controlling the order of the materials and their thickness.

The metallization process is carried out using a sputtering machine, which is depicted in Figure 3.7. The sputtering machine consists of a chamber containing up to four metals like titanium (Ti), platinum (Pt) and gold (Au) inside individual targets.

The samples are stuck to a wafer holder using a cleanroom tape and then placed inside the chamber. The sputtering can only occur after the pressure of the chamber has been reached vacuum, which takes around eight hours.

After the chamber reaches -7 torr, sputtering can start. The sputtering occurs when an ionized gas molecule displaces an atom of the material to create a plasma at an atomic level. The plasma strikes a target of the selected material and then bonds with the atoms of the substrate in order to create a thin film layer. After achieving the desired combination of elements, the chamber needs to be vented in order to return to normal pressure and during this time the wafer cools down.

The resulting coating is thin, uniform, and with an unbreakable bond. However, the coating covers the entire wafer holder and it only needs to be in certain areas. Therefore, the final step is a chemical lift-off. The highlights of the process are depicted in Figure 3.10.
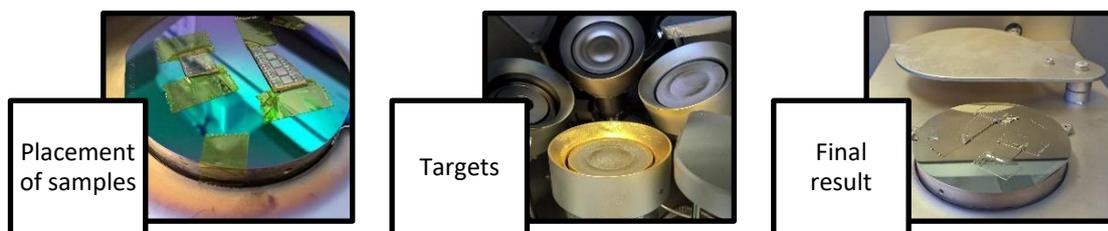
Figure 3.10: Metallization process

3.5. Electrical and Optical Characterisations

After the device fabrication, the electrical and optical performance needs to be characterised and for this a standard set of metrics have been compiled. This is because every device has been created in a unique manner from the material chosen during growth to the material applied during the fabrication, and the only way to compare the results is by using these metrics. These results allow comparison of the performance of every device under the same metrics.

These metrics [14] are:
1. for the electrical characterisation is the dark current density (J_{dark});
2. and for the optical characterisation are
    2.1. Responsivity ($\mathscr{R}$),
    2.2. Quantum efficiency (η or QE), and
    2.3. Specific detectivity (D*).

However, due to the close relationship between responsivity and quantum efficiency, it is possible to measure one metric and then use these values to calculate the other metric.

3.5.1. Dark Current

Dark current density (J_{dark}) is a small current that the device produces in the absence of light. The saturation current occurs when the reverse bias (V<0) is applied and this is defined as dark current. The dark current (J_{dark}) is obtained in reverse bias form and is equal to -J_0. The overall current-voltage (I-V) characteristics of a photodiode can be depicted as the sum of the photocurrent (J_{sc}) and the dark current, and is depicted in equation E3.2 [47]. The dark current density is measured in amperes per square cm (A/cm^2).

$$J = J_{SC} - J_0\left(e^{qV/kT} - 1\right) \qquad \text{[E3.2]}$$

where J_0 is the saturation current, k is the Boltzmann's constant (1.38×10^{-23} Joules/Kelvin (J/K)), q is the electron charge (1.6×10^{-19} Coulombs (C)), V is the applied voltage (V), and T is the temperature in Kelvin (K).

The photocurrent and dark current flow in the same direction when reverse bias is applied. The dark current can be obtained by using a parameter analyser (Keithley 460A), which generates a I-V graph.

The photocurrent can be obtained by using a spectrum analyser (SR770) as part of an installation which includes a light source (IR), a preamplifier (SR570), and a sample holder (variable-temperature cryostat).

3.5.2. Responsivity

Responsivity ($\mathcal{R}$) is the relationship between the output signal and the input optical power, which could be either voltage or current responsivity and is depicted in equation E3.3 [20]. The responsivity is measured in volts or amperes per watt (V/W & A/W). The responsivity measures the detector's sensitivity to light.

$$\mathcal{R}_I = \frac{I_{out}}{P_{in}} \ \& \ \mathcal{R}_V = \frac{V_{out}}{P_{in}} \tag{E3.3}$$

where I_{out} and V_{out} are the output signal, and P_{in} is the input optical power. The responsivity can be obtained by using a spectrometer (Thermo Fisher Nicolet IS50) as part of an installation which includes a light source (blackbody), a preamplifier (SR570), and a sample holder (variable-temperature cryostat).

3.5.3. Quantum Efficiency

Quantum efficiency (η or QE) is the relationship between the number of electron-hole pairs produced and the photons absorbed, and is depicted in equation E3.4 [20]. The ideal QE is 1.

$$\eta = \frac{N_e}{N_v}(100\%) = \mathcal{R}\frac{hv}{q} = \mathcal{R}\frac{hc}{q\lambda} \qquad \text{[E3.4]}$$

where N_e is the number of electrons produced, N_v is the number of photons absorbed, q is the electron charge, h is the Planck's constant ($6.63{\times}10^{-34}$ Joules second (J s)), v is the frequency of light, c is the speed of light in vacuum ($3{\times}10^8$ meters per second (m/s)), $\mathcal{R}$ is responsivity, and λ is the wavelength of the photon.

3.5.4. Specific Detectivity

Specific detectivity (D*) allows to compare the detectors of the same type but with different areas, and is depicted in equation E3.5 [20]. The specific detectivity is the only figure of merit which measures the noise performance of the photodetector.

The specific detectivity is measured in Jones or centimetre square root of Hertz per watt (cm Hz^{½}/W).

$$D^* = \frac{\sqrt{A_d \Delta f}}{NEP} = \frac{\mathcal{R}_V \sqrt{A_d \Delta f}}{V_n} = \frac{\mathcal{R}_V}{\sqrt{2qJ_{dark} + \frac{4Tk}{R_0 A}}_V} \qquad \text{[E3.5]}$$

where A_d is the active detector area, Δf is the bandwidth, and NEP is the noise equivalent power, J_{dark} is dark current, k is Boltzmann's constant, T is operating temperature, $R_0 A$ is resistance area product at zero-bias, $\mathcal{R}$ is responsivity, and q is electron charge.

Chapter 4:   High quality T2SL detectors on Si and GaAs substrates

4.1. Introduction

This chapter compares the performance of the basic nip structure and its behaviour on both GaAs and Si substrates. In order for this comparison to work, the nip structure is exactly the same in both cases.

The aim was to analyse the behaviour of a common structure grown on different substrates in order to understand the contribution that the Si substrate has to the structure. This was the first structure ever grown on Si substrate using MBE.

The structure grown on GaAs substrate will be used as the benchmark for comparison, as all materials share the same zinc blend structure (substrate and architecture). Although, GaAs has a lattice mismatch with regards to the rest of the structure, it shares the same crystal structure and belongs to the same semiconductor group (group III-V). GaAs (with a lattice constant of 5.653Å), is one of the substrates used for T2SL as it has a lattice constant closest to Si (5.431Å). The expectation is that this will create similar dislocations during the growth.

The nip structure is the same on both substrates. The only difference is the construction between the substrate and the nip structure which is attributed to the different crystal structures of both Si (diamond) and GaAs (zinc blend). The Si substrate sample required a nucleation layer to reduce the dislocation mismatch between the buffer and the substrate.

After the growth, the material characterisation measurements were carried out by myself with minor supervision at UCL premises. The fabrication process was carried out by myself at the cleanroom laboratory of London Centre for Nanotechnology (LCN). However, the electrical and optical testing were carried out by Shanghai Tech University, which is outside the UCL premises.

4.2. Methodology

4.2.1. MBE growth details.

The structures were grown in a Veeco GEN930 solid-source MBE by the MBE group based at UCL and are depicted in Figure 4.1 [43].

The T2SL photodiode consists of periods of 10ML GaSb, 10ML InAs and 1ML In. The InSb layer is grown for strain balance due to the fact that the lattice constant of InAs is 0.75% smaller than that of GaSb.

a) GaAs substrate

50nm p+ GaSb
500nm of p-type [10ML GaSb/10ML InAs] SL
2,000nm of i-region [10ML GaSb/10ML InAs] SL
500nm of n-type [10ML GaSb/10ML InAs] SL
1,000nm GaSb buffer
200nm N+ GaAs buffer
N+ GaAs Substrate

b) Si substrate

50nm p+ GaSb
500nm of p-type [10ML GaSb/10ML InAs] SL
2,000nm of i-region [10ML GaSb/10ML InAs] SL
500nm of n-type [10ML GaSb/10ML InAs] SL
500nm GaSb buffer
100nm buffer [10ML AlSb/10ML GaSb] SL
500nm GaSb buffer
100nm buffer [10ML AlSb/10ML GaSb] SL
10nm AlSb
N+ Si Substrate
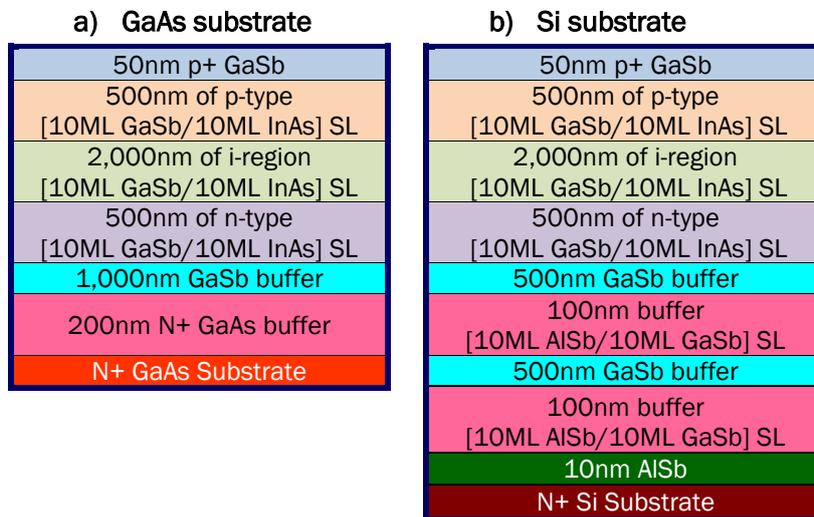
Figure 4.1: Epitaxial layer structures of a) GaAs and b) Si architecture

In the **Si architecture**, all epi-layers were directly grown on a Si (100) substrate by MBE, with a 4° offcut towards the [001]. Before the epitaxy growth, the Si substrate was heated in the ultra-high vacuum at 900°C for 30min in order to fully remove the surface native oxide. After the deoxidation, the substrate was cooled down to 400°C in order to grow a 10nm AlSb nucleation layer. After the nucleation layer, the temperature was raised to about 500°C in order to grow the buffer. The buffer consisted of a two-block structure of 100nm superlattice with each period consisting of 10ML AlSb and 10ML GaSb, followed by 500nm GaSb.

After the buffer, the substrate was cooled down to 400°C in order to grow the T2SL structure. The epitaxial layer structure of the nip photodiode (as it is read from bottom to top), consists of an n-doped bottom contact of 500nm (82 periods), an intrinsic region

of 2µm (329 periods), and a p-doped top contact of 500nm (82 periods). After the structure, a heavily p+ doped 50nm GaSb cap layer is grown for good ohmic contact property.

The **GaAs architecture** was grown as a reference, where all epi-layers were directly grown on GaAs (001) substrate. After the deoxidation, the substrate was cooled to 590°C in order to grow a smooth layer of 200nm GaAs. Then the substrate was cooled further to 500°C in order to grow a buffer of 1µm GaSb. After the buffer, the T2SL photodiode architecture is grown which is the same as the one from the Si substrate including the cap layer.

4.2.2. Device fabrication.

The first device fabrication was carried out at the cleanroom facilities of the London Centre for Nanotechnology (LCN) over a five-day period. The step-by-step fabrication process is depicted in Figure 4.2.

Part 1 is creating the mesa structures by using photolithography, which is used for device preparation and first photolithography. The Si sample perimeter measurements are 1.272x1.2x1.2x1.18cm (squarish), and the GaAs sample perimeter measurements are 1.6x2.484x3.50cm (trianglish). The first step was to get the sample cleaned and dehydrated. Then the photoresist S1818 was applied and after using the spinner, the sample was baked at 115°C for 60sec. The next step was aligning the sample with the photomask using the Karl Suss Mask Aligner, then exposed the sample to UV light for a period of 3.7sec, and finally developed the sample using developer MF319 for 50sec and a further 6sec in deionised (DI) water.

The next step is the wet etching, which is obtained by submerging the sample into a chemical solution (mixture of 1:1:4:16 of citric acid ($C_6H_8O_7$), phosphoric acid (H_3PO_4), hydrogen peroxide (H_2O_2) & distilled water (H_2O)) for a period of 4 minutes to obtain an etching of 2,000nm (2µm). The final step is removing the photoresist by submerging the sample into solvent 1165 inside a 65°C water bath for 10 minutes and a further 5 minutes in a clean and cold solvent 1165. This process is performed until the etching has been achieved, as T2SL structure is the same in all samples.
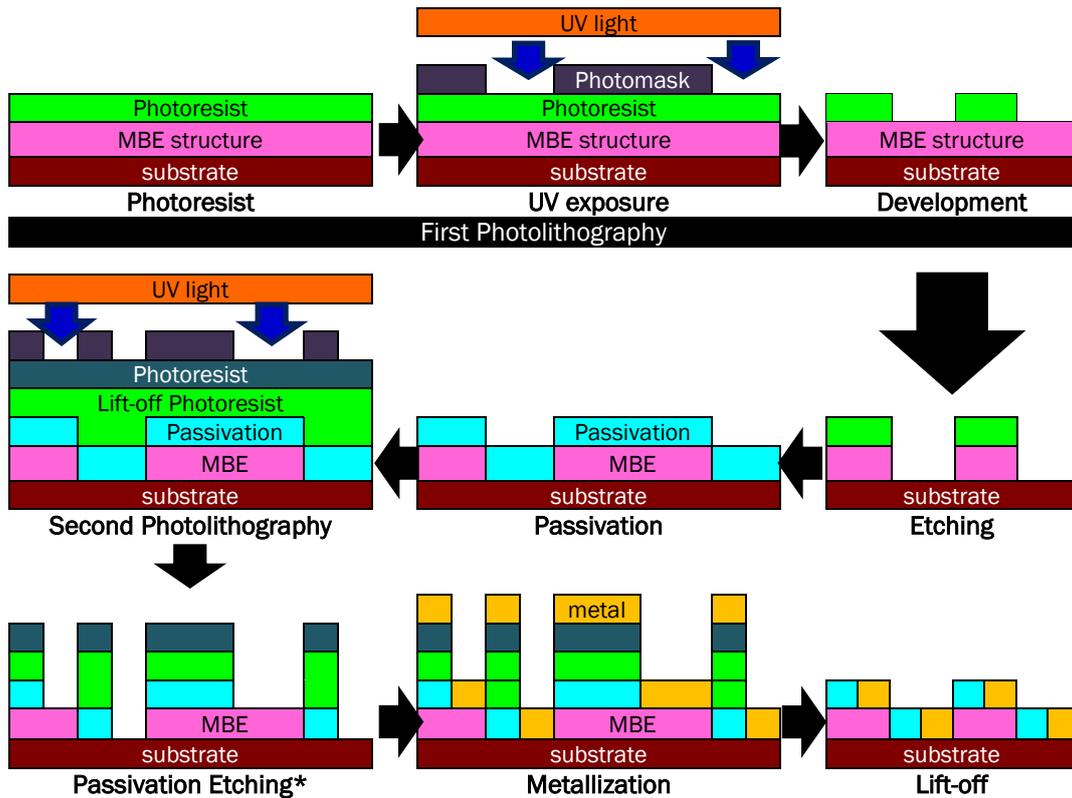
Figure 4.2: Step-by-step Device Fabrication Schematic

Part 2 is the passivation, which is used to reduce the surface leakage of the mesas. The passivation was carried out using a plasma enhanced chemical vapour deposition (PECVD). The passivation was designed as a low frequency (LF) SiO_2 (silicon dioxide) with a thickness of 200nm. A test sample was placed together with the designed sample, to verify the thickness. The final step is placing the test sample under the Horba Jobin Yvon MM16 Control Unit microscope to measure the thickness of the passivation, which in this case was 217nm. The passivation covered the entire mesa (top and laterally).

Part 3 is creating the ohmic contacts by using photolithography, which is second photolithography. The first step is to get the sample cleaned and dehydrated. Then the lift-off resist LOR10B was applied and after using the spinner, the sample was baked at 197°C for 10min. Then the photoresist S1818 was applied and after using the spinner, the sample was baked at 115°C for 60sec.

The next step was aligning the sample with the photomask using the Karl Suss Mask Aligner, then expose the sample to UV light for a period of 3.7sec, and finally develop the sample with developer MF319 for 50sec and a further 6sec in DI water. The final step is the passivation etching, which is obtained by submerging the sample into a chemical solution (1:1:4:16), same as before.

Part 4 is the metal deposition, which is carried out using a scientific vacuum system Allen-Bradley sputtering machine (SVS6000) by sputtering 20nm Ti (titanium), 50nm Pt (platinum) and 400nm Au (gold). The final step is the lift-off, which is achieved by submerging the sample into solvent 1165 inside a 65°C water bath for 30 minutes and a further 5 minutes in a clean and cold solvent 1165. This process is performed until a complete lift-off has been achieved in all the samples.

The result of the entire process is depicted in Figure 4.3.
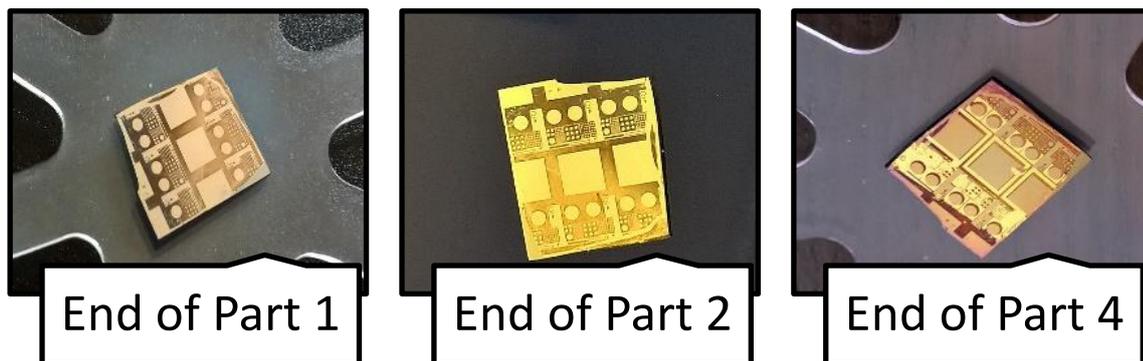
Figure 4.3: Device Fabrication Results

4.3. Results

4.3.1. Material Characterization.

The material characterisation measurements were carried out in order to assess the quality of the structure before fabrication. All the measurements were carried out in three different EEE laboratories based at UCL.

4.3.1.1. X-Ray Diffraction

The x-ray diffraction (XRD) results were obtained using a Bede D1 system machine, located at the MBE laboratory based at UCL EEE building.

The Bede machine creates a graph by using the diffracting pattern produced by each component starting from the top contact layer and ending with the substrate. Therefore, the graph depicts the top layer components on the left and the substrate on the right. The graphs depict the structural quality of the material constituting the sample by obtaining the ω-2θ value.

In order to obtain the best results, the Bede machine needs a starting point and this is given by the material of each sample substrate. In these cases, the substrates are GaAs with an ω (omega) of 33.0250° and a θ (theta) of 66.0501°, and Si with an ω of 34.5635° and a θ of 69.138°.

The OriginLab software enables the merging of various graphs from different samples. The graphs are centred at the zero peak (SL$_{0th}$), which depicts the intensity of the active region and the comparable measurement is full-width at half maximum (FWHM) which compares the microstrain within the sample. The graphs obtained were one per samples and they are depicted in Figure 4.4.

The resulting graphs depict their superlattice structures by the curve of the graph and the fringes created in between the peaks, which are created by the overlapping of the quantum wells. The curve goes uphill until it reaches its maximum height at zero peak and then goes downhill ending with the peak of the substrate.
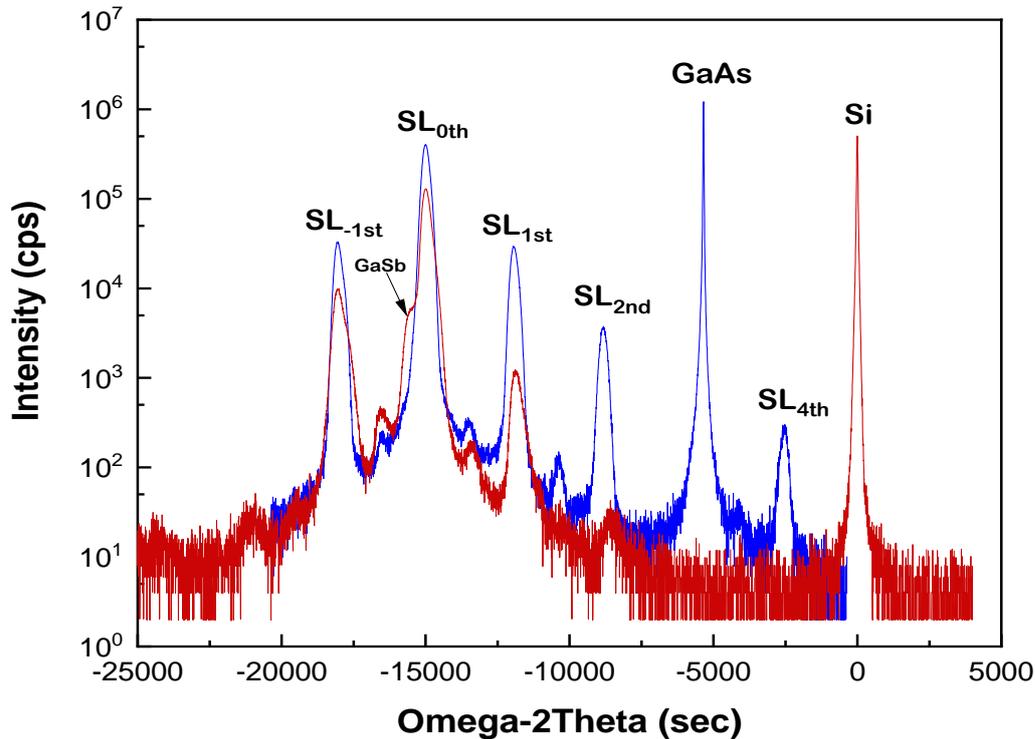
Figure 4.4: XRD of T2SL for a) GaAs and b) Si substrate

Figure 4.4 (blue) depicts the GaAs sample and its diffracting pattern. The graph depicts clear and defined peaks of up to fourth order depicting a well-defined superlattice structure, as they are grown in the same crystal structure. However, there is a minor threading dislocation due to the direct growth of GaSb over the GaAs substrate, which are depicted between the substrate and the SL_{2nd} peak. The full width half medium (FWHM) for GaAs is 300.2arcs.

Figure 4.4 (red) depicts the Si sample and its diffracting pattern. The graph depicts clear and defined peaks up to second order. After this, there is some scattering due to the crystal structure mismatch which occurs between SL_{1st} peak and the substrate. Additionally, the zero peak overlaps with the GaSb buffer which indicates a nearly lattice matched superlattice layers. There is a large threading dislocation due to the direct growth of AlSb over the Si substrate, which are depicted between the substrate and the SL_{2nd} peak and propagates into the device active region as the SL_{2nd} peak is almost unnoticeable. The FWHM for Si is 331.9arcs, however, this takes into consideration the contributions of GaSb buffer.

4.3.1.2. Atomic Force Microscope

The atomic force microscope (AFM) results were obtained using Bruker Dimension icon machine with ScanAsyst software, located at the Nanotechnology Laboratory based at UCL EEE building, and the images were obtained using the NanoScope software.

The Bruker machine creates an image of the morphology of the top layer. However, the NanoScope software helps analyse the information obtained and allows the information to be represented as a 2D image.

The 2D image allows to have a visual comparison of the structure and cluster. The comparison is between the root mean square (RMS) or roughness value and the thickness of the material of the top layer. Then the value is compared to the material's monolayer (ML) as a reference point. These results are depicted in Figure 4.5.

Figure 4.5: AFM of T2SL at 5x5μm² for a) GaAs and b) Si subtrate

Figure 4.5a depicts that the GaAs sample has very smooth surface where the atomic terraces are clearly defined, which demonstrates a good quality structure. The atoms kinetic energy is large enough to overcome the binding energy at the island coast which leads to a roughness transition. The top contact layer is made of 50nm GaSb, where GaSb has a ML of 0.3047nm. The RMS at 5x5μm² is 0.5nm for, which is less than 1.8% of the top contact layer or around 2ML. The height scale is 0.9 to 5.5nm.

Figure 4.5b depicts that the Si sample has atomic clusters which is the reason of the higher value of the RMS at 5x5μm^2, as slightly increasing the size reveals the real structures of the top layer. The top contact layer is made of 50nm GaSb, where GaSb has a ML of 0.3047nm. The RMS at 5x5μm^2 is 12nm for, which is around 24% or around 40ML. The height scale is -43.5 to 44.6nm.

4.3.1.3.　　Photoluminescence

The photoluminescence (PL) results were obtained from the experimental arrangement and then using the BenWin software which gathers information from a custom setting for testing mid-infrared array, located at the laser laboratory based at UCL EEE building.

The BenWin software creates one graph per sample as a function of either the temperature or the incident laser power. After gathering the information of multiple graphs, the OriginLab software allows to merge the graphs. The graphs obtained for temperature and power dependent are depicted in Figure 4.6.
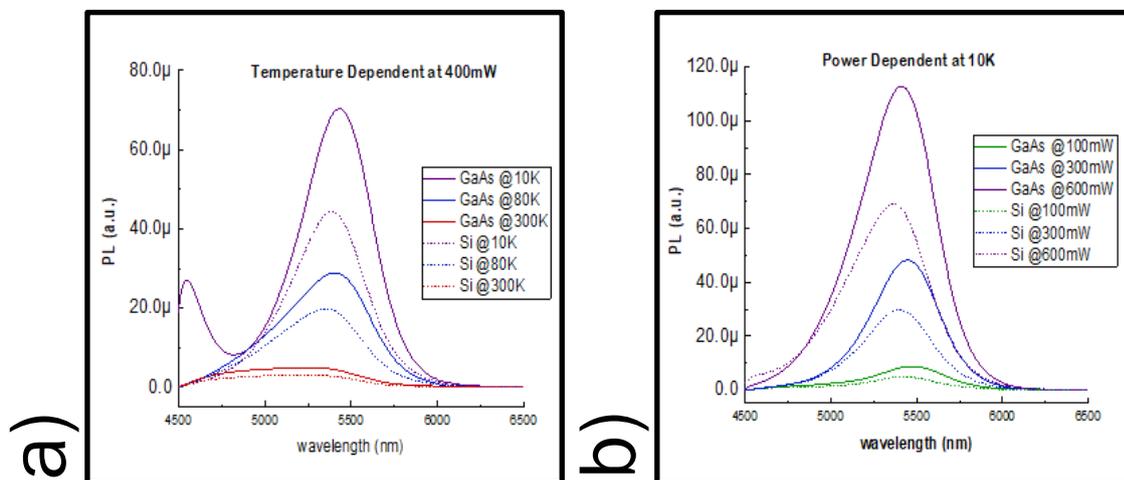
Figure 4.6: PL of T2SL for a) temperature and b) power dependent

Figure 4.6a depicts the power dependence which was carried out at 10K and helped define the power range. The measurements were carried out from 100mW to 600mW. The highest peak for both substrates is at 600mW, where the peak of GaAs at 546nm is 112.86μau (arbitrary unit), while the Si peak at 5365nm is 69.08μau.

Figure 4.6b depicts the temperature dependence which was carried out at 400mW and helped define the temperature range. The measurements were carried out from 10K to 300K. The highest peak for both substrates is at 10K, where the peak of GaAs at 5435nm is 70.33µau, while the Si peak at 5380nm is 44.38µau.

4.3.2. Electrical Characterization.

The electrical characterisation consists of the measurements of the dark current against bias voltage and against temperature. The results were obtained by Shanghai Tech University, where they tested all samples associated with this project.

4.3.2.1.   Bias-dependent Dark Current Density

The dark current (J_{dark}) results were collected and analysed by a Keysight semiconductor parameter analyser, located at Shanghai Tech University.

The parameter analyser measured the temperature-dependent I-V characteristics. After gathering the information of multiple graphs, the OriginLab software allows merging of the graphs. The graphs obtained for dark current vs bias voltage are depicted in Figure 4.7.

Figure 4.7a depicts the dark current vs bias voltage of the GaAs substrate. The temperatures were taken at 77K, 130K, 190K and 300K over bias ranging from 0,5V to -1.0V. The largest value measured at 300K and -1.0V is $8x10^1A/cm^2$; and the lowest value measured at 77K and -1.0V is $3x10^0A/cm^2$. The spread of the dark current between 77K and 300K is less than two orders of magnitude.

Figure 4.7b depicts the dark current vs bias voltage of the Si substrate. The temperatures were taken at 70K, 130K, 190K and 300K over bias ranging from -1.0V to 0.5V. The largest value measured at 300K and -1.0V is $1 x10^2A/cm^2$; and the lowest value measured at 70K and -1.0V is $4x10^1A/cm^2$. The spread of dark current between 70K and 300K is less than one order of magnitude.
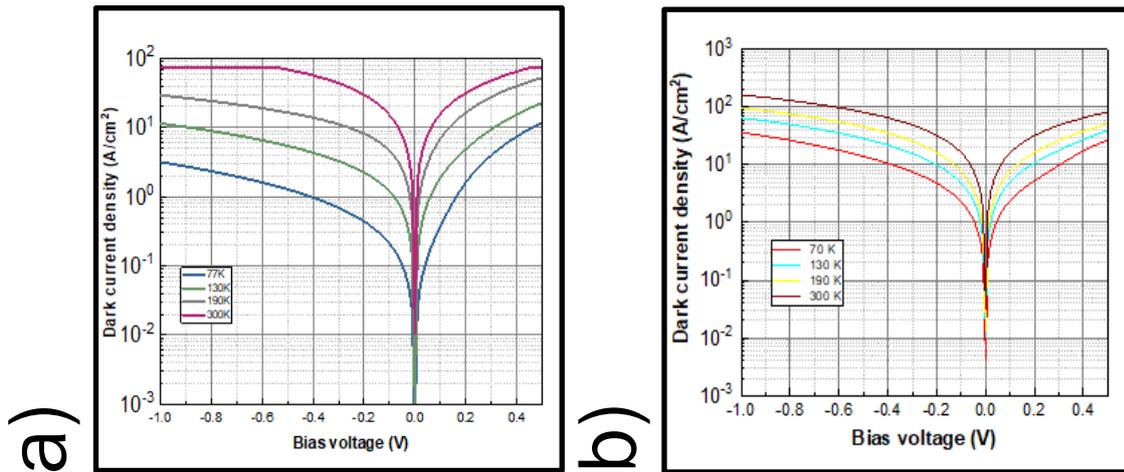
Figure 4.7: Dark current vs Bias for a) GaAs and b) Si subtrate

The dark current behaviour under bias depicts that the dark current of the GaAs structure is 6% lower than the Si structure within the temperature ranging between 70K and 130K. These results demonstrate that the GaAs spread is 2 orders of magnitude, while the Si spread is less than 1 order of magnitude.

4.3.2.2.   Temperature-dependent Dark Current Density

The dark current (J_{dark}) results were collected and analysed by a Keysight semiconductor parameter analyser which was configured to measure the temperature dependent dark current at a fixed reverse bias of 0.1V. This machine was located at Shanghai Tech University.

The characterisation of the activation energy (E_a) is the absolute value of the slope of this line [48], which is the minimum energy level required to create electron-hole pairs. The crossover temperature is where the diffusion and the generation-recombination currents are equal [22]. The temperature-dependent Arrhenius plots for dark current density are depicted in Figure 4.8.

Figure 4.8a depicts the dark current vs 1/temperature of the GaAs substrate. The measurements were taken at -0.1V with the temperature ranging from 77K to 300K. The activation energy at high temperatures is 53.1meV and at low temperatures is 28.1meV, with E_g of 230meV.
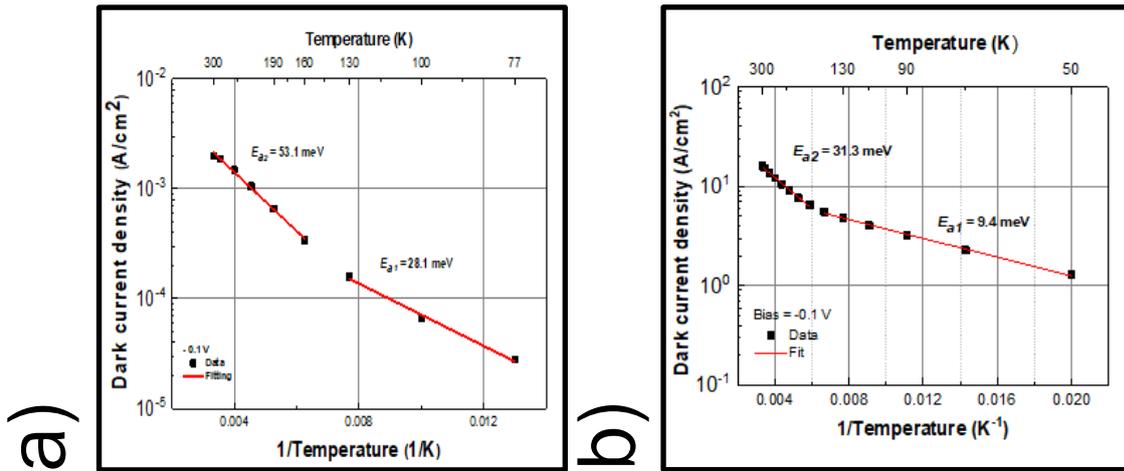
Figure 4.8: Arrheniou plot Dark current vs 1/Temperature for a) GaAs and b) Si substrate

Figure 4.8b depicts the dark current vs 1/temperature of the Si substrate. The measurements were taken at -0.1V with the temperature ranging from 77K to 300K. The activation energy at high temperatures is 31.3meV and low temperatures is 9.4meV.

In both substrates, the crossover temperature is 130K. The dark current values at high temperature demonstrates the absence of generation-recombination, as the activation energy is very small suggesting improvements in the doping quality at the contact level is required.

At low temperature, the very small activation energy demonstrates a predominate surface leakage.

4.3.3. Optical Characterization.

The optical characterisation consists of the measurements of quantum efficiency, absolute responsivity and specific detectivity. The results were obtained by Shanghai Tech University, where they tested all samples associated with this project.

4.3.3.1. Responsivity

The responsivity (R) results were collected and analysed using an FTIR (Fourier Transform Infrared) ThermoFisher Nicolet IS50, which gathers information from a custom setting consisting of a variable temperature cryostat and an IR light source, located at Shanghai Tech University.

The software creates one graph per unit change of temperature. After gathering the information of multiple graphs, the OriginLab software allows to merge the graphs. The graphs obtained for responsivity are depicted in Figure 4.9.
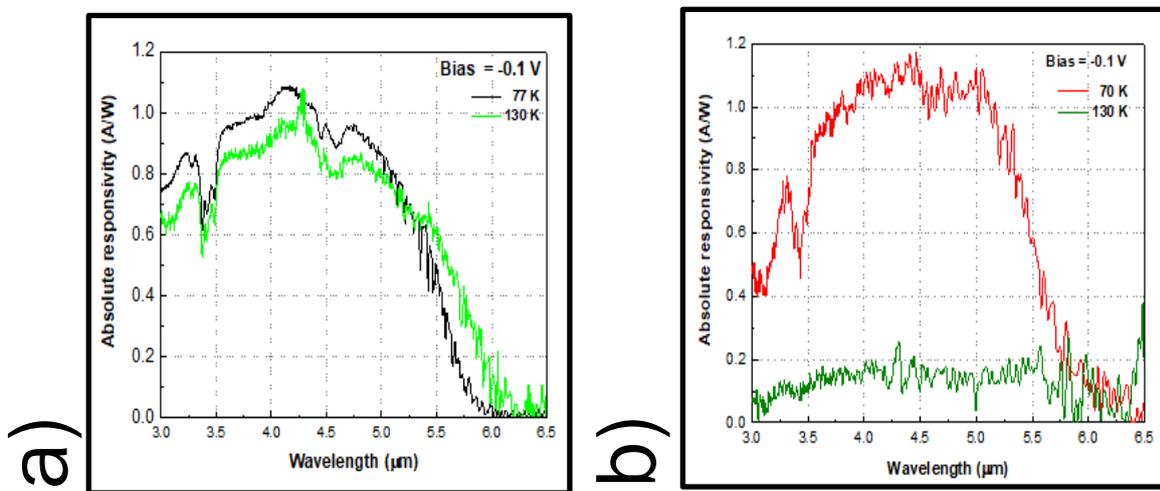
Figure 4.9: Responsivity at 130K for a) GaAs and b) Si substrate

Figure 4.9a depicts the responsivity of photodiode grown on the GaAs substrate. The temperatures were taken at 77K and 130K under bias of -0.1V. The largest value measured at 77K and 4.25µm is 1.1A/W; and the lowest value measured at 130K and 4.25µm is 0.98A/W. The absorption edge is around 5.5 µm and the difference between both temperatures is around 0.12A/W.

Figure 4.9b depicts the responsivity of photodiode grown on the Si substrate. The temperatures were taken at 70K and 130K under bias of -0.1V. The largest value measured at 70K and 4.25µm is 1.1A/W; and the lowest value measured at 130K and 4.25µm is 0.2A/W. The absorption edge is around 5.5 µm and the difference between both temperatures is around 0.9A/W.

4.3.3.2.   External Quantum Efficiency

The external quantum efficiency (EQE) results were obtained using equation E3.5. The software creates one graph per unit change of temperature. After gathering the information of multiple graphs, the OriginLab software allows merging of the graphs. The graphs obtained for responsivity are depicted in Figure 4.10.
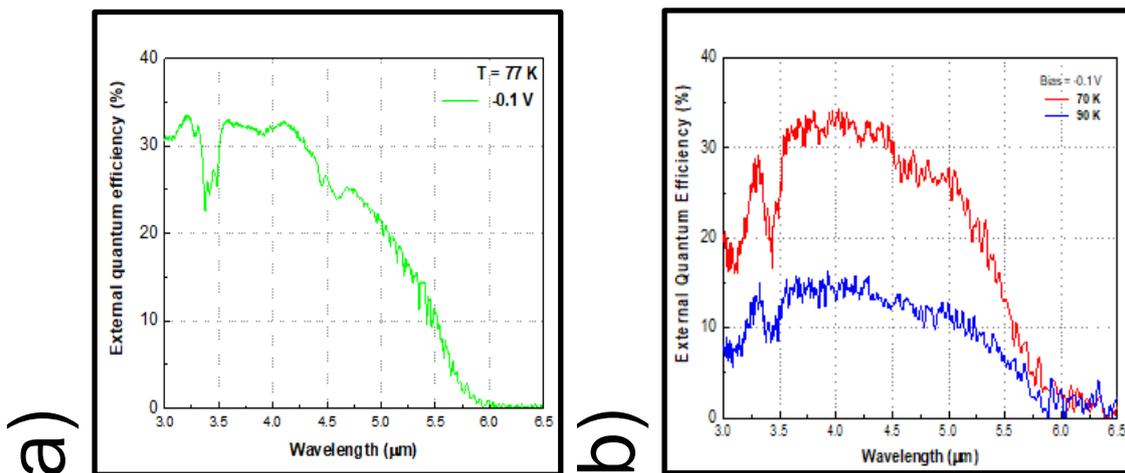
Figure 4.10: External Quantum Efficiency at -0.1V for a) GaAs and b) Si substrate

Figure 4.10a depicts the quantum efficiency of photodiode grown on the GaAs substrate. The temperatures were taken at 77K under bias of -0.1V. The largest value measured at 4.25µm is 33.5%. The absorption edge is around 5.5µm.

Figure 4.10b depicts the quantum efficiency of photodiode grown on the Si substrate. The temperatures were taken at 70K under bias of -0.1V. The largest value measured at 4.25µm is 30%. The absorption edge is around 5.5µm. The EQE reduces with temperature and at 77K the EQE is around 25%. The absorption edge is around 5.5µm.

4.3.3.3.　　　Specific Detectivity

The specific detectivity (D*) results were obtained using equation E3.6. The software creates one graph per unit change of temperature. After gathering the information of multiple graphs, the OriginLab software allows to merge the graphs. The graphs obtained for responsivity are depicted in Figure 4.11.
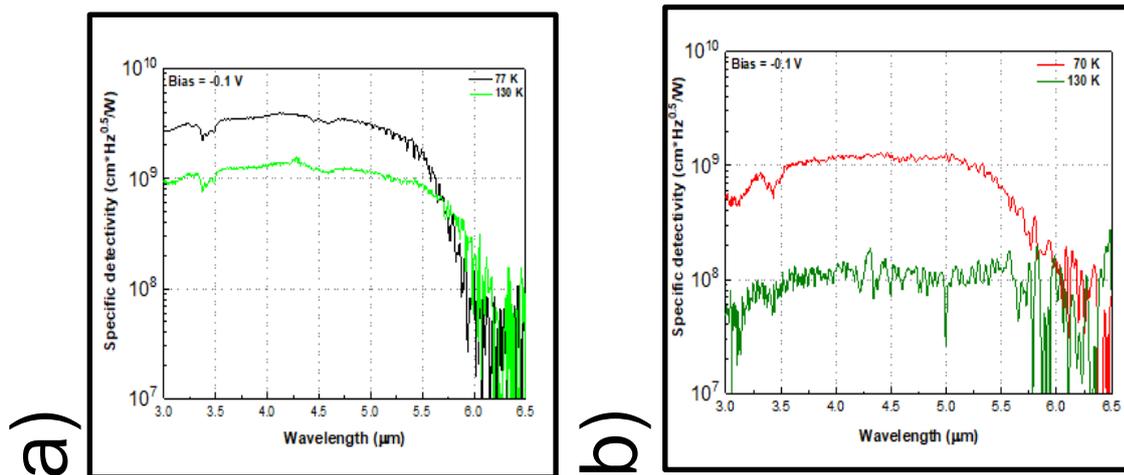
Figure 4.11: Specific Detectivity for a) GaAs and b) Si substrate

Figure 4.11a depicts the specific detectivity of photodiode grown on the GaAs substrate. The temperatures were taken at 77K and 130K under bias of -0.1V. The largest value measured at 77K and 4µm is 4×10^9 cmHz$^{\frac{1}{2}}$/W; and the lowest value measured at 130K and 4µm is 1×10^9 cmHz$^{\frac{1}{2}}$/W. The absorption edge is around 5.5 µm and there is less than half an order of magnitude.

Figure 4.11b depicts the specific detectivity of photodiode grown on the Si substrate. The temperatures were taken at 70K and 130K under bias of -0.1V. The largest value measured at 70K and 4µm is 1×10^9 cmHz$^{\frac{1}{2}}$/W; and the lowest value measured at 130K and 4µm is 1×10^8 cmHz$^{\frac{1}{2}}$/W. The absorption edge is around 5.5 µm and there is one order of magnitude.

4.4. Discussion

This chapter compared the performance between structures grown on GaAs substrate and Si substrate. Overall, it can be concluded that the performance of the Si architecture is consistent with the performance of the GaAs architecture. The construction of the Si substrate is of good quality, good performance and good migration of the structure grown on GaAs substrate.

The x-ray diffraction of both structures has achieved similar dislocation density at zero peak. There is also some scattering from the Si structure caused by the buffer which is between the substrate and the nip structure where the full-width at half maximum (FWHM) of the Si architecture is 10% bigger than the GaAs architecture due to the contribution of the GaSb buffer.

The photoluminescence of the Si architecture is 40% smaller than the intensity of the GaAs architecture. The optimal temperature is 10K and optimal power is 600mW. The Si peak shifted 1% to the left with respect to the GaAs peak.

The atomic force microscope depicts good crystal qualities for the GaAs architecture, however, the Si architecture developed atomic clusters. The RMS for the Si architecture is 24% bigger than the GaAs architecture.

The dark current behaviour under bias depicts that the dark current of the GaAs architecture is 6% lower than the Si architecture within the temperature ranging between 70K and 130K.

The temperature dependent dark current demonstrates the absence of generation-recombination due to the low values at high temperatures.

The optical characterisation measured the absorption edge of both structures as 5.5μm. The quantum efficiency for the Si architecture is 23% lower than the GaAs architecture. The responsivity for the Si architecture is 80% lower than the intensity of the GaAs architecture. The specific detectivity for the Si architecture is 25% lower than the GaAs architecture and their spread is around 1 order of magnitude.

The material characterisation demonstrates that the Si architecture has 60% of the intensity compared to the GaAs architecture. The absorption edge of the GaAs structure is around 5.43µau while for the Si structure is around 5.38µau.

The electrical characterisation demonstrates that GaAs architecture has 6% reduction of the dark current under bias when compared to the Si architecture. The Si architecture has 41% reduction when compared to the dark current under temperature.

These results demonstrate that the direct growth of a T2SL structure over the Si substrate migration has achieved similar structural and optical properties with regards to the GaAs substrate, which is our reference architecture.

These results demonstrate that achieving optimisation of the GaAs substrate before migrating to the Si substrate will result in better growth techniques and hence better architectures.

Therefore, the next Chapter will be comparing three basic structures grown over GaAs substrate before moving to more complex architectures grown directly on Si substrate.

Chapter 5: Comparison of T2SL detectors of different architectures on GaAs substrate

5.1. Introduction

This chapter compares the performance of the nip, pπn and pπBn architectures grown on GaAs substrates.

The aim was to demonstrate high quality type II superlattice (T2SL) detectors grown on GaAs substrate. With this in mind, the superlattice layers of the structures have the same period of 10ML InAs/ 10ML GaSb with opposite doping types to match the designed configuration. The structures were designed by Dr Jiang Wu.

The main difference in the structures is the use of a unipolar barrier. The structure's layers remain almost the same with just an addition of the barrier within the intrinsic layer in one of the structures creating the pπBn structure. This allows isolation of the performance of the barrier and analyses its overall effect in the structure.

The other differences are the size of the buffer and the material of the top doped contact layer of the architecture between the nip and pπn architectures. This allows comparing of the performance of the different architectures and its contact resistance on the complete structure.

After the growth, the material characterisation measurements were carried out by myself with minor supervision at UCL premises. However, the fabrication process, the electrical and the optical testing were carried out by Shanghai Tech University, which is outside the UCL premises, due to temporary closure of the cleanroom laboratory at LCN.

5.2. Methodology

5.2.1. MBE growth details.

The structures were grown in Veeco GEN930 solid-source MBE by the MBE group based at UCL. These structures are depicted in Figure 5.1 [45].

The T2SL photodiodes consist of different superlattice periods but always ending with a 1ML InSb. The InSb layer is grown for strain balance due to the fact that the lattice constant of InAs is 0.75% smaller than that of GaSb.
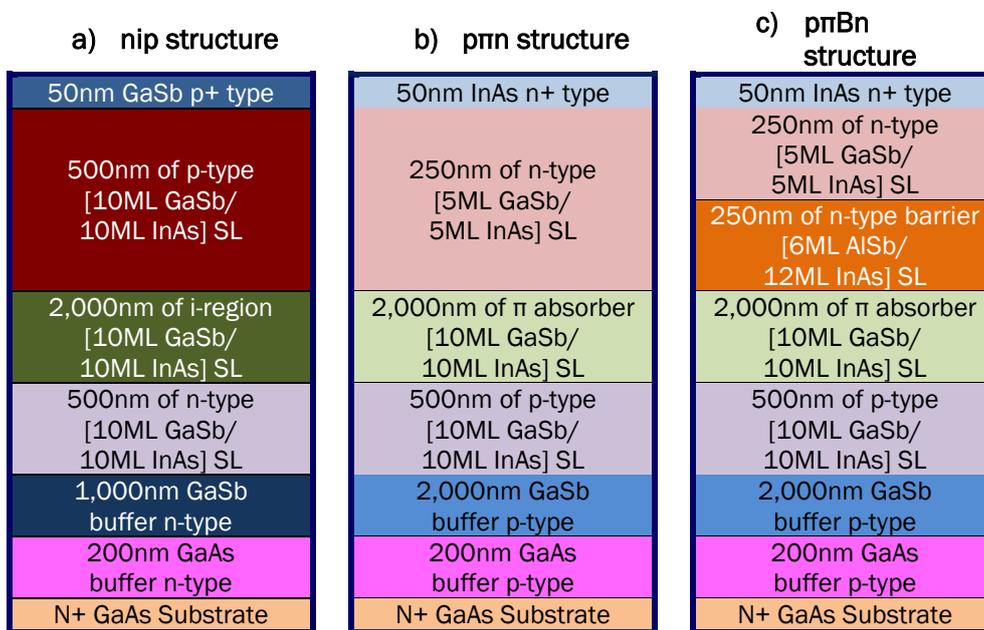
Figure 5.1: Epitaxial layer structures for a) nip, b) pπn and c) pπBn architecture

In the ***nip architecture,*** which consists of an n-doped layer (n), then an intrinsic layer (i), and finally a p-doped layer (p). All epi-layers were directly grown on GaAs (001) substrate by MBE. After the deoxidation, the substrate was cooled down to 590°C in order to grow a 200nm GaAs smooth layer. Then the substrate was cooled further to about 500°C in order to grow a 1µm GaSb buffer layer.

After the buffer, the substrate was cooled down to 400°C in order to grow the T2SL photodiode. The architecture of the nip structure consists of an n-doped bottom contact of 500nm (82 periods of 10ML GaSb/10ML InAs/1ML In), an i-region of 2µm (329 periods of 10ML GaSb/10ML InAs/1ML In), and an p-doped top contact of 500nm (82

periods, 10 ML GaSb/10 ML InAs/1ML In). After the structure, a heavily p+ doped 50nm GaSb cap layer is grown for good ohmic contact property.

In the ***pπn architecture***, which consists of a p-doped layer (p), then a near-intrinsic p-doped layer (π) and finally an n-doped layer (n). All epi-layers were directly grown on GaAs (001) substrate by MBE. After the deoxidation, the substrate was cooled down to 590°C in order to grow a 200nm GaAS smooth layer. Then the substrate was cooled further to about 500°C in order to grow a 2µm GaSb buffer layer.

After the buffer, the substrate was cooled down to 400°C in order to grow the T2SL photodiode. The architecture of the pπn structure (as it is read from bottom to top) consists of a p-doped bottom contact of 500nm (82 periods of 10ML GaSb/10ML InAs/1ML In), a π absorber (as it is near-intrinsic p-doped) of 2µm (329 periods of 10ML GaSb/10ML InAs/1ML In), and an n-doped top contact of 250nm (82 periods, 5 ML GaSb/5ML InAs/1ML In). After the structure, a heavily n+ doped 50nm InAs cap layer is grown for good ohmic contact property.

In the ***pπBn architecture***, which consists of a p-doped layer (p), then a near-intrinsic p-doped layer (π), then an n-doped barrier (B) and finally an n-doped layer (n). All epi-layers were directly grown on GaAs (001) substrate by MBE. After the deoxidation, the substrate was cooled down to 590°C in order to grow a 200nm GaAS smooth layer. Then the substrate was cooled further to about 500°C in order to grown a 2µm GaSb buffer layer.

After the buffer, the substrate was cooled down to 400°C in order to grow the T2SL photodiode. The architecture of the pπBn structure consists of a p-doped bottom contact of 500nm (82 periods of 10ML GaSb/10ML InAs/1ML In), a p-doped absorber (π absorber) of 2µm (329 periods of 10ML GaSb/10ML InAs/1ML In), a n-doped barrier of 250nm (41 periods of 6ML AlSb/12ML 6 InAs/1ML In), and an n-doped top contact of 250nm (82 periods, 5 ML GaSb/5ML InAs/1ML In). After the structure, a heavily n+ doped 50nm InAs cap layer is grown for good ohmic contact property.

5.2.2. Device fabrication.

The device fabrication was carried out by Shanghai Tech University. The device fabrication is a standard procedure regardless of where it takes place. After this, the electrical and the optical characterisation were also carried out by Shanghai Tech University. The step-by-step fabrication process is depicted in Figure 5.2.
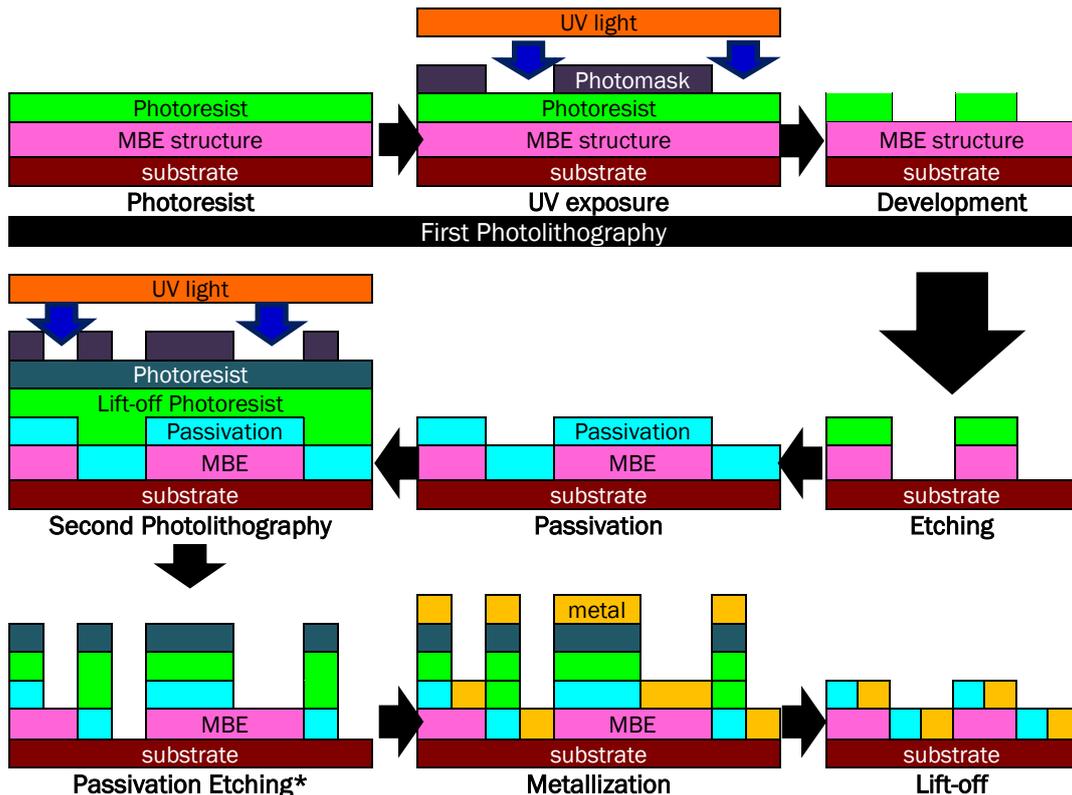
Figure 5.2: Step-by-step Device Fabrication Schematic

According to Shanghai Tech University, the wafer was processed into circular mesas of variable diameters [45] using the standard process of UV photolithography technique. The mesas were defined by wet chemical etching with a chemical solution (mixture of 1:1:4:16 of citric acid ($C_6H_8O_7$), phosphoric acid (H_3PO_4), hydrogen peroxide (H_2O_2) & distilled water (H_2O)).

The passivation applied was SU8 using a spinner and soft bake. Then metal was deposited by sputtering 50nm Ti, 50nm Pt and 300nm Au. Finally, the samples underwent a lift-off process to remove the excess of metal.

5.3. Results

5.3.1. Material Characterization.

The material characterisation measurements were carried out in order to assess the quality of the structure before fabrication. All the measurements were carried out in three different EEE laboratories based at UCL.

5.3.1.1.   X-Ray Diffraction

The x-ray diffraction (XRD) results were obtained using a Bede D1 system machine, located at the MBE laboratory based at UCL EEE building.

The Bede machine creates a graph by using the diffracting pattern produced by each component starting from the top contact layer and ending with the substrate. Therefore, the graph depicts the top layer components on the left and the substrate on the right. The graphs depict the structural quality of the material constituting the sample by obtaining the ω-2θ value.

In order to obtain the best results, the Bede machine needs a starting point and this is given by the material of each sample substrate. In this case, the substrate is GaAs with an ω (omega) of 33.0250° and a θ (theta) of 66.0501.

The OriginLab software enables the merging of various graphs from different samples. The graphs are centred at substrates as they are all GaAs samples. The graphs obtained were one per sample and they are depicted in Figure 5.3.

The resulting graphs depict their superlattice structure by the curve of the graph and the fringes created in between the peaks, which is created by the overlapping of the quantum wells. The curve goes uphill until it reaches its maximum height at zero peak and then goes downhill ending with the peak of the substrate.

The diffracting pattern of graphs depict clear and defined peaks up to fourth order depicting a well-defined superlattice structure, as they are grown in the same crystal structure. However, there is a minor threading dislocation due to the direct growth of

GaSb over the GaAs substrate, which is depicted between the substrate and SL_{2nd} represents. The threading dislocation is created by the direct growth of GaSb over the GaAs substrate. In case of the nip structure this layer is 1,000nm, while for the pπn and pπBn structures is 2,000nm.

The shift of the SL_{-1st} of the pπn and pπBn structures from nip structures is due to the fact that the nip structure comprises of 10ML GaSb/10ML InAs while the other two structures are 5ML GaSb/5ML InAs.

The division of the SL_{0th} peak is due to the fact that the nip structure has intrinsic material while the pπn and pπBn has a p-doped absorber. The only peak which is identical in all structure is SL_{1st} as it has the same construction in all the structures.
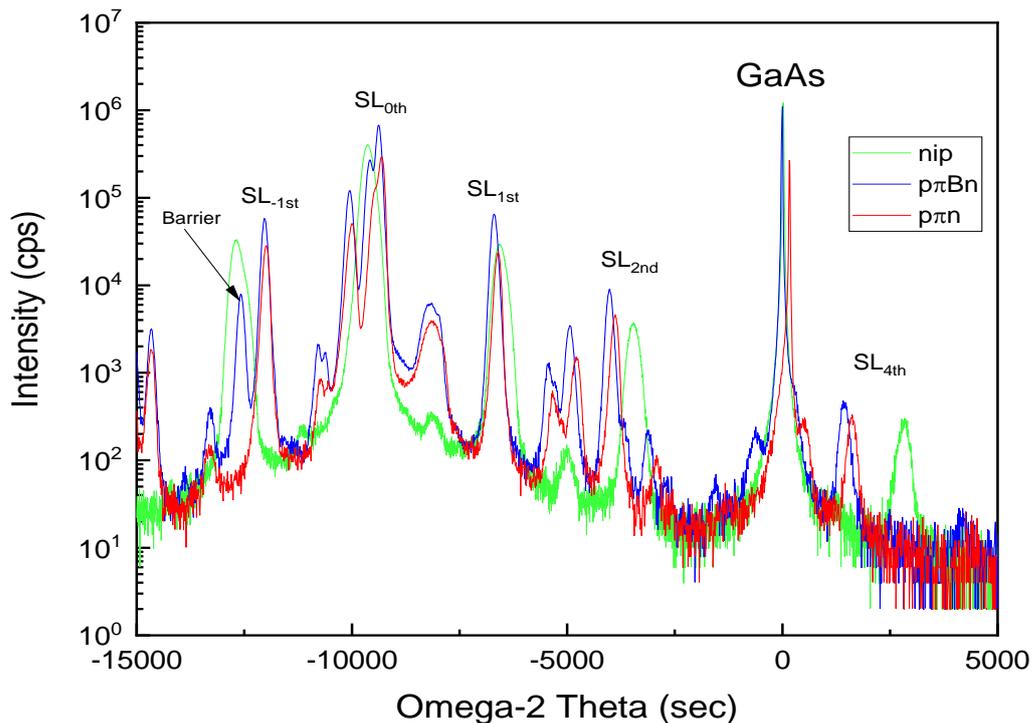
Figure 5.3: XRD of T2SL for a) nip, b) pπn and c) pπBn structures

Figure 5.3 (green) depicts the nip structure and the FWHM at zero peak is 300.2arcs. The diffracting pattern of the graph depicts clear and define peaks up to fourth order depicting a well-defined superlattice structure, as they are grown in the same crystal structure. However, there is a minor threading dislocation due to the direct growth of GaSb over the GaAs substrate.

Figure 5.3 (red) depicts the pπn structure and the FWHM at zero peak is 235arcsec. The diffracting pattern of the graph also depicts up to fourth order peaks these are not as well defined as the nip structure.

Figure 5.3 (blue) depicts the pπBn structure and the FWHM at zero peak is 223arcsec. The diffracting pattern of the graph also depicts up to fourth order peaks but these are not as well defined as the nip structure. However, these are the same as pπn structures with the only difference in the SL$_{-1st}$ order where the pπBn structure has an additional peak depicting the barrier.

5.3.1.2.   Atomic Force Microscope

The atomic force microscope (AFM) results were obtained using Bruker Dimension icon machine with ScanAsyst software, located at the Nanotechnology Laboratory based at UCL EEE building, and the images were obtained using the NanoScope software.

The Bruker machine creates an image of the morphology of the top layer. However, the NanoScope software helps analyse the information obtained and allows the information to be represented as a 2D image.

The 2D image allows to have a visual comparison of the structure and cluster. The comparison is between the root mean square (RMS) or roughness value and the thickness of the material of the top layer. Then the value is compared to the material's monolayer (ML) as a reference point. These results are depicted in Figure 5.4. The height scale in all graphs is 0 to 5nm.

Figure 5.4a depicts the nip structure, where its top contact layer is made of 50nm GaSb with a ML of 0.3047nm. The RMS at 5x5µm^2 is 0.5nm, which is less than 2% of the top contact layer or around 2ML.

Figure 5.4b depicts the pπn structures, where its top contact layer is made of 50nm InAs with a ML of 0.3029nm. The RMS at 5x5µm^2 is 0.9nm, which is less than 3ML.
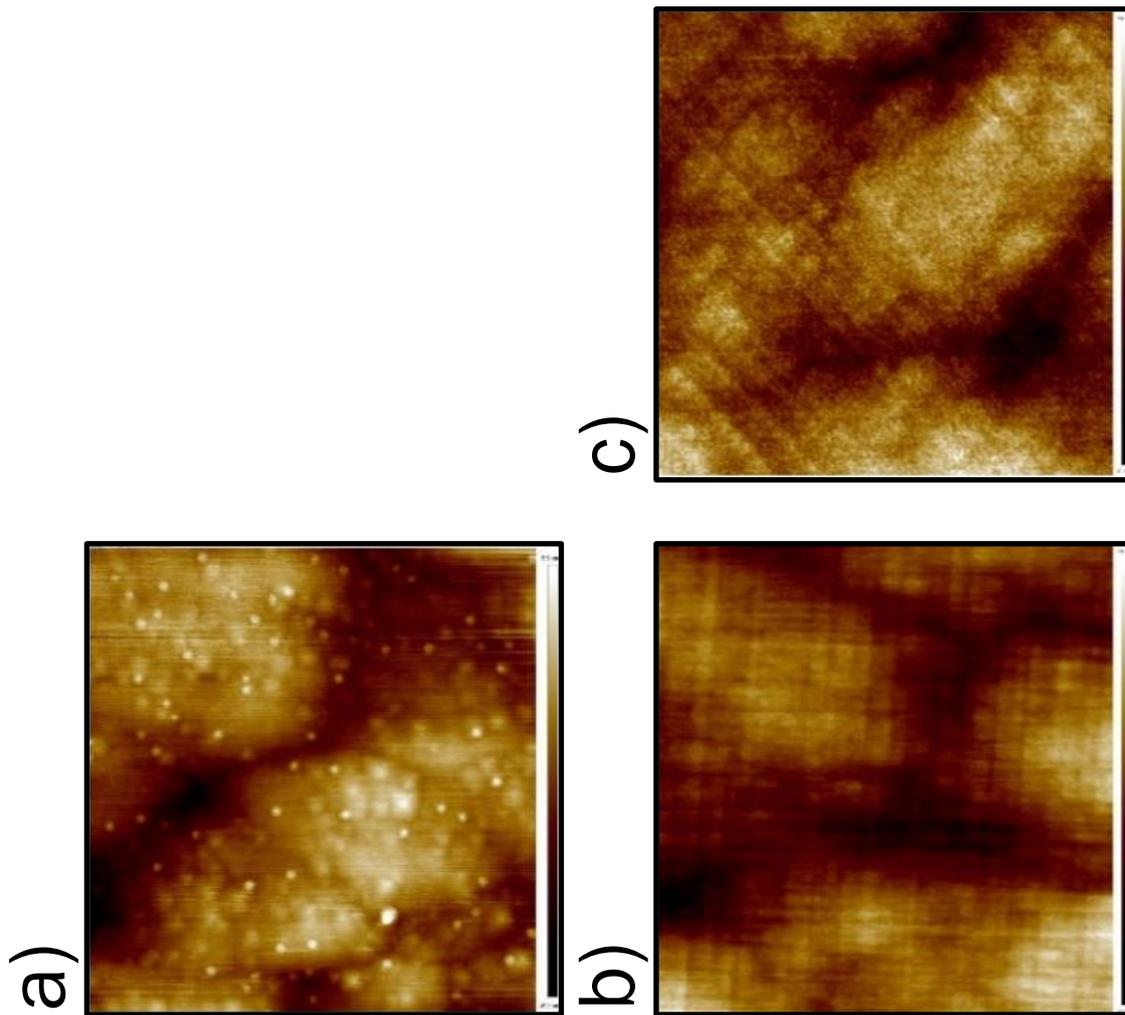
Figure 5.4: AFM of T2SL at 5x5μm² for a) nip, b) pπn and c) pπBn structures

Figure 5.4c depicts the pπBn structure, where its top contact layer is made of 50nm InAs with a ML of 0.3029nm. The RMS at 5x5μm² is 1.32nm, which is less than 5ML.

5.3.1.3.   Photoluminescence

The photoluminescence (PL) results were obtained from the experimental arrangement, located at the laser laboratory based at UCL EEE building.

In both cases, the samples were placed in cryostat cooling system. Then the temperature was reduced to 10K, as this has proved to be the optimal value from the results obtained in Chapter 4. Then the power measurement started at around 600mW, as this has proved to be the optimal value from the results obtained in Chapter 4.

The BenWin software was unable to detect any peaks at 600mW, therefore, the power range was increased. The new power range was from 10mW to 1,000mW and still no visible peaks were found. The same experiment was attempted in three different session and no results were derived.

5.3.2. Electrical Characterization.

The electrical characterisation consists of the measurements of the dark current against bias voltage and temperature. The results were obtained by Shanghai Tech University, where they tested all samples associated with this project. In order to do their testing, Shanghai University performed their own device fabrication using SU8 as their choice for passivation.

5.3.2.1.   Bias-dependent Dark Current Density

The dark current (J_{dark}) results were collected and analysed by a Keysight semiconductor parameter analyser, located at Shanghai Tech University.

The parameter analyser measured the temperature-dependent I-V characteristics. After gathering the information of multiple graphs, the OriginLab software allows to merge the graphs. The graphs obtained for dark current vs bias voltage are depicted in Figure 5.5.

Figure 5.5a depicts the dark current vs bias voltage of the nip and pπn structure. The temperatures were taken at 77K, 130K and 190K over bias ranging from 0.5V to -1.0V. The largest value of the nip structure measured at 190K and -0.6V is $2x10^1$A/cm^2; and the lowest value measured at 77K and -0.6V is $1.8x10^0$A/cm^2. The spread of the dark current between 77K and 190K is a bit over one order of magnitude. The largest value of pπn structure measured at 190K and -0.6V is $6x10^1$A/cm^2; and the lowest value measured at 77K and -0.6V is $8x10^1$A/cm^2. The spread of the dark current between 77K and 190K is less than half an order of magnitude.
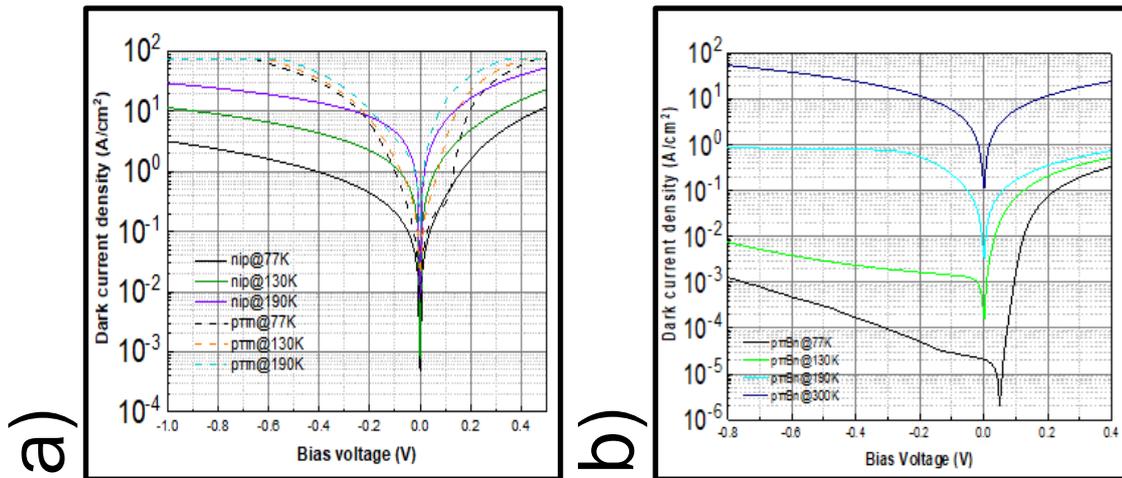
Figure 5.5: Dark current vs bias for a) nip & pπn and b) pπBn structures

Figure 5.5b depicts the dark current vs bias voltage of the pπBn structure. The temperatures were taken at 70K, 130K, 190K and 300K over bias range from -1.0V to 0.5V. The largest value measured at 190K and -1.0V is $9 \times 10^{-1} A/cm^2$; and the lowest value measured at 77K and -1.0V is $5 \times 10^{-3} A/cm^2$. The spread of dark current between 70K and 190K is less than three orders of magnitude, while the spread of dark current between 70K and 300K is almost four orders of magnitude.

5.3.2.2. Temperature-dependent Dark Current Density

The dark current (J_{dark}) results were collected and analysed by a Keysight semiconductor parameter analyser which was configured to measure the temperature dependent dark current at a fixed reverse bias of 0.1V. This machine was located at Shanghai Tech University.

The characterisation of the activation energy (E_a) is the absolute value of the slope of this line [48], which is the minimum energy level required to create electron-hole pairs. The temperature dependent Arrhenius plots of the dark current density are depicted in Figure 5.6. The crossover temperature is 130K.

Figure 5.6a depicts the dark current vs 1/temperature of the nip structure. The measurements were taken at -0.1V with the temperature ranging from 77K to 300K. The activation energy at high temperatures is 53.1meV and at low temperatures is

28.1meV, with E_g of 230meV. The dark current values at high temperature demonstrate the surface leakage dominant and at low temperature demonstrate the absence of the generation-recombination mechanism.
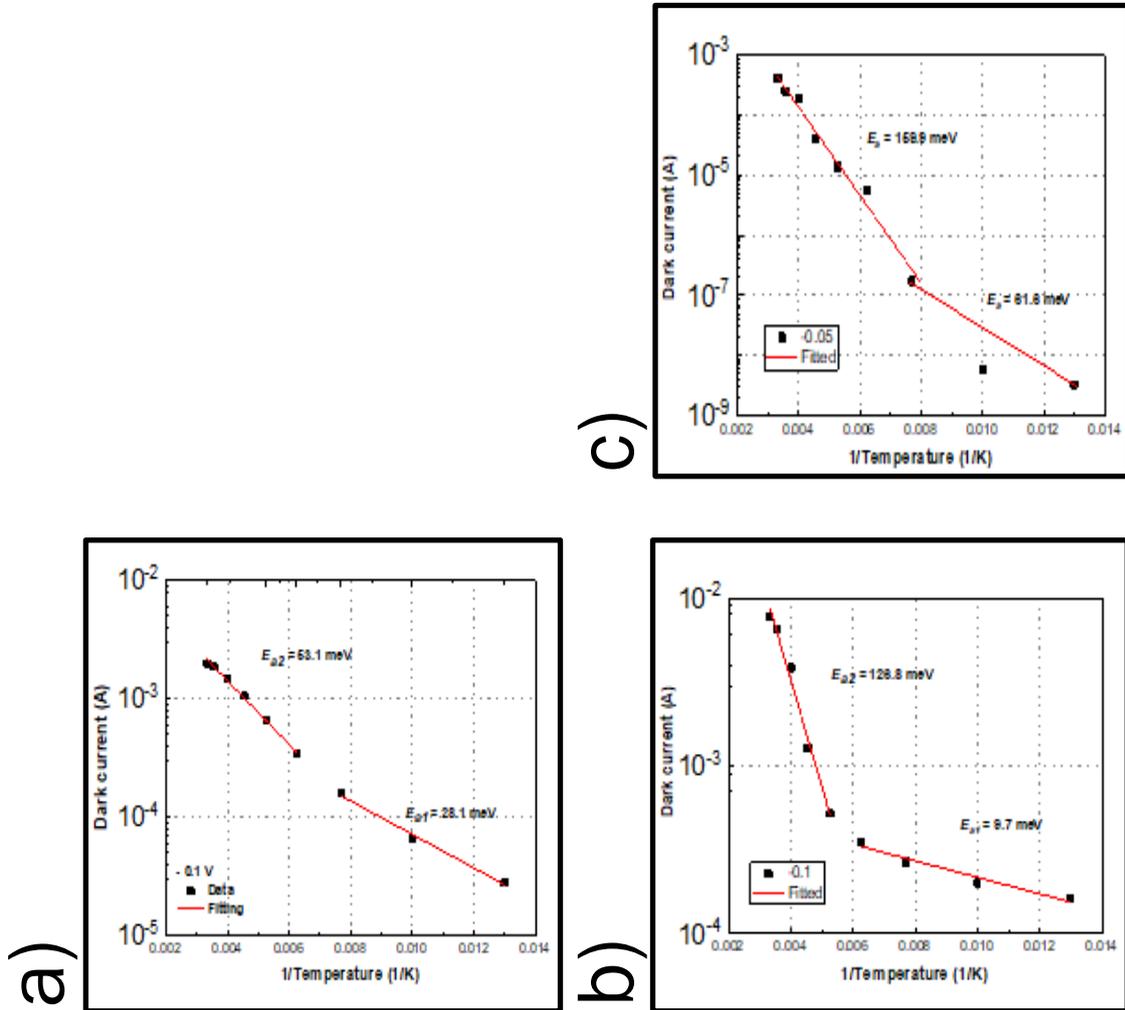
Figure 5.6: Arrheniou plot of Dark current vs 1/Temperature a) nip, b) pπn and c) pπBn structures

Figure 5.6b depicts the dark current vs 1/temperature of the pπn structure. The measurements were taken at -0.1V with the temperature ranging from 77K to 300K. The activation energy at high temperatures is 126.8meV and low temperatures is 9.7meV. The dark current values at high temperature demonstrates mainly contribution by diffusion, as the activation energy is closer to the energy gap. At low temperature demonstrate generation-recombination mechanism dominant, as the activation energy is very small.

Figure 5.6c depicts the dark current vs 1/temperature of the pπBn structure. The measurements were taken at -0.1V with the temperature ranging from 77K to 300K. The activation energy at high temperatures is 159.9meV and low temperatures is 61.6meV, with E_g of ~184meV. The dark current values at high temperature demonstrates mainly contribution by diffusion, as the activation energy is closer to the energy gap. At low temperature, the activation energy is around a third of the energy gap demonstrating a mechanism limited by the generation-recombination.

5.3.3. Optical Characterization.

The optical characterisation consists of the measurements of quantum efficiency, absolute responsivity and specific detectivity. The results were obtained by Shanghai Tech University, where they tested all samples associated with this project.

5.3.3.1.   Responsivity

The responsivity (R) results were collected and analysed using an FTIR (Fourier Transform Infrared) ThermoFisher Nicolet IS50, which gathers information from a custom setting consisting of a variable temperature cryostat and an IR light source, located at Shanghai Tech University.

The software creates one graph per unit change of temperature. After gathering the information of multiple graphs, the OriginLab software allows to merge the graphs. The graphs obtained for responsivity are depicted in Figure 5.7.

Figure 5.7a depicts the responsivity of the nip structure. The temperatures were taken at 77K, 130K and 190K under bias of 0V. The largest value measured at 77K and 4.25μm is 0.55A/W; and the lowest value measured at 190K under 4.25μm is 0.15A/W. The absorption edge is around 5.5 μm and the difference between both temperatures is around 0.4A/W.

Figure 5.7b depicts the responsivity of the pπn structure. The temperatures were taken at 77K, 130K and 190K under bias of 0V. The largest value measured at 77K and

6.0µm is 0.06A/W; and the lowest value measured at 190K and 6.0µm is 0.006A/W. The absorption edge is around 6.5 µm and the difference between both temperatures is around 0.014A/W.
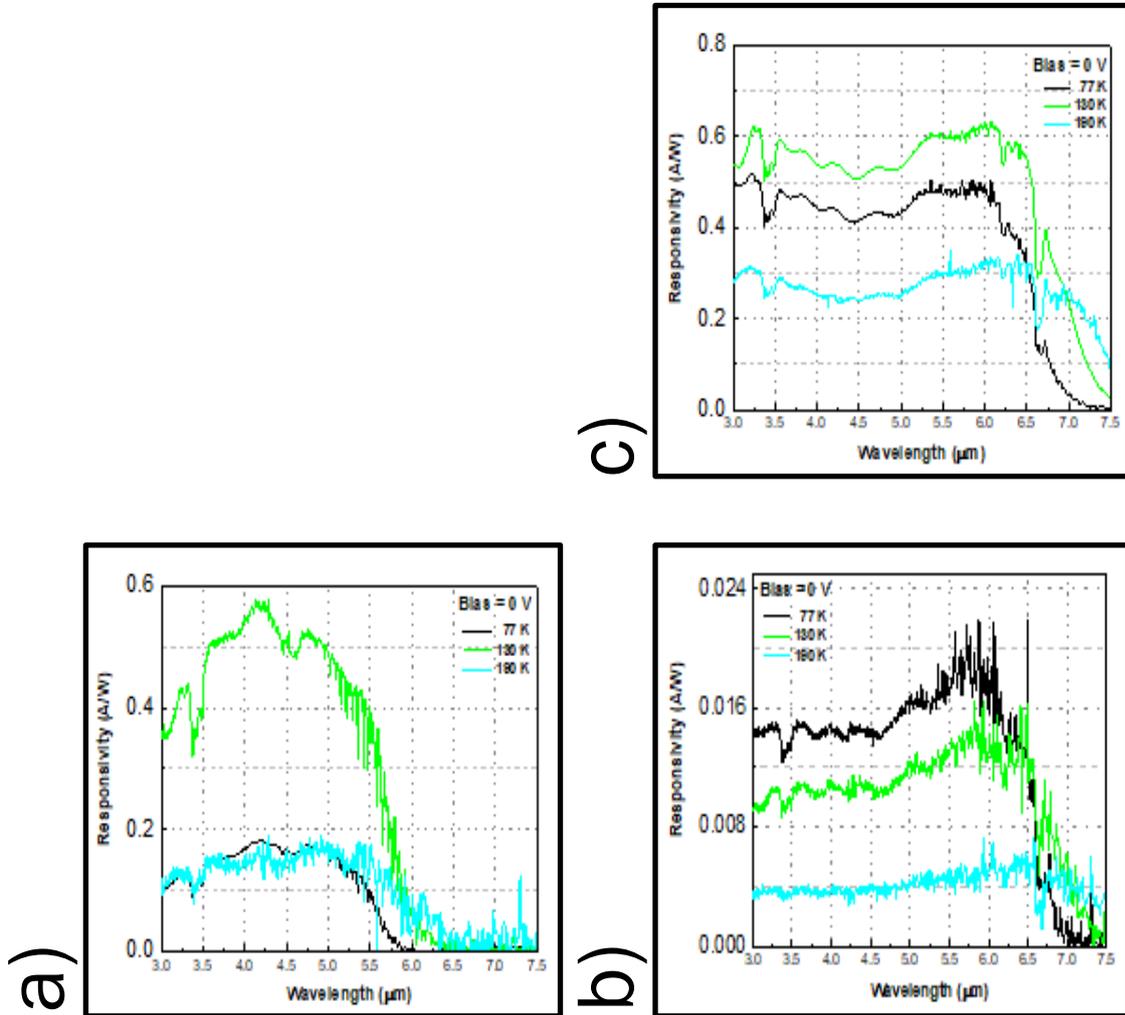
Figure 5.7: Responsivity for a) nip, b) pπn and c) pπBn structures

Figure 5.7c depicts the responsivity of the pπBn structure. The temperatures were taken at 77K, 130K and 190K under bias of 0V. The largest value measured at 77K and 6.0µm is 0.6A/W; and the lowest value measured at 190K and 6.0µm is 0.3A/W. The absorption edge is around 6.5 µm and the difference between both temperatures is around 0.3A/W.

The difference of 1 µm between the absorption layer of the nip structures and the other two structures is due to the top superlattice layer. The top superlattice layers are: for

nip the p-doped layer is 10ML GaSb/10ML InAs, and for pπn and pπBn the n-doped layer is 5ML GaSb/ 5ML InAs.

5.3.3.2. External Quantum Efficiency

The external quantum efficiency (EQE) results were obtained using equation E3.5. The software creates one graph per unit change of temperature. After gathering the information of multiple graphs, the OriginLab software allows to merge the graphs. The graphs obtained for responsivity are depicted in Figure 5.8.
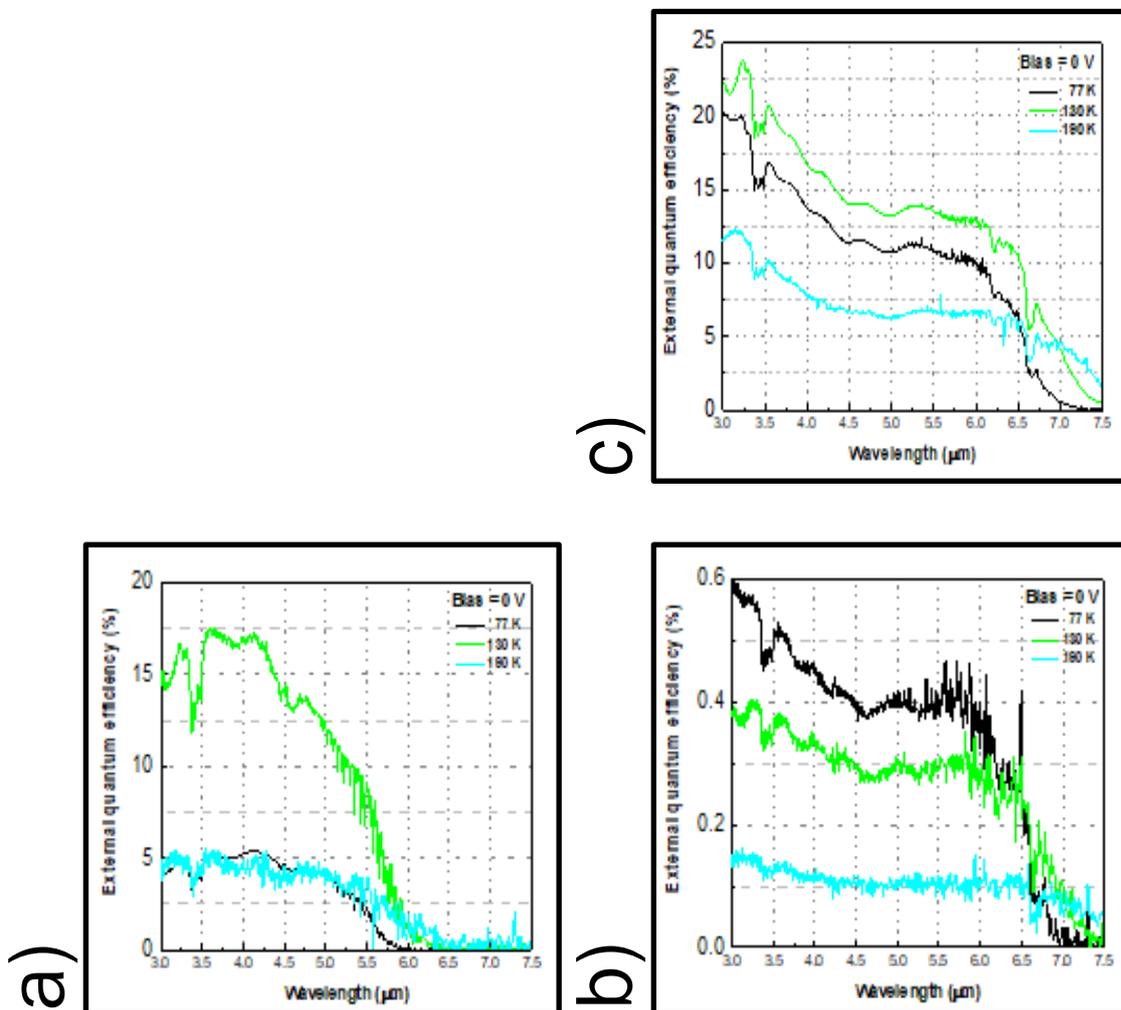
Figure 5.8: External Quantum Efficiency for a) nip, b) pπn and c) pπBn structures

Figure 5.8a depicts the quantum efficiency of the nip structures. The temperatures were taken at 77K, 130K and 190K under bias of 0V. The largest value is measured at 130K and 4.25μm is 17.5%. The absorption edge is around 5.5 μm.

Figure 5.8b depicts the quantum efficiency of the pπn structure. The temperatures were taken at 77K, 130K and 190K under bias of 0V. The largest value is measured at 77K and 3.0μm is 0.6%. The absorption edge is around 6.5 μm.

Figure 5.8c depicts the quantum efficiency of the pπBn structure. The temperatures were taken at 77K, 130K and 190K under bias of 0V. The highest is measured at 130K and 3.25μm is 23%. The absorption edge is around 6.5 μm.

5.3.3.3. Specific Detectivity

The specific detectivity (D*) results were obtained using equation E3.6. The software creates one graph per each change of temperature. After gathering the information of multiple graphs, the OriginLab software allows to merge the graphs. The graphs obtained for responsivity are depicted in Figure 5.9.

Figure 5.9a depicts the specific detectivity of the nip structure. The temperatures were taken at 77K, 130K and 190K under bias of 0V. The largest value measured at 77K and 4μm is $2x10^9$cmHz$^{1/2}$/W; and the lowest value measured at 190K and 4μm is $2x10^8$cmHz$^{1/2}$/W. The absorption edge is around 5.5 μm and the difference is one order of magnitude.

Figure 5.9b depicts the specific detectivity of the pπn structure. The temperatures were taken at 77K, 130K and 190K under bias of 0V. The largest value measured at 77K and 4μm is $1x10^8$cmHz$^{1/2}$/W; and the lowest value measured at 190K and 4μm is $5x10^6$cmHz$^{1/2}$/W. The absorption edge is around 6.5 μm and the difference is around one and a half order of magnitude.

Figure 5.9c depicts the specific detectivity of the pπBn structure. The temperatures were taken at 77K, 130K and 190K under bias of 0V. The largest value measured at 77K and 4μm is $1x10^{11}$cmHz$^{1/2}$/W; and the lowest value measured at 190K and 4μm is $2x10^9$cmHz$^{1/2}$/W. The absorption edge is around 6.5 μm and the difference is around two orders of magnitude.
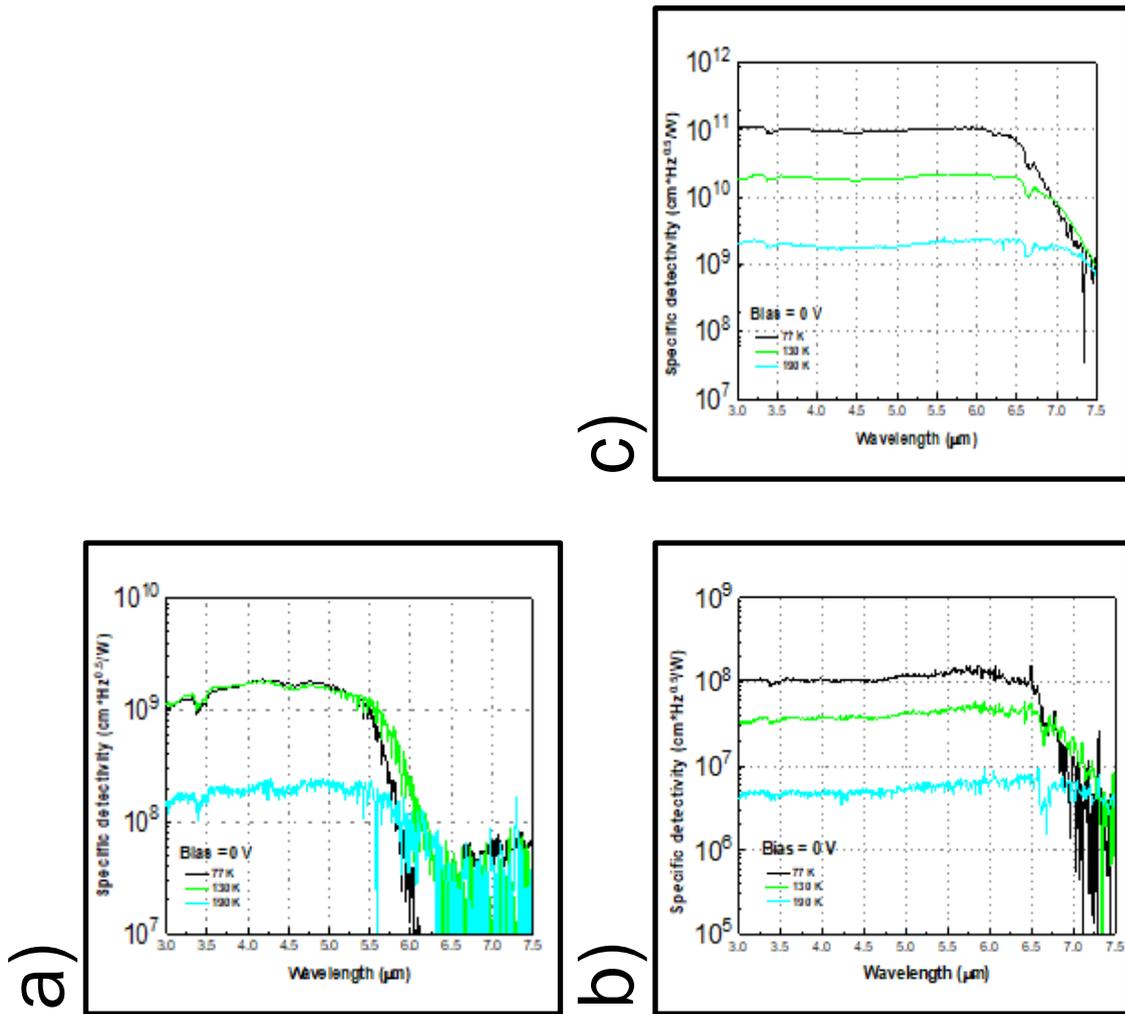
Figure 5.9: Specific Detectivity for a) nip, b) pπn and c) pπBn structures

5.4. Discussion

This chapter compares the performance of three T2SL structures grown on GaAs substrates, which were nip, pπn and pπBn. Overall, it can be concluded that the pπBn was the best architecture due to the wide bandgap unipolar barrier, as it demonstrates the best results in all parameters.

The x-ray diffraction of the pπn and pπBn have similar architectures due to the p-doped absorber and therefore depicts similar shape peaks, which is considerably smaller than the nip. The three structures have achieved similar dislocation density as it depicts fourth order well-define peaks and minor threading dislocation due to direct growth over GaAs substrate.

The atomic force microscope depicts good crystal qualities. All the structures were grown directly on GaAs substrate, which demonstrate very smooth surface with clear atomic terraces. for GaAs substrate. The RMS for nip is 0.5nm (1%), for pπn is 0.9nm (1.8%) and for pπBn is 1.32nm (2.6%).

The dark current behaviour under bias depicts that the pπBn structure has the smallest dark current overall. For the pπn and nip spread is around 1 order between 77K and 190K, while the pπBn spread is around 4 orders of magnitude between 77K and 300K. The wide spread of pπBn can be attributed to poor-quality passivation.

The optical characterisation measured the absorption edge of pπn and pπBn to be 6.5μm and for nip it was 5.5μm. The quantum efficiency for pπBn is 23% while for pπn is 0.6%. The responsivity at 77K depicts the same value for nip and pπBn at their highest value. The specific detectivity at 77K depicts the highest value for pπBn while the pπn is around 3 orders of magnitude smaller.

These results demonstrate that the pπBn has best architecture due to the wide bandgap unipolar barrier. Therefore, future research should compare architectures with more complexity grown directly on Si substrate.

Chapter 6: Conclusion & Future Work

6.1. Conclusion

The aim of this project was to compare the performance between the InAs/GaSb T2SL architectures grown on Si substrate and on GaAs substrate, while finding the best T2SL structure and optimising its architecture in order to develop an IR detector capable of being monolithically integrated.

In order to achieve this, the project was divided in two experiments. The first experiment achieved the first direct growth of an InAs/GaSb T2SL photodiode on Si substrate by molecular beam epitaxy. The second experiment achieved direct growth of an InAs/GaSb T2SL photodiode on GaAs substrate with multiple structures (pπn, nip and pπBn) by molecular beam epitxy.

The ***first experiment*** compared the performance between structures grown on GaAs and Si substrate. The results are depicted in Table 6.1.

The *material characterisation results* are:
   a) X-ray diffraction (XRD) of both architectures has achieved similar dislocation density at zero peak, where the Si is 10% bigger than the GaAs due to the contribution of the GaSb buffer to the zero peak.
   b) Photoluminescence (PL) of the Si peaks are around 40% weaker than the intensity of the GaAs, where their peak wavelength shifted 1% to the left with respect to the GaAs peak.
   c) Atomic force microscope (AFM) of the Si RMS (root mean square) is 24% bigger than the GaAs. The GaAs architecture exhibits good crystal qualities while the Si architecture exhibits atomic clusters.

The *electrical characterisation results* are:
   a) Bias dependent dark current (J_{dark}) of the GaAs is 6% smaller than the Si.
   b) Temperature dependent dark current (J_{dark}) of the Si is 40% smaller than the GaAs.

The *optical characterisation results* are:

    a) Responsivity (R) for the Si is 80% smaller than that of the GaAs;

    b) Quantum efficiency (QE) for the Si is 23% lower than the GaAs; and

    c) Specific detectivity (D*) for the Si is 25% lower than the GaAs.

Table 6.1: First experiment results (GaAs and Si substrate)

Characterisation Results		Parameter	GaAs	Si
Material	XRD	FWHM [arcs]	300.2	331.9
	PL	@ 10K [µau]	70.33	44.38
		Absorption edge [µm]	5.43	5.38
	AFM	RMS @ 5x5µm^2 [nm]	0.5	12
Electrical	J_{dark} vs V	@ 300K & -1V [A/cm^2]	1.8×10^1	1×10^2
	J_{dark} vs $1/T$	above 130K [meV]	53.1	28.1
		below 130k [meV]	absence of G-R mechanisms	
Optical		Absorption edge [µm]	~5.5	~5.5
	R	@ 130K/ -1V/ 4.25µm [A/W]	0.98	0.2
	QE	@ 77K/ -1V/ 4.25µm	33.46%	25%
	D*	@ 130K/ -1V/ 4µm [cmHz^{½}/W]	1×10^9	1×10^8

Overall, it can be concluded that the performance of the Si architecture is consistent with the performance of the GaAs architecture. The construction of the Si substrate is of good quality, good performance and good migration of the structure grown on GaAs substrate.

This **second experiment** compared the performance of three different T2SL structures (nip, pπn and pπBn) grown on GaAs substrates. The results are depicted in Table 6.2.

The *material characterisation results* are:

    a) XRD of the three structures have achieved similar dislocation density at zero peak as well as depicting 4th order well-defined peaks and minor dislocation due to the direct growth over GaAs substrate. The pπn and pπBn structure have similar architectures and shape peaks due to the π-absorber, which is considerably smaller than the nip.

    b) AFM of all the structures depict good crystal qualities demonstrating very smooth surfaces with clear atomic terraces.

The *electrical characterisation results*:

a) Bias dependent dark current of the pπBn structure is around 4 orders of magnitude smaller than the pπn structure. The spread between 77K and 190K for pπBn structure is around 2 orders of magnitude, which can be attributed to poor-quality passivation.

b) Temperature dependent dark current of the pπBn structures is 67% smaller than the nip structure. The dark current values for the pπn and the pπBn are closer to the value of the energy bandgap (~184meV) demonstrating contribution mainly by diffusion.

The *optical characterisation results* are:

a) R for nip and pπBn structures depicts similar values at 77K.

b) QE for pπBn structure is 97% larger than the pπn structure.

c) D* for pπn structure is around 3 orders of magnitude smaller than the pπBn structure.

Table 6.2: Second experiment results (nip, pπn and pπBn structures)

Characterisation Results		Parameter	nip	pπn	pπBn
Optical	*XRD*	FWHM [arcs]	300.2	235	223
	AFM	RMS @ 5x5 µm^2 [nm]	0.5	0.9	1.32
Electrical	*J_{dark} vs V*	@ 77K & -0.6V [A/cm^2]	1.8×10^0	6×10^1	5×10^{-3}
	J_{dark} vs 1/T	above 130K [meV]	53.1	126.8	159.9
Optical		Absorption edge [µm]	~5.5	~6.5	~6.5
	R	@ 77K/ 0V/ [A/W]	0. 55 @ 4.25µm	0.6 @ 6µm	0.6 @ 6µm
	QE	@ 77K/ -1V	17.5% @ 4.25µm	0.6% @ 6µm	23% @ 6µm
	D*	@ 77K/ 0V/ 4.0 µm [cmHz$^{1/2}$/W]	2×10^9	1×10^8	1×10^{11}

Overall, it can be concluded that the pπBn structure has the best overall results due to the wide bandgap unipolar barrier, as it has the highest specific detectivity and quantum efficiency, and the lowest bias temperature dependent dark current.

6.2. Future Work

This project research was focused on comparing the performance of new InAs/GaSb T2SL architectures directly grown on Si and GaAs substrates. In order to achieve these results, the research focused on two experiments:

a) the comparison between the same T2SL photodiode grown on GaAs substrate and on Si substrate; and

b) the comparison between different T2SL photodiode grown on GaAs substrate.

Therefore, the future work should focus on two aspects:

a) in optimisation of Si growth technique, and

b) in developing new T2SL architectures by using unipolar barrier.

The aim of the optimisation is to increase the density of sensors built within one sample, as this project was focused on single pixel fabrication. The optimisation of the T2SL growth technique requires that the threading dislocation density must be reduced so it is important to further optimise the growth process. This requires direct growth on Si substrate was based on the construction of a superlattice buffer including a two-block breakout distribution and a thin nucleation layer. Therefore, the optimisation needs to be in the buffer because the T2SL structure is the same as the reference sample.

The aim of developing new structures is enhancing the device performance as depicted in this research, the more complex the T2SL structure the better dark current and quantum efficiency obtained. This could be achieved by developing new T2SL structures by using existing unipolar barriers used in bulk materials such as M-structure and N-structures, or by developing a completely new structures with the aim of direct growth on Si substrate. These architectures should focus only on the T2SL structure by standardising the rest of the architecture in order to isolate the performance of the T2SL structure.

Regardless of which approach to take, the overall aim of future work is developing an T2SL IR photodiode directly grown on Si substrate for the purpose of being used as a sensor within an IR camera. The objective is to experiment with different growth

conditions such as temperature, thickness and alloys to create a T2SL with a better overall performance.

Based on this research project, Lancaster University has created their own version of T2SL IR photodetector directly grown on Si substrate by modifying mainly the buffer, as expected. The modification in the buffer included a thicker nucleation layer grown, a thicker buffer but still using the same two-block breakout distribution, and a new dislocation filter all grown at the same higher temperature. The InAs/InAsSb SL nBn structure was grown and the results obtained were a dark current density at 200K and 100mV is 1.4×10^{-2} A/cm^2, quantum efficiency at 200K is 25.6% and maximum specific detectivity of 3.65×10^{10} Jones (cmHz^{½}/W), with cutoff wavelength (absorption edge) of ~5.5µm [30]. Therefore, this publication demonstrates that the contribution of this research towards direct growth on Si substrates can be used with different: alloy combinations, growth conditions and SL structures.

However, this research faced many disruptions due to closure of the MBE laboratory for a year of maintenance, to the closure of the cleanroom for a year of maintenance, and to intermittent closure of the PL laboratory for 18 months. This problem delayed the growth of the samples and thus having a cascaded effect until final fabrication.

The other problem associated with this research was the lack of equipment required to perform all the electrical and optical characterisation, which had to be done by Shanghai Tech University in China. This problem meant that the measurements were done at different stages of the research and therefore the measurements were different limiting the interpretation of the results.

Therefore, the best way to improve the results is to control the measurement by having access to all the equipment required over the entire project.

Bibliography

1. *Yan-Feng Lao, Seyoum Wolde, A. G. Unil Perera, Y. H. Zhang, M. Wang, C. Liu, J. O. Kim, Ted Schuler-Sandy, Zhao-Bing Tian, and S. S. Krishna*; **InAs/GaAs p-type quantum dot infrared photodetector with higher efficiency;** Applied Physics Letters 103, 241115 (2013)

2. *Piotr Martyniuk, Antoni Rogalski*; **Modeling of MWIR CdHgTe complementary barrier HOT detector**; Solid-State Electronics 80, pp 96–104 (2013).

3. *Piotr Martyniuk, Waldemar Gawron, Dawid St ̧epie´n, Djalal Benyahia, Andrzej Kowalewski, Krystian Michalczewski, and Antoni Rogalski;* **Demonstration of Mid-Wave Type-II Superlattice**; IEEE Electron Device Letters, VOL. 37, NO. 1, January 2016.

4. *Igor Vurgaftman, Chadwick L. Canedy, Eric M. Jackson, Jill A. Nolde, Chaffra A. Affouda, Edward H. Aifer, Jerry R. Meyer;* **Analysis and performance of type-II superlattice infrared detectors**; Optical Engineering 50(20), 061007 (June 2011)

5. *A. Rogalski*; **History of infrared detectors**; Opto−Electron. Rev., 6, no. 3, 2012.

6. *Dr David R Selviah, Dr Sally E Day, Dr Huiyun Liu;* **Advanced Photonics Devices (*Lecture*)**; Department of Electronic and Electrical Engineering UCL.

7. *Prof Jasprit Singh*; **Semiconductor Technology: Materials, Physics, Devices, Technology (*Book*)**; www.eecs.umich.edu/~singh

8. *Jenny Nelson;* **The Physics of Solar Cells (*Book*)**; Imperial College Press; 2004.

9. *Prof (Emeritus) Chenming Calvin Hu;* **Modern Semiconductor Devices for Integrated Circuits (Book)**; Pearson; 2009.

10. *T. Tansel, M. Hostut, S. Elagoz, A. Kilic, Y. Ergun, A. Aydinli;* **Electrical performance of InAs/AlSb/GaSb superlattice photodetectors**; Superlattices and Microstructures 91, pp 1-7 (2016).

11. *Elena A. Plis*; **InAs/GaSb Type-II Superlattice Detectors;** Hindawi Publishing Corporation Advances in Electronics Volume 614, Article ID 246769.

12. *S. Abdollahi Pour, E. K. Huang, G. Chen, A. Haddadi, B.-M. Nguyen, and M. Razeghi;* **High operating temperature midwave infrared photodiodes and focal plane arrays based on type-II InAs/GaSb superlattices;** Appl. Phys. Lett. 98, 143501 (2011).

13. *E. Plis, M.N. Kutty, S. Myers, H.S. Kim, N. Gautam, L.R. Dawson, S. Krishna;* **Passivation of LWIR InAs/GaSb strained layer superlattice detectors**; Infrared Physics & Technology 54, pp 252-257 (2011).

14. *Elizabeth H. Steenbergen, Gamini Ariyawansa, Charles J. Reyner, Geoffrey D. Jenkins, Christian P. Morath, Joshua M. Duran, John E. Scheihing, Vincent M. Cowana*; **A recent review of mid-wavelength infrared type-II superlattices carrier localization, device performance, and radiation tolerance;** Quantum Sensing and Nano Electronics and Photonics XIV, Proc. of SPIE Vol. 10111, 1011104 (2017).

15. *Elizabeth H. Steenbergen, Kalyan Nunna, Lu Ouyang, Bruno Ullrich, Diana L. Huffaker, David J. Smith, Yong-Hang Zhang*; **Strain-balanced InAs/InAs1-xSbx type-II superlattices grown by molecular beam epitaxy on GaSb substrates**; Journal of Vacuum Science & Technology B, Nanotechnology and Microelectronics: Materials, Processing, Measurement, and Phenomena 30, 02B107 (2012).

16. *Omer Salihoglu, Abdullah Muti, Kutlu Kutluer, Tunay Tansel, Rasit Turan, Yuksel Ergun, and Atilla Aydinli*; **"N" structure for type-II superlattice photodetectors**; Appl. Phys. Lett. 101, 073505 (2012).

17. *Antoni Rogalski*; **Infrared detectors: an overview**; Infrared Physics & Technology 43, pp 187–210 (2002).

18. *A. Rogalski*; **Infrared Detectors for the Future**; Optical and Acoustical Methods in Science and Technology Vol. 116 (2009).

19. *N. Gautam, H. S. Kim, M. N. Kutty, E. Plis, L. R. Dawson, and S. Krishna;* **Performance improvement of longwave infrared photodetector based on type-II InAs/GaSb superlattices using unipolar current blocking layers;** Appl. Phys. Lett. 96, 231107 (2010).

20. *Antonio Ragalski*, **Infrared Detectors (book),** CRC Press (2011).

21. *A. Rogalski, P. Martyniuk, and M. Kopytko;* **InAs/GaSb Type-II superlattice infrared detectors: future prospect;** Appl. Phys. Rev. 4, 031304 (2017).

22. *Manijeh Razeghi, and Binh-Minh Nguyen;* **Band gap tunability of Type II Antimonide-based superlattices;** Physics Procedia 3 (2010).

23. *P. Martyniuk, M. Kopytko, and A. Rogalski;* **Barrier infrared detectors;** Opto-electronics Review 22 (2014).

24. *Claude Weisbuch, and Borge Vinter;* **Quantum Semiconductor Structures: Fundamentals and Applications (book);** Academic Press (1991).

25. *Greg Parker;* **Introductory Semiconductor Device Physics (book);** IOP Publishing Ltd (2004).

26. *John Orton and Tom Foxon;* **Molecular Beam Epitaxy: a short history (book);** Oxford University Press (2015).

27. *Thomas Ihn;* **Semiconductor Nanostructures: Quantum states and electronic transport (book);** Oxford University Press (2009).

28. *Ugur Serincan, Bulent Arikan, Onur Senel;* **Direct growth of type II InAs/GaSb superlattice MWIR photodetector on GaAs substrate;** Superlattice and Microstructures 16, pp 15-21 (2018).

29. *Donghai Wu, Arash Dehzangi, and Manijeh Razeghi;* **Demonstration of mid-wavelength infrared nBn photodetectors based on type-II InAs/InAs1-xSbx superlattice grown by metal-organic chemical vapor deposition;** Appl. Phys. Letter 115, 061102 (2019).

30. *Evangelia Delli, Veronica Letka, Peter D Hodgson, Eva Repiso, Jonathan P. Hayton, Adam P Craig, Qi Lu, Richard Beanland, Anthony Krier, Andrew R J Marshall, and Peter J Carrington;* **Mid-infrared InAs/InAsSb superlattice nBn photodetector monolithically integrated onto Silicon;** ACS Photonics 6, 538-544 (2019).

31. *L. Solymar, D. Walsh,* **Lectures on the Electrical Properties of Materials (book),** Oxford Science Publication (1990).

32. *Ali T Hajiah,* **Materials catalogue, EPI Materials Ltd., Lancaster Way, Ely, Cambridge-shire, CB6 3NW UK.**

33. *E. Scott Barr;* **The Infrared Pioneers I**; Infrared Physics Vol. 1 (1961).

34. *E. Scott Barr;* **The Infrared Pioneers II;** Infrared Physics Vol. 2 (1962).

35. *E. Scott Barr;* **The Infrared Pioneers III;** Infrared Physics Vol. 3 (1963).

36. *A. Rogalski and J. Piotrowski;* **Intrinsic Infrared Detectors;** Prog Quant Electr vol. 12 (1998).

37. *Paul R. Norton;* **Infrared detectors in the next millennium;** Proc. SPIE 3698, Infrared Technology and Applications XXV (1999).

38. *M.B. Reine, A.K. Sood and T.J. Tredwell;* **Semiconductors and Semimetals (book);** Academic Press, Chapter 6 (1981).

39. *S.C. Choo;* **Carrier Generation-Recombination in the space-charge region of an asymmetrical pn junction;** Solid-State Electronic, Pergamon Press vol. 11 (1968).

40. *Paul Harrison;* **Quantum Wells, Wires and Dots (book);** John Wiley & Sons Ltd (2009).

41. *A. Rogalski, P. Martyniuk, M. Kopytko;* **Type-II superlattice photodetectors versus CdHgTe photodiode;** Progress in Quantum Electronics (2019).

42. *D. Selviah, H. Liu;* **Advance Photonic Devices;** UCL EEE Lecture (2018).

43. *Claudia González Burguete, Daqian Guo, Pamela Jurczak, Fan Cui, Mingchu Tang, Wei Chen, Zhuo Deng, Yaojiang Chen, Marina Gutiérrez, Baile Chen, Huiyun Liu, Jiang Wu;* **Direct growth of InAs/GaSb type II superlattice photodiodes on silicon substrates**; IET Optoelectronics, vol. 12, no. 1, pp. 2-4, February 2018.

44. *Zhuo Deng, Daqian Guo, Claudia González Burguete, Zongheng Xie, Jian Huang, Huiyun Liu, Jiang Wu, Baile Chen;* **Demonstration of Si based InAs/GaSb type-II**

superlattice pin photodetector; Infrared Physics and Technology, vol. 101, pp. 133-137, September 2019.

45. *Zhuo Deng, Daqian Guo, Jian Huang, Huiyun Liu, Jiang Wu, Baile Chen;* **Mid-wave infrared InAs/GaSb type II superlattice photodetector with nBp design grown GaAs substrate;** IEEE Journal of Quantum Electronics, vol. 55, August 2019.

46. *B-M. Nguyen, M. Razeghi*; **Type-II "M" Structure Photodiodes: An Alternative Material Design for Mid-Wave to Long Wavelength Infrared Regimes**; Quantum Sensing and Nanophotonic Devices IV, edited by Manijeh Razeghi, Gail J. Brown, Proc. of SPIE Vol. 6479, 64790S (2007).

47. *David Z. Ting, Alexander Soibel, Sam A. Keo, Sir B. Rafol, Jason M. Mumolo, John K. Liu, Cory J. Hill, Arezou Khoshakhlagh, Linda Höglund, Edward M. Luong, Sarath D. Gunapala*; **Development of quantum well, quantum dot, and type II superlattice infrared photodetectors;** Journal of Applied Remote Sensing 084998-1 Vol. 8 (2014).

48. *Ralf Widenhorn, Morley M. Blouke, Alexander Weber, Armin Rest, and Erik Bodegom;* **Temperature dependence of dark current in a CCD;** SPIE Vol 4669 (2002).

49. ISO 20473:2007.

50. *F. Pelayo García de Arquer, Ardalan Armin, Paul Meredith, and Edward H. Sargent;* **Solution-processed semiconductors for next-generation photodetectors;** Nature Reviews (Materials) Vol 2, article number 16100 (2017).

51. *Adeela Rehman, Soo-Jin Park;* **State of the art two-dimensional materials-based photodetectors: Prospects, challenges and future outlook;** Journal of Industrial and Engineering Chemistry 89, pp 28-46 (2020).

52. *Wei Yang, Jiaxin Chen, Yong Zhang, Yujia Zhang, Jr-Hau He, and Xiaosheng Fang;* **Silicon-compatible Photodetectors: Trends to Monolithically Integrate Photosensors with Chip Technology;** Advanced Functional Materials 29, 1808182 (2019).

53. *Maurizio Caslino, Giuseppe Coppola, Mario Iodice, Ivo Rendina, and Luigi Sirleto;* **Near-Infrared Sub-bandgap all-silicon photodetectors: state of the art and perspectives;** Sensor vol. 10, pp 10571-10600 (2010).

54. *Chao Liu, Yanbo Li, Yiping Zeng;* **Progress in Antimonide based III-V compound semiconductors and devices;** Engineering vol 2, pp 617-624 (2010).

55. *Y.H. Kim, Y.K. Noh, M.D. Kim, J.E. Oh, and K.S. Chung;* **Transmission electron microscopy study of the initial growth stage of GaSb grown on Si (001) substrate by molecular beam epitaxy method;** Thin Solid Films vol 518, pp 2280-2284 (2010).

56. *Jiang Wu, Qi Jiang, Siming Chen, Mingchu Tang, Yuriy I. Mazur, Yurii Maidaniuk, Mourad Benamara, Mykhaylo P. Semtsiv, W. Ted Masselink, Kimberly A. Sablon, Gregory J. Salamo, and Huiyun Liu;* **Monolithically Integrated InAs/GaAs Quantum Dot mid-infrared Photodetectors on Silicon substrates;** ACS Photonics vol 3, pp 749-753 (2016).

57. *Svenja Mauthe, Yannick Baumgartner, Marilyne Sousa, Qian Ding, Marta D. Rossell, Andreas Schenk, Lukas Czornomaz, and Kirsten E. Moselund;* **High-speed III-V nanowires photodetector monolithically integrated on Si;** Nature Communications 11:4565 (2020).

58. *Chandler Downs and Thomas E. Vandervelde;* **Progress in Infrared Photodetectors Since 2000;** Sensors vol 13, pp 5054-5098 (2013).

59. *L.J. Kozlowski;* **HgCdTe focal plane arrays for high performance infrared cameras**; Proc SPIE 3179, Solid State Crystals in Optoelectronics and Semiconductor Technology (13th June 1997).

60. *Jonathan R. Andrews, Sergio R. Restaino, Scott W. Teare, Yagya D. Sharma, Member, Woo-Yong Jang, Thomas E. Vandervelde, Jay S. Brown, Axel Reisinger, Mani Sundaram, Sanjay Krishna, and Luke Lester;* **Comparison of Quantum Dots-in-a-Double-Well and Quantum Dots-in-a-Well Focal Plane Arrays in the Long-Wave Infrared;** IEEE Transactions on Electron Devices vol 58, no 7 (July 2011).

61. *Subhananda Chakrabarti, Sourav Adhikary, Nilanjan Halder, Yigit Aytac, and A. G. U. Perera;* **High-performance, long-wave (~10.2 μm) InGaAs/GaAs quantum dot infrared photodetector with quaternary In0.21Al0.21Ga0.58As capping;** Applied Physics Letters 99, 181102 (2011).

62. *Wei, Yajun, Hood, Andrew, Gin, Aaron, Yazdanpanah, Vahid, Razeghi, Manijeh***; High performance LWIR type II InAs/GaSb superlattice photodetectors and infrared focal plane arrays;** Proc. SPIE 5732, Quantum Sensing and Nanophotonic Devices II (25 March 2005).

63. *Sarath D. Gunapala, Sumith V. Bandara, John K. Liu, E. M. Luong, N. Stetson, Craig A. Shott, J. J. Bock, S. B. Rafol, Jason M. Mumolo, and Mark J. McKelvey;* **Long-Wavelength 256 256 GaAs/AlGaAs Quantum Well Infrared Photodetector (QWIP) Palm-Size Camera;** IEEE Transactions on Electron Devices vol 47, no 2 (February 2000).

64. *Mengxia Liu, F. Pelayo García de Arquer, Yiying Li, Xinzheng Lan, Gi-Hwan Kim, Oleksandr Voznyy, Lethy Krishnan Jagadamma, Abdullah Saud Abbas, Sjoerd Hoogland, Zhenghong Lu, Jin Young Kim, Aram Amassian, and Edward H. Sargent;* **Double-Sided Junctions Enable High-Performance Colloidal-Quantum-Dot Photovoltaics;** Advanced Materials vol 28, pp 4142-4188 (2016).

65. *Akihiro Kojima, Kenjiro Teshima, Yasuo Shirai, and Tsutomu Miyasaka*; **Organometal Halide Perovskites as Visible-Light Sensitizers for Photovoltaic Cells;** American Chemical Society vol 131, pp 6050-6051 (2009).

66. *Lou Zheng, Liang Zhongzhu, and Shen Guozhen;* **Photodetectors based on two dimensional materials;** Journal of Semiconductors vol 37 (2016).

67. *Xiaodong Xu, Nathaniel M. Gabor, Jonathan S. Alden, Arend M. van der Zande, and Paul L. McEuen;* **Photo-Thermoelectric Effect at a Graphene Interface Junction;** Nano Letters vol 10, pp 562-566 (2010).

68. *A. Morita;* **Semiconducting Black Phosphorus;** Applied Physics A vol 39, pp 227-242 (1986).

69. *Yejing Dai, Xingfu Wang, Wenbo Peng, Cheng Xu, Changsheng Wu, Kai Dong, Ruiyuan Liu, and Zhong Lin Wang;* **Self-Powered Si/CdS Flexible Photodetector with Broadband Response from 325 to 1550 nm Based on Pyro-phototronic Effect: An Approach for Photosensing below Bandgap Energy;** Advanced Materials vol 30 (2018).

70. *Michael B. Johnston;* **Fast silicon photodiodes;** Nature Photonics vol 11 (2017).

71. *Dung-Sheng Tsai, Chin-An Lin, Wei-Cheng Lien, Hung-Chih Chang, Yuh-Lin Wang, and Jr-Hau He;* **Ultra-High-Responsivity Broadband Detection of Si Metal-Semiconductor-Metal Schottky Photodetectors Improved by ZnO Nanorod Arrays;** ACS Nano vol 5, no 10, pp 7748-7753 (2011).

72. *Chao Xie, Chun-Ki Liu, Hok-Leung Loi, and Feng Yan;* **Perovskite-Based Phototransistors and Hybrid Photodetectors;** Advanced Functional Materials vol 30 (2020).

73. *J Podlecki, L Gouskov, F Pascal, F Pascal-Delannoy and A Giani;* **Photodetection at 3.65µm in the atmospheric window using InAs$_{0.91}$Sb$_{0.09}$/GaAS heteroepitaxy;** Semiconductor Science and Technology vol 11 (1996).

74. *Yating Wan, Zeyu Zhang, Ruilin Chao, Justin Norman, Daehwan Jung, Chen Shang, Qiang Li, MJ Kennedy, Di Liang, Chong Zhang, Jin-Wei Shi, Arthur C. Gossard, Kei May Lau, and John E. Bowers;* **Monolithically integrated InAs/InGaAs quantum dot photodetectors on silicon substrate;** Optics Express vol 25, no 22 (30th October 2017).

Glossary

Abbreviation	Term	Description
d	absorber thickness	
α	Absorption coefficient	
Adatom	Adsorbed atom	An atom that lies on a crystal surface, like graphene.
a-Si	amorphous Silicon	is the non-crystalline form of silicon used for solar cells and thin-film transistors in LCD displays. It is deposited in thin films onto a variety of flexible substrates. These generally feature low efficiency and are environmentally friendly as they do not use toxic heavy metals.
AR	Anti-reflection coating	Is a type of optical coating applied to the surface of lenses and other optical elements to reduce reflection by improving efficiency since less light is lost. Antireflective coatings are often used in microelectronic photolithography to help reduce image distortions associated with reflection off the surface of the substrate. These are applied either before or after the photoresist.
AFM	Atomic force microscope	This is a very high-resolution type of scanning probe microscopy with demonstrated resolution on the order of fractions of a nanometre, more than 1000 times better than the optical diffraction limit.
	Auger coefficient	This is the ratio of the number of auger electrons to the number of ejected x-ray photons. Auger effect is a two-electron process in which an electron makes a discrete transition from a less bound shell to the vacant, but more tightly bound, electron shell. The energy gained in this process is transferred, via the electrostatic interaction, to another bound electron which the escapes from the atom.
BLIP	background limited performance conditions	
BTBT	band-to-band tunneling	
Δf	bandwidth	
V	Bias (voltage)	Biasing in electronics means establishing predetermined voltages or current at various points of an electronic circuit for the purpose of establishing proper operating condition in electronic components. Many electronic devices such as transistors and vacuum tubes, whose function is processing time-varying (AC) signals also require a steady (DC) current or voltage to operate correctly.
BIB	blocked impurity band	
	Blueshift	This is any decrease in wavelength, with a corresponding increase in frequency of an electromagnetic wave. In visible light, this shifts the colour from the red end of the spectrum to the blue end.
k	Boltzmann's constant	
CdHgTe	Cadmium Mercury Tellurium	Band gap 0 - 1.5 eV; Known as "MerCad". Extensive use in sensitive cooled infrared imaging sensors, infrared astronomy, and infrared detectors. Alloy of mercury telluride (a semimetal, zero band gap) and CdTe. High electron mobility. The only common material capable of operating in both 3–5 µm and 12–15 µm atmospheric windows. Can be grown on CdZnTe.

Abbreviation	Term	Description
CdZnTe	cadmium zinc tellurium	Band gap 1.4 eV; upper 2.2eV; direct; efficient solid-state x-ray and gamma ray detector, can operate at room temperature. High electro-optic coefficient. Used in solar cells, can be used to generate and detect terahertz radiation, can be used as a substrate for epitaxial growth of CdHgTe
τ	Carrier lifetime	
CMT	CdHgTe infrared photodetector	This is the common material in photodetectors.
CBIRD	complementary barrier infrared detector	
Δx	Compositional uniformity	
CB	Conduction band	This is the lowest range of vacant electronic state. This is located above the Fermi level.
XSTM	cross-sectional scanning tunneling microscopy	
λ_c	Cutoff wavelength	
	Dark current	Is the relatively small electric current that flows photosensitive devices such as photomultiplier tube, photodiode or charge-coupled device even when no photos are entering the device. It is also referred as reverse bias leakage current in non-optical devices and is present in all diodes. Dark-current spectroscopy can be used to determine the defect present by monitoring the peaks in the dark current histogram's evolution with temperature.
	Doping	Intentionally introduces impurities into an extremely pure intrinsic semiconductor for the purpose of modulating its electrical properties. The impurities are dependent upon the type of semiconductor and the properties that it needs to have for its intended purpose. Lightly and moderately doped semiconductors are referred to as extrinsic semiconductors. A dope semiconductor acts more like a conductor than a semiconductor is referred to as a degenerate semiconductor.
DWELL	Dot-in-a-well	Quantum well is a potential well with only discrete energy values.
m^*	Effective mass	
η	Efficiency	Useful work per quantity of energy, mechanical advantage over ideal mechanical advantage.
EBIC	electron beam-induced current	This is a semiconductor analysis technique performed in a SEM (scanning electron microscope) or STEM (scanning transmission electron microscope). It is used to identify buried junctions or defect in semiconductors, or to examine minority carrier properties. EBIC is similar to cathode luminescence in that it depends on the creating of electron-hole pairs in the semiconductor sample by microscope's electron beam.
q	Electron charge	
n	Electron concentration	
eV	electrovolt	Unit of energy 160 zeptojoules (10-21 joules, Zj) or 1.6x10-19 Joules (J) energy gained by the movement of a single electron across electrical potential difference of 1 volt.

Abbreviation	Term	Description
EDS	energy dispersive x-ray spectroscopy	This is sometimes called energy dispersive X-ray analysis (EDXA) or energy dispersive X-ray microanalysis (EDXMA) is an analytical technique used for the elemental analysis or chemical characterization of a sample. Its characterization capabilities are due in large part to the fundamental principle that each element has a unique atomic structure allowing a unique set of peaks on its electromagnetic emission spectrum (which is the main principle of spectroscopy).
E_g	energy gap	This is also called bandgap and is an energy range in a solid where no electron states can exist. In graphs of the electronic band structure of solids, the bandgap generally refers to the energy difference (in electron volts) between the top of the valence band and the bottom of the conduction band in insulators and semiconductors. It is the energy required to promote a valence electron bound to an atom to become a conduction electron, which is free to move within the crystal lattice and serve as a charge carrier to conduct electric current.
	Epitaxy growth	Epitaxy refers to the deposition of a crystalline overlayer on a crystalline substrate. The overlayer is called an epitaxial film or epitaxial layer. Epitaxial films may be grown from gaseous or liquid precursors. Because the substrate acts as a seed crystal.
EQE	External quantum efficiency	Is the ratio of number of charge carriers collected by the solar cell to the number of photons of a given energy shining on solar cells from outside (incident photons)
μ or EF	Fermi level	This is the total chemical potential for electrons (or electrochemical potential).
FF	Fill factor	Ratio of the actual maximum obtainable power to the product of the open circuit voltage and short circuit current.
FPA	Focal plane arrays	This is an image sensing device consisting of an array of light-sensing pixels at the focal plane of a lens. FPAs are used most commonly for imaging purpose (taking pictures), but can be used for non-imaging purpose such as spectrometry, LIDAR and wave-front sensing.
FIB	focused ion beam	This is a technique used particularly in the semiconductor industry, materials science and increasingly in the biological field for site-specific analysis, deposition, and ablation of materials. A FIB setup is a scientific instrument that resembles a scanning electron microscope (SEM). FIB setup uses a focused beam of ions instead, this can also be incorporated in a system with both electron and ion beam columns, allowing the same features to be investigated using either of the beams.
FTIR	Fourier transform infrared	This is a technique which is used to obtain an IR spectrum of absorption or emission of a solid, liquid or gas. An FTIR spectrometer simultaneously collects high spectral resolution data per a wide spectral range. This confers a significant advantage over a dispersive spectrometer, which measure intensity over a narrow range of wavelengths at a time.
m	Free electron mass	
FWHM	Full width at half maximum	Extent of a function given by the difference between two extremes.

Abbreviation	Term	Description
GaAs	gallium arsenide	III-V direct bandgap semiconductor with zinc blende crystal structure, for solar cells and optical windows.
GaAsN	gallium arsenide nitride	GaN is a very hard mechanically stable wide bandgap semiconductor material with high heat capacity and thermal conductivity.
GaP	gallium phosphide	Semiconductor with indirect bandgap of 2.26 eV.
GaSe	gallium selenium	Band gap 2.1 eV, gap type indirect; photoconductor use in nonlinear optics.
GR	generation-recombination or tunneling or quantum tunneling	This spelling difference refers to the quantum mechanical phenomenon where a particle tunnels through a barrier that it classically could not surmount. This plays an essential role in several physical
Ge	germanium	It is a lustrous, hard, greyish-white metalloid in the carbon group chemically similar to tin and silicon. Pure germanium is a semiconductor. Ge is the substrate of the wafer for high-efficiency multijunction photovoltaic cells for space applications. GaAs and Ge have very similar lattice constant.
III-V	Group III-V	Boron nitride cubic (BN), Baron Phosphide (BP), Boron Arsenide (BAs); Aluminium nitride (AIN), Aluminium Phosphide (AlAs); Aluminium Antimonide (AlSb), Gallium Nitride (GaN), Gallium Phosphide (GaP); Gallium Arsenide (GaAs), Gallium Antimonide (GaSb); Indium Nitride (InN); Indium Phosphide (InP); Indium Arsenide (InAs), Indium Antimonide (InSb)
	heterojunction	This interface occurs between two layers or regions of dissimilar crystalline semiconductors. These semiconducting materials have unequal band gaps as opposed to a homojunction. It is often advantageous to engineer the electronic energy bands in many solid-state device applications, including semiconductor laser, solar cells and transistors. The combination of multiple heterojunctions together in a device is called a heterostructure, although the two unequal band gaps is somewhat loose, especially on small length scales, where electronic properties depend on spatial properties.
HOT	higher operating temperature	An operating temperature is the temperature at which an electrical or mechanical device operates. The device will operate effectively within a specified temperature range, which varies based on the device function and application context, and ranges from the minimum to maximum or high.
HGTSL	High-growth temperature GaAs space layer	
HXRXD	high-resolution x-ray diffraction	
p	Hole concentration	
InAs	indium arsenide	Semiconductor with melting point of 942°C, use for infrared defector wv = 1-38µm; photovoltaic photodiodes. Quantum dotes can be formed in a monolayer of InAs where the tension in the surface layer leads to the formation of QD.
IR	Infrared	Is an invisible radiation energy, electromagnetic radiation with longer wavelength than those of the visible light extending from 700nm (frequency 430THz) to 1,000,000nm (300GHz).

Abbreviation	Term	Description
IB	Intermediate band	It introduces an intermediate band energy level in between the valance and conduction bands. This allows two photons with energy less than the bandgap to excite an electron from the valence band to conduction band.
IBSCs	Intermediate-band solar cells	Made of III-V QD expected to attain of 63% with proper QD alignments. Intermediate band photovoltaics in solar cell research provides methods for exceeding the Shockley-Queisser limit on the efficiency of a cell.
Å	Lattice constant (Armstrong)	Refers to the physical dimensions of unit cells in a crystal lattice. Lattices in three dimensions generally have three lattice constants, referred as a, b, and c. in special case of cubic crystal structures, all of the constants are equal and we only refer to a.
	Lattice-matched cells	Matching of lattice structures between two different semiconductor material allows a region of band gap change to be formed in a material without introducing a change in crystal structure. This allows construction of advance light-emitting diodes and diodes laser. Gallium arsenide, aluminium gallium arsenide, and aluminium arsenide have almost equal lattice constant.
LCCC	leadless ceramic chip carrier	a chip carrier is one of the several kinds of surfaces mount technology packages for integrated circuits. Connections are made on all four edges of a square package. Compared to the internal cavity for mounting the integrated circuit, the package overall size is large. This instead of leads has rounded pins through the edges of the ceramic.
l	length	
LED	Light emitting diode	Produces light from electricity, makes colour light when electricity is sent through in the expected direction.
LIDAR	Light Imaging, Detection, and Ranging	This is a surveying method that measures distance to a target by illuminating that target with a laser light. Lidar is popular used to make high-resolution maps, with applications in geodesy, geomatics, archaeology. It is also called laser scanning and 3D scanning, with terrestrial, airborne, and mobile applications.
LWIR	long-wave infrared	Region of 8-15μm, frequency 6-37THz, temperature 362-193K. The thermal imaging region, in which sensors can obtain a completely passive image of objects only slightly higher in temperature than room temperature. The human body, based on thermal emissions only and requiring no illumination such as the sun, moon, or infrared illumination. The region is also called thermal infrared.
MEMS	Microelectromechanical systems	
MWIR	mid-wave infrared	Region of 3-8μm, frequency 37-100THz, temperature 966-362K. In guided missile technology 3-5μm portion of this band is the atmospheric window in which the homing heads of passive IR "heat seeking" missiles are designed to work, homing on to the infrared signature of the target aircraft, typically the jet engine exhaust plume. This region is also known as thermal infrared.
MBE	Molecular beam epitaxy	Epitaxy (deposition of a crystalline overlayer on a crystalline substrate). MBE is an epitaxy method for thin-film deposition of single crystals. It is widely used for transistors.

Abbreviation	Term	Description
ML	Monolayer	
	monotonically	This is in a monotonic manner.
	n+ contact layer	
NbN	niobium nitride detector	which offers a relatively high superconducting critical temperature (~10K) and a very fast cooling time (<100psec). NbN devices have demonstrated device detection efficiencies as high as 67% at 1064nm wavelength with count rates in the hundreds of MHz
NEP	noise equivalent power	This is a measure of the sensitivity of a photodetector or detector system. It is defined as the signal power that gives a signal-to-noise ratio of one in a one hertz output bandwidth. An output bandwidth of one hertz is equivalent to half a second of integration time. The units of NEP are watts per square root hertz. The NEP is equal to the noise spectral density.
NETD	noise equivalent temperature differences	This is a measure of the sensitivity of a detector of thermal radiation in the infrared, terahertz or microwave portions of the electromagnetic spectrum. It is the amount of incident signal temperature that would be needed to match the internal noise of the detector such that the signal-to-noise ratio is equal to one. Often the spectrum of the NET is reported as a temperature per root bandwidth. A detector that measures power is often interested in the analogous noise-equivalent power (NEP). If a relation between intensity and temperature is well defined over the pass band, as in the case of a blackbody, then the NET simply scales with the NEP.
	Non-polar	It is a molecule when there is an equal sharing of electrons between the two atoms of a diatomic molecule or because of the symmetrical arrangement of three polar bonds at 16°
D*	normalized Detectivity or specific Detectivity	This is a figure of merit used to characterize performance, equal to the reciprocal of noise-equivalent power (NEP), normalized per square root of the sensor's area and frequency bandwidth (reciprocal of twice the integration time).
	nucleation technique	Nucleation is the first step in the formation of either a new thermodynamic phase or a new structure via self-assembly or self-organization. Nucleation is typically defined to be the process that determines how long an observer has to wait before the new phase or self-organised structure appears.
1D/2D/3D	One, two and three dimensional	
Voc	Open circuit voltage	The difference of electrical potential between two terminals of a device when disconnect from any circuit. There is no external load connected, flows between the terminals.
g	Photoelectrical gain	
PL	Photoluminescence	Light emission from any form of matter after absorption of photons (electromagnetic radiation)
PV	Photovoltaic	Are arrays of cells containing a solar photovoltaic material that converts solar radiation of energy from the sun into direct current electricity.
h	Planck's constant	

Abbreviation	Term	Description
	Polar	It has a net dipole as a result of the opposing charges (having partial positive and partial negative charges) from polar bonds arranged asymmetrically. Polar molecules are generally able to dissolve in water.
PCE	Power conversion efficiency	
pin diode	p-type, intrinsic and n-type semiconductor	These are good for photodetectors and high voltage applications. P-type semiconductors have a larger hole concentration than electron concentration, which refers to the positive charge in the hole. N-type semiconductors have a larger electron concentration than hole concentration, which refers to the negative charge of the electron.
QD	Quantum dot	A very small semiconductor particle, only several nanometres in size, so small that their optical and electronica properties differ from those of larger particles. These will emit light of specific frequencies if electricity or light is applied to them, and these frequencies can be precisely tuned by changing the dot's size, shape and material, giving rise to many applications.
QD BIRD	quantum dot barrier infrared detector	
QDIP	quantum dot infrared photodetector	
QE	Quantum efficiency	This may apply to incident photon to cover electron ration of a photosensitive device or it may refer to the TMR effect of the Magnetic Tunnel Junction. It is measured in electrons per photon or amps per watt. QE is often measured over a range of different wavelengths to characterize a device's efficiency at each photon energy level. QE for photos with energy below band gap is zero; photographic film typical has a QE of much less than 10%.
QW	Quantum well	Is a semiconductor with a small energy gap (bandgap) sandwiched between two thicker layers of semiconductor with a larger energy gap such as GaAs.
QWIP	quantum well IR photodetector	This is an infrared photodetector, which uses electronic intersubband transitions in quantum wells to absorb photons. The basic elements of a QWIP are quantum wells, which are separated by barriers. The quantum wells are designed to have one confined state inside the well and a first excited state, which aligns with the top of the barrier.
QWSC	Quantum well solar cells	Is a potential well that confines particles to two dimensions that are otherwise free to move in three dimensions.
	Quasi-Fermi	This is the displacement from equilibrium is such that the carrier population can no longer be described by a single fermi level. This is when the rate tends to be much slower than the energy relaxation within each band (conduction and valence band) can each have an individual population that is internally in equilibrium, even though the bands are not in equilibrium with respect to exchange of electrons.
v	Radiation frequency	
ROC	Read-out circuits	Improve system performance and reduces the fabrication cost.

Abbreviation	Term	Description
ROIC	Read-out integrated circuits	This is an integrated circuit specifically used for reading detectors of a particular type. They are compatible with different types of detectors such as infrared and ultraviolet. The primary purpose for ROIC is to accumulate the photocurrent from each pixel and then transfer the resultant signal onto output taps for readout.
R_0A	Resistance area product	An equilibrium condition is achieved as it no external voltage has been applied.
	reverse bias	Connecting the *p-type* region to the negative terminal of the battery and the *n-type* region to the positive terminal corresponds to reverse bias. If a diode is reverse-biased, the voltage at the cathode is comparatively higher than at the anode. Therefore, very little current will flow until the diode breaks down. The connections are illustrated in the adjacent diagram.
RT	Room temperature	Refers to the range of temperatures that people tend to prefer for indoor setting this are around 6 to 22 °C (68 to 72 °F) (295 to 298K)
STM	scanning tunneling microscope	This is an instrument for imaging surfaces at the atomic level. This is based on the concept of quantum tunneling, when a conducting tip is brought very near to the surface to be examined, a bias applied between the two can allow electronics to tunnel through the vacuum.
	Schottky barrier	This is a potential energy barrier for electronics formed at a metal-semiconductor junction. This have rectifying characteristics, suitable for use as a diode. One of the primary characteristics of a Schottky barrier is the Schottky barrier height, denoted by φ_B, and the value depends on the combination of metal and semiconductor.
SEMI	shallow etch mesa isolation approach	
RSRH	Shockley-Read-Hall recombination	This is when the electron in transition between bands passes through a new energy state (localized state) created within the band gap by an impurity in the lattice, such energy stated are called deep-level traps.
Jsc	Short circuit current density	Short circuit – a connection between two point of different potential in electric circuit, bypassing the load and establishing path of low resistance through which an excessive current can flow. Current density – the ratio of the electric current flowing at a particular point in a conductor to the cross-sectional of the conductor taken perpendicular to current flow at that point.
SWIR	short wave infrared	Region of 1.4-3µm, frequency 100-214THz, temperature 2,070-966K. Water absorption increases significantly at 1450nm. The 1530 to 1560nm range is the dominant spectral region for long-distance telecommunications.
Si	silicon	Group IV, band gap 1.12 eV, gap type indirect
SiGe	silicon germanium	SiGe is beginning to replace GaAs in wireless communication devices.
SC	Solar cells	An electrical device that converts the energy of light directly into electricity by the photovoltaic effect, which is physical and chemical phenomenon.
SPL	Space layer	Layer in between two substrates inside a solar cell.
SLS	Strained Layer Superlattice detectors	Also called Type II superlattice detectors.

Abbreviation	Term	Description
SK growth	Stranski-Krastanow growth mode	This is one of the three primary modes by which thin films grow epitaxially at a crystal surface or interface. The SK mode follows a two-step process.
SCL	Strong carrier localization	Carrier signal, a waveform suitable for modulation by an information beaming signal.
SML	Submonolayer	Is beneath a layer of material that is one molecule thick.
SL	Superlattice	This is a periodic structure of layers of two (or more) materials; the thickness of one layer is several nanometres. This can also refer to a lower-dimensional structure such as an array of quantum dotes.
T	Temperature	
Ea	Thermal activation energy	The activation energy is the minimum energy required to start a chemical reaction, units of kilojoules per mole (kJ/mol) or kilocalories per mole (kcal/mol).
t	Thickness	
TF	Thin-film solar cell	2nd generation solar cells, made by depositing one or more thin layers of photovoltaic material on a substrate such as glass, plastic or metal. Commonly used with CdTe (cadmium telluride), CIGS (copper indium gallium selenide) and a-Si (amorphous thin-film silicon). This allows the cells to be flexible, lower in weight and has less friction. It is used in building in integrated photovoltaics and as a semi-transparent photovoltaic glazing material that can be laminated onto windows. Commercial application uses rigid thin film solar panels (sandwiched between two panes of glass).
TEM	Transmission electron microscope	A beam of electrons is sent towards the specimen – some electrons are reflected, while some pass through. Those that pass through are detected and used to form an image of the specimen at a magnification of about 500,00- times.
TEM	tunneling electron microscopy	
T2SL	Type II Superlattice detector	This is a system made of a repeating sequence of thin layers of different materials. If the layer thicknesses are small enough in a quantum mechanical sense.
UV	ultraviolet	
VB	Valence band	This is the highest range of electron energies in which electrons are normally present at absolute zero temperatures. This is located below the Fermi level.
VLWIR	very long-wave infrared	Region of 14-1000μm, frequency 0.3-6THz, temperature 193-3K.
λ	wavelength	This is a sinusoidal wave is the spatial period of the wave - the distance over which the wave's shape repeats, and thus the inverse of the spatial frequency.
WL	Wetting layer	This is an initial layer of atoms that is epitaxially grown on a surface upon which self-assembled quantum dots or thin films are created. The atoms composing a wetting layer can be alloys (for thin films). This control the artificial atomic states of the quantum dot for uses in quantum information.
ALSL-B	x barrier	
QDs	Zero-dimensional quantum dot or Self-assembled quantum dots	These have a sharper density of state than higher-dimension structures; as a result, they have superior transport and optical properties.